Parameter Extraction for Photovoltaic Device Performance Characterization

by

Ravi Sharma

B.E., Visveswaraiah Technological University, 2009

A THESIS SUBMITTED IN PARTIAL FULFILLMENT OF

THE REQUIREMENTS FOR THE DEGREE OF

MASTER OF APPLIED SCIENCE

in

The College of Graduate Studies

(Electrical Engineering)

THE UNIVERSITY OF BRITISH COLUMBIA

(Okanagan Campus)

August 2017

The undersigned certify that they have read, and recommend to the College of Graduate Studies for acceptance, a thesis entitled:

Parameter Extraction for Photovoltaic Device Performance Analysis Characterization

submitted by Ravi Sharma in partial fulfillment of the requirements of

the degree of Master of Applied Science.

Dr. Stephen K. O'Leary, School of Engineering

Supervisor, Associate Professor

Dr. Richard Klukas, School of Engineering

Supervisory Committee Member, Associate Professor

Dr. Liwei Wang, School of Engineering

Supervisory Committee Member, Assistant Professor

Dr. Sumi Siddiqua

University Examiner, Professor

August 1, 2017

(Date Submitted to Grad Studies)

Abstract

Photovoltaic systems for solar energy harvesting have seen accelerated growth over the past few decades. Crystalline silicon based photovoltaic systems are one of the most widespread photovoltaic solar cell technologies in use today. Such increased penetration of the photovoltaic systems creates new opportunities but also raises challenges, for photovoltaic manufacturers that are tasked with making their product more reliable and of good quality. As a final step during the fabrication of photovoltaic solar cells or modules, the current-voltage characteristics corresponding to each finished product, are measured under standard testing conditions. Measurement of electrical characteristics of the finished product is important for qualification purposes. For quality assessment purposes, certain metrics associated with the current-voltage characteristics, such as open-circuit voltage, short-circuit current, maximum current, maximum voltage, etc., are used based on a chi-by-the-eye method in adjudicating as to whether a given photovoltaic device is of “good” quality. In doing so, only a few of the salient points in the current voltage characteristic are utilized, while detailed information, inherent in the current-voltage characteristic, is not considered. In this thesis, means whereby empirical models of photovoltaic solar cells or modules may be used to fit the experimentally measured current-voltage characteristics is proposed. Accordingly, model parameters that can be used to characterize photovoltaic solar cells or modules are extracted from their measured current-voltage characteristics. These model parameters include photo-generated current, reverse saturation current, diode ideality factor, series resistance, and shunt resistance. For the realization of this objective, one of the most commonly used models to predict the current-voltage characteristic of

a photovoltaic solar cell or module is adopted. A curve fitting approach is proposed based on a non-linear optimization technique to extract model parameters associated with given current-voltage characteristics. In this thesis, computational solutions are developed for accurately extracting model parameters. The presented research spans from performance modeling, parameter estimation methods, to application of an optimization algorithm. Both experimental and standard data are used to investigate the accuracy of the extracted model parameter results obtained to validate the optimal performance of the proposed technique. The possible applications of this approach are discussed.

Preface

This thesis is an original and unpublished work by the author, Ravi Sharma, under the supervision of Dr. Stephen K. O'Leary.

Table of Contents

List of Tables

List of Figures

List of Symbols

Symbol	Description
c	Speed of light
C	Coulomb
E	“Built-in” electric field
E_C	Conduction band edge
E_F	Fermi level
E_V	Valence band edge
E_g	Energy band gap
E_λ	Energy of a photon
f	Frequency
$f(E)$	Fermi-Dirac distribution function
FF	Fill-factor
$f(\bar{x}_k)$	Objective function at current iterate
$g(E)$	Density of available states
h	Planck’s constant
H_k	Hessian approximation
I	Output current
I_{Rsh}	Leakage current through shunt resistance

I_d	Diode current
I_{d1}	Diode current through diode 1
I_{d2}	Diode current through diode 2
I_{mp}	Maximum power current
I_{meas_i}	Measured output current at i^{th} data point
I_{model_i}	Modeled output current at i^{th} data point
I_{ph}	Photo-generated current
I_{sat}	Diode reverse saturation current
I_{sat1}	Diode 1 reverse saturation current
I_{sat2}	Diode 2 reverse saturation current
I_{sc}	Short-circuit voltage
$J(\bar{x}_k)$	Jacobian of objective function
k_B	Boltzmann's constant
L_h	Hole Diffusion Length
L_e	Electron Diffusion Length
$m(\bar{x}_k)$	Quadratic approximation of objective function
n	Diode ideality factor
n_1	Diode ideality factor of diode 1
n_2	Diode ideality factor of diode 2

N_p	Number of solar strings connected in parallel
N_s	Number of solar cells connected in series
$N(\bar{x}_k)$	Open set in the neighborhood of current iterate
P_{in}	Incident solar irradiance
P_{mp}	Maximum power point
q	Charge of electron
$r_i(x)$	Residual vector
R_s	Series Resistance
R_{s1}	Series Resistance of a solar cell in a module
R_{sh}	Shunt Resistance
R_{sh1}	Shunt Resistance of a solar cell in a module
R_{sho}	Negative reciprocal of slope at open circuit point
R_{so}	Negative reciprocal of slope at short circuit point
s_k	Trail step
T	Device temperature
V	Output voltage
V_{meas_i}	Measured output voltage at i^{th} data point
V_{mp}	Maximum power voltage
V_{oc}	Open-circuit voltage

V_t	Thermal voltage
$\bar{x}^*$	Vector representing optimal solution/minimize
$\bar{x}_k$	Vector representing current iterate
$\bar{x}_{k+1}$	Vector representing next iterate
Δ_{k}	Radius of trust-region
$\nabla^2 f\ (\bar{x})$	Hessian matrix of objective function
$\nabla f\ (\bar{x})$	Gradient of objective function
η	Efficiency
θ	Angle of incidence
λ	Wavelength

List of Acronyms

Abbreviation	Definition
AC	Alternating Current
AM	Air-Mass
BOS	Balance of System
c-Si	Crystalline Silicon
DC	Direct Current
EHP	Electron Hole Pairs
EIA	Energy Information Agency
GHG	Green House Gases
GHI	Global Horizontal Irradiation
IEC	International Electrotechnical Commission
LS	Least-Squares
MPP	Maximum Power Point
PV	Photovoltaic
RMSE	Root Mean Squares Error
STC	Standard Testing Conditions
RTC	Radiotechnique Compelec

Acknowledgements

I wish to sincerely thank my supervisor, Dr. Stephen K. O'Leary, for his constant support and encouragement through my program. His unwavering guidance kept me constantly engaged with my research and helped me push through difficult times. I would also like to thank my committee members, Dr. Richard Klukas and Dr. Liwei Wang. Special thanks goes out to our industrial partner, who has wished to remain anonymous, for providing me with the opportunity for the experimental measurements. I would like to thank my fellow graduate students, especially Charles Rockson and Gyan Kumar Shrestha, for their constructive feedback during my writing process. Last, but certainly not the least, I would like to thank my wife, Upashna Thapaliya, for always being there for me and supporting me with all of my decisions.

Dedication

Dedicated to my parents, Chandra Prakash Sharma and Parbati Sharma.

Chapter 1 Introduction

1.1 Overview

Modern industrial societies require energy in order to function. Energy is needed in order to power our industries, heat and air-condition our homes, and allow for our places of business, leisure, and recreation to function. During the 20th Century, fossil fuels have supplied much of our energy needs. At present, nearly 80% of global electrical energy demand is supplied from fossil fuels, such as oil, natural gas, and coal; 14% of global electrical energy demand is supplied from renewable sources of energy, the remaining 6% being from nuclear sources [1]. With the Earth's population expected to grow to nearly 10 Billion by the middle of 21st Century, the global demand for electrical energy is expected to increase by more than two-fold by that time [2]. In recent years, concerns about global warming and the environmental degradation that accompanies the use of fossil fuels have motivated researchers to consider alternate sources of energy. With society's ever increasing demand for electrical energy, coupled with the current rate of depletion of the world's fossil fuel reserves, renewable sources of energy, in their various forms, are being looked at as being a possible solution to the world's pressing energy supply needs [3, 4].

There are various types of renewable energy. For the purposes of this thesis, the focus is on renewable energy sources that are harnessed from natural processes. The U.S. Energy Information Administration (EIA), an agency within the U.S. Department of Energy, classifies mainstream renewable energy sources into five broad categories [5];

- biomass energy,
- hydropower,
- geothermal,
- wind energy, and
- solar energy.

Figure 1.1 stylistically illustrates the most common sources of renewable energy in use as of today. Many forms of renewable energy are themselves derived, either directly or indirectly, from the Sun. Biomass energy, for example, arises from the consumption of materials arrived at through photosynthesis. Hydro-electric energy, which ultimately stems from the natural cycle of evaporation, precipitation, and hydrological flow, is also being powered by the Sun. Wind energy, which arises from the differential heating of the Earth's surface, is another example of an energy source which is a product of the Sun's influence. Finally, solar (thermal or photovoltaic) energy stems from the Sun, albeit in a much more direct manner. In addition to these forms of solar derived energy, there is geothermal energy, which corresponds to the harvesting of energy from within the Earth itself. Although the classification of geothermal energy as a renewable source of energy is sometimes questioned, the fact that sources of geothermal energy, i.e., heat generated within the Earth, is continuous and unlikely to run out, supports this classification. A distinct advantage of renewable sources of energy is that in addition to being sustainable, such sources offer the advantage of not contributing to the emission of

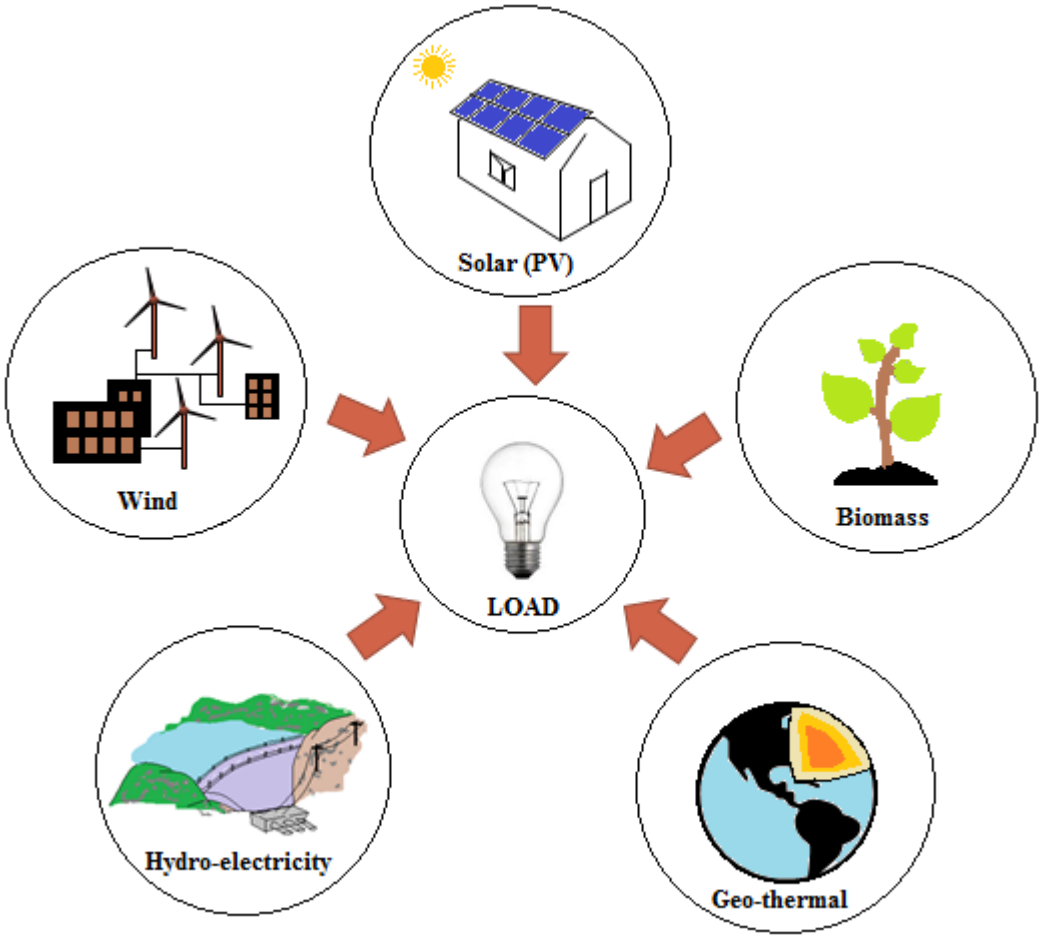

Figure 1.1: The most common forms of renewable energy in use today, drawn in illustrated form. The online version of this figure is in color.

green-house gases (GHG)[1], this being a pressing issue facing the modern world today. Therefore, such sources of energy are often termed as clean forms of energy.

Of the aforementioned sources of renewable energy, solar energy is currently viewed as one of the most promising sources of renewable energy for the generation of electrical energy [6]. Solar energy is converted directly into electrical energy via photovoltaic solar cells that are made up of semiconductor materials. An individual photovoltaic solar cell typically generates a voltage of just under 0.6 V at 25°C and 1000 Watts per meter squared of incident solar radiation [7]. In order to generate higher voltages and current levels, photovoltaic solar cells are connected electrically in series and/or parallel configurations. This ensemble of photovoltaic solar cells is packed together in an environmentally protective laminate, thus forming a photovoltaic solar module. Any number of photovoltaic solar modules connected in series and/or parallel configurations form a complete power generation unit referred to as a photovoltaic system that may be used to produce commercial or utility scale currents and voltages.

The genesis of photovoltaic technology dates back to the 19th Century when Edmond Becquerel, in 1839, observed the photovoltaic effect using platinum electrodes in a conductive solution exposed to light, as noted in [8]. Since then, a great amount of effort had been invested in order to understand the interaction of light and materials (metals and semiconductors) and how such processes can be used for the generation of electrical energy. The commercial age of photovoltaic solar cells, however, began in

[1] The combustion of biofuels releases CO_2 which is more or less equivalent to what would have been released naturally as the organic matter decomposed. Therefore, there is no net increase in global green-house gas accrued as a result of the combustion of biomass [71].

1954, when Chapin, Fuller, and Pearson, of Bell Telephone Laboratories, developed the first crystalline silicon-based photovoltaic solar cell with a conversion efficiency of 6% [9]. A tremendous amount of effort has been devoted ever since towards improving the conversion efficiency of photovoltaic solar cells. Factors, such as the need for the use of photovoltaic solar cells in space applications and the oil embargo of 1973, created a favorable atmosphere for the steady growth of photovoltaic technology, with gradual improvements in conversion efficiency being noted [10, 11]. By the late 1980s, photovoltaic technology was being considered for general urban and suburban applications and mainstream grid connected applications for utility power generation [10]. Well established semiconductor industries during the initial days, and mature processing and manufacturing technologies available for electronic grade silicon favored the growth of the photovoltaic industry with silicon being the preferred semiconductor material of choice for fabrication [12]. To date, commercial mono-crystalline silicon based photovoltaic solar cells, with efficiencies as high as 24.1 %, have been reported [13, 14], while researchers have recently reported tandem concentrator solar cells with efficiencies as high as 42.3 % [15]. Figure 1.2 illustrates the improvements in the efficiency of different technologies of photovoltaic solar cells that have been achieved thus far.

Figure 1.3 shows the growth of photovoltaic installed capacity. Note the annual additions between 2005 and 2015 [16]. This growth has been further complemented by the gradual decline in manufacturing costs of semiconductor materials [17]. Favorable energy policies implemented by

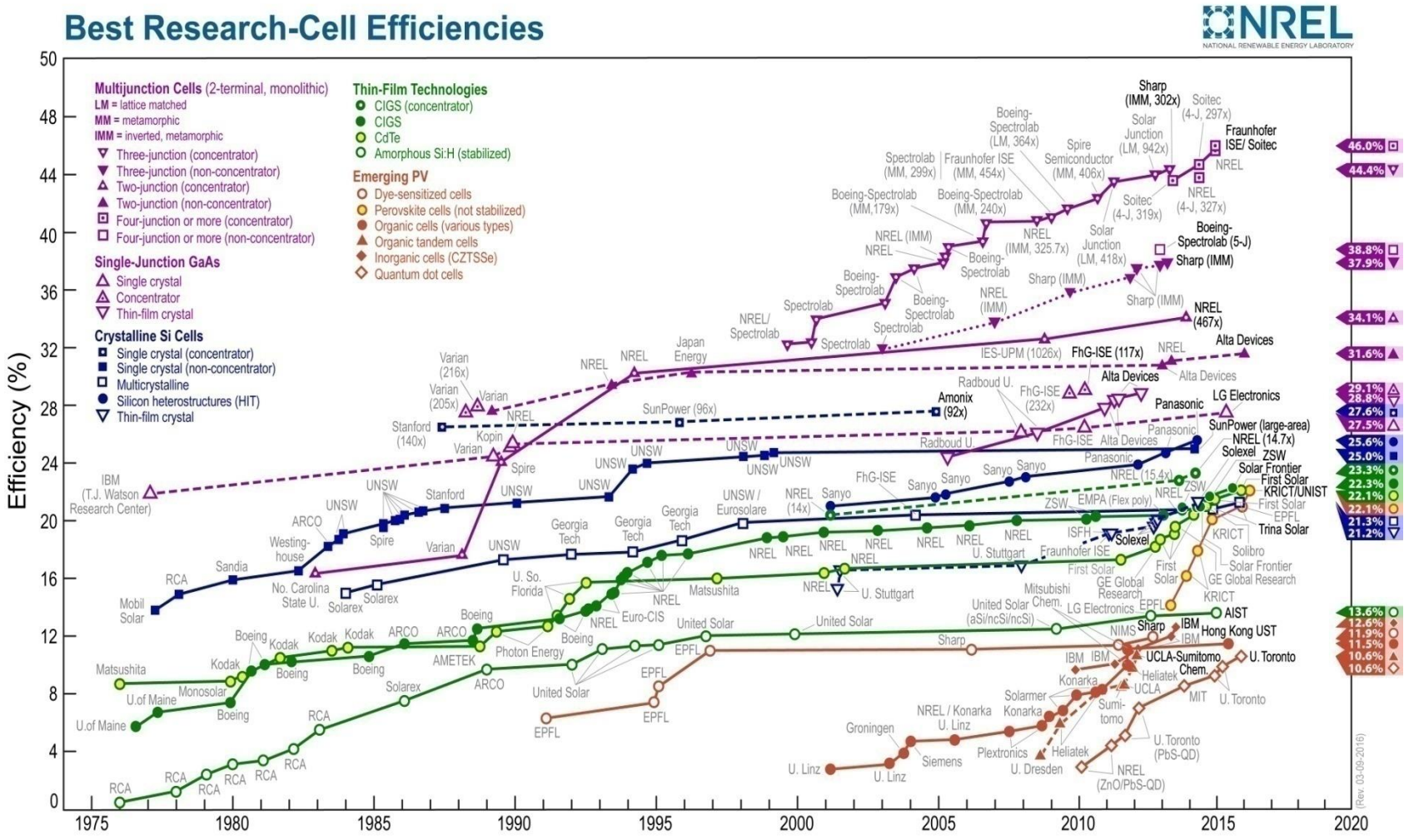

Figure 1.2: Best research solar cell efficiencies recorded between 1975 and 2015. This plot is courtesy of the National Renewable Energy Laboratory, Golden, CO.

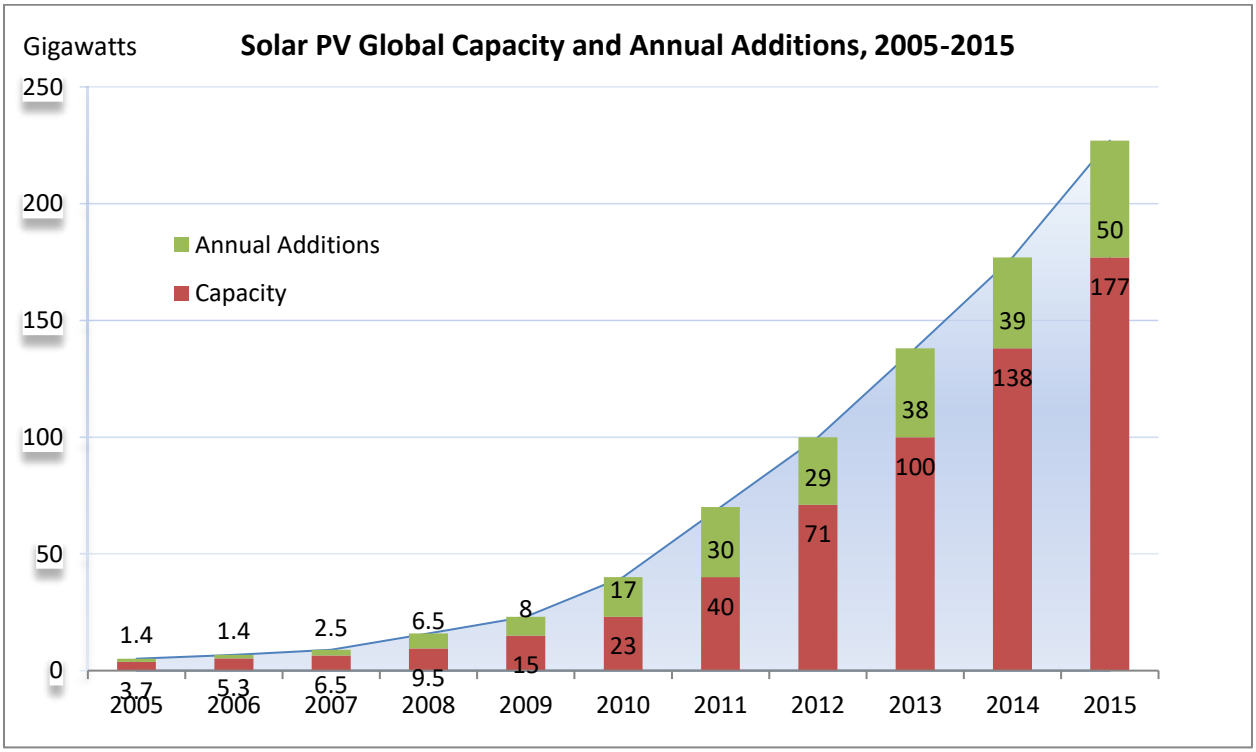

Figure 1.3: Solar PV global capacity and annual additions, 2005-2015. This figure is after Renewable 2016 Global Status Report [16]. The online version of this figure is in color.

different governments around the world in order to encourage investment in renewable energy, has resulted in a significant growth of both small-scale residential and grid connected large-scale photovoltaic power plants [18].

The European Photovoltaic Industry Association has forecast that utilizing the full potential of sunbelt countries translates into a potential for global energy production capacity in the range of 400 GWp by 2030, based on an accelerated growth forecast [19]. Figure 1.4 depicts a map representing annual global horizontal irradiance [20]. The increasing use of photovoltaic systems for electrical generation entails a detailed understanding of such systems and their operation. Figure 1.5 illustrates a typical photovoltaic system with the various components connected related to energy generation and conditioning. A robust understanding of the interaction of photovoltaic solar cells, which form the core of such a system, with the balance-of-system, which includes pieces of equipment, such as the wiring, switches, a mounting system, inverters, a battery bank, battery charger, etc., is essential for the efficient design and operation of complete photovoltaic systems.

The modeling of a complete photovoltaic system assists in the development of efficient converter/controller systems by matching the control and drive requirements of the converter system to the characteristics of the photovoltaic system [21]. These controllers ensure that photovoltaic systems are being operated in an optimal manner so as to produce the maximum possible electrical energy in a rather dynamic condition of operation and are therefore termed as Maximum Power Point Controllers. The amount of energy generated by a photovoltaic system relies heavily on meteorological

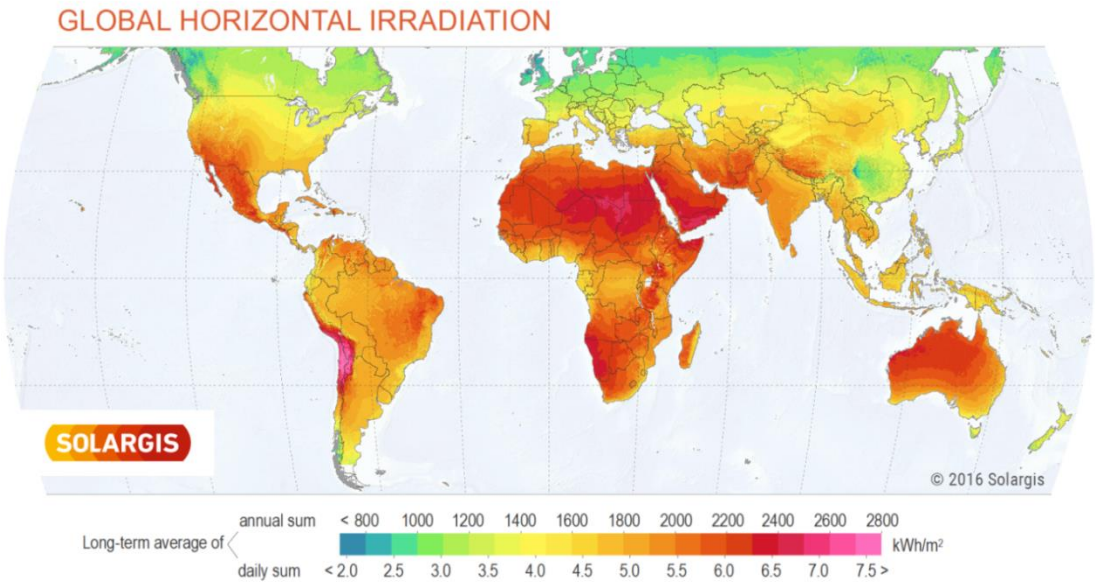

Figure 1.4 : Global horizontal irradiation. GHI Solar Map © 2016 Solargis, used under Creative Commons Attribution-Share Alike 3.0 Unported License. The online version of the figure is in color.

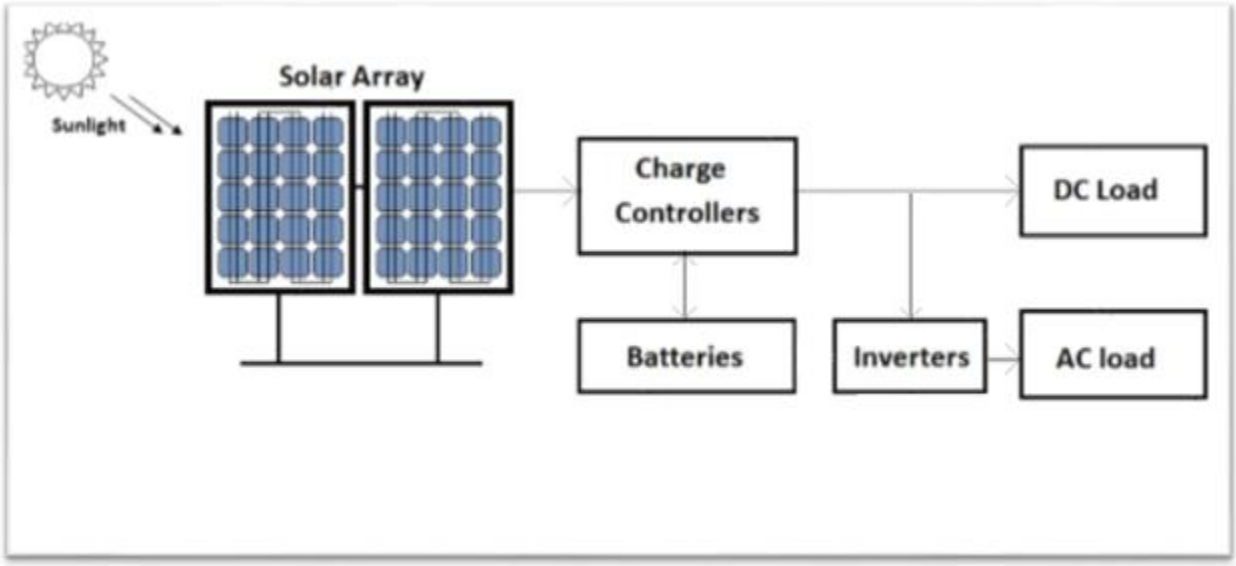

Figure 1.5 : Schematic of a typical photovoltaic system used for the generation of electrical energy. The figure is adapted from Dufo-Lopez *et al.* [22]. The online version of this figure is in color.

factors; therefore, the designer of such systems must be able to predict the system performance subject to a range of environmental conditions. Such studies are not just essential during the initial design phase, but also for the preventive maintenance and troubleshooting of such systems. Accurate models that can simulate and predict the behavior of photovoltaic systems will help with performance optimization.

1.2 Motivation of thesis

At present, photovoltaic systems seem destined to play an important role in supplying our future energy needs. Our understanding of the performance of photovoltaic systems and their interaction with other units will influence the efficient operation of such systems, thereby influencing their power generation capabilities. From a commercial perspective, the electrical (power) performance of photovoltaic devices, i.e., photovoltaic solar cells or modules, are typically characterized through measurement of their current-voltage characteristics under standard testing conditions defined with the air-mass 1.5 (AM1.5) spectrum of incident solar radiation and a device temperature of 25°C. This is done to ensure uniformity in the evaluation and comparison of photovoltaic devices (solar cell or modules) from different manufacturers. The actual operating conditions, however, seldom reflect standard test conditions of a laboratory. Standards, such as IEC 60891, have been established, that define components and processes involved in power measurements, for standardization across the industry. An appliance, called a flash tester, also known as a solar simulator, measures the current-voltage characteristics by exposing a given photovoltaic device to a short and bright flash of artificial light which is as close to the solar spectrum as possible. The qualification of the tested photovoltaic device is based on the measured

power with respect to a calibrated reference cell (or module).

1.3 Thesis objective

A common quality-control step that is performed in photovoltaic device manufacturing is the determination of the current-voltage characteristics corresponding to each photovoltaic device produced; this is achieved using the aforementioned solar simulator. In standard analysis, metrics associated with this measured current-voltage characteristic, such as, the open-circuit voltage, the short-circuit current, the maximum power point, the fill-factor, etc., are used to adjudicate as to whether a given photovoltaic device is adequate or not. In such traditional approach, for the assessment of quality of the solar photovoltaic device, such performance metrics are determined from the measured current-voltage characteristics of the device under test. Certain thresholds defined for these performance metrics, for example, a threshold for peak power generated by the photovoltaic device under test, are then used as a reference to accept or reject the product during such test and further to classify the qualifying products into different product categories.

It is noted that this approach to quality-control uses few selective performance metrics determined from the measured current-voltage characteristics of the device under test and neglects the full-range of data included in the corresponding current-voltage characteristic, i.e., an entire current-voltage characteristic is reduced to a number of salient points. It might be expected that an alternate approach to quality-control, that takes into account the full-range of data in a current-voltage characteristic, would involve the extraction of model parameters corresponding to a given current-voltage

characteristic and the assessment as to whether or not the obtained model parameters fall into the range of values expected for a “good-quality” photovoltaic device.

In this thesis, an empirical model that accurately describe the nonlinear electrical characteristics of the photovoltaic device, often termed as single-diode equivalent circuit model, will be adopted to describe the photovoltaic device performance. This empirical model describes the electrical characteristics of photovoltaic devices based on the fundamental material and device properties such as inherent parasitic resistances, non-linear diode properties etc. which vary according to the model employed to characterize the photovoltaic device. These fundamental parameters collectively define the electrical performance of the photovoltaic device. The aim of this thesis is to extract these fundamental model parameters from the experimentally measured current-voltage characteristics of the photovoltaic device under test and use such model parameters to ascertain the quality of the photovoltaic device. The extracted model parameters may further be utilized to categorize each photovoltaic device into different product categories based in the extracted model parameters. Figure 1.6 depicts this process conceptually. The n-dimensional hyperspace represents the subset of the acceptable values corresponding to each of the “n” model parameters such that devices with model parameters within the subset are deemed acceptable while those with model parameters outside the range of acceptable values are rejected.

The extraction of the fundamental model parameters from current-voltage characteristics constitutes a challenging task, especially due to the non-linear nature of the current-voltage characteristics of such device. In this thesis, this problem is addressed by formulating the model

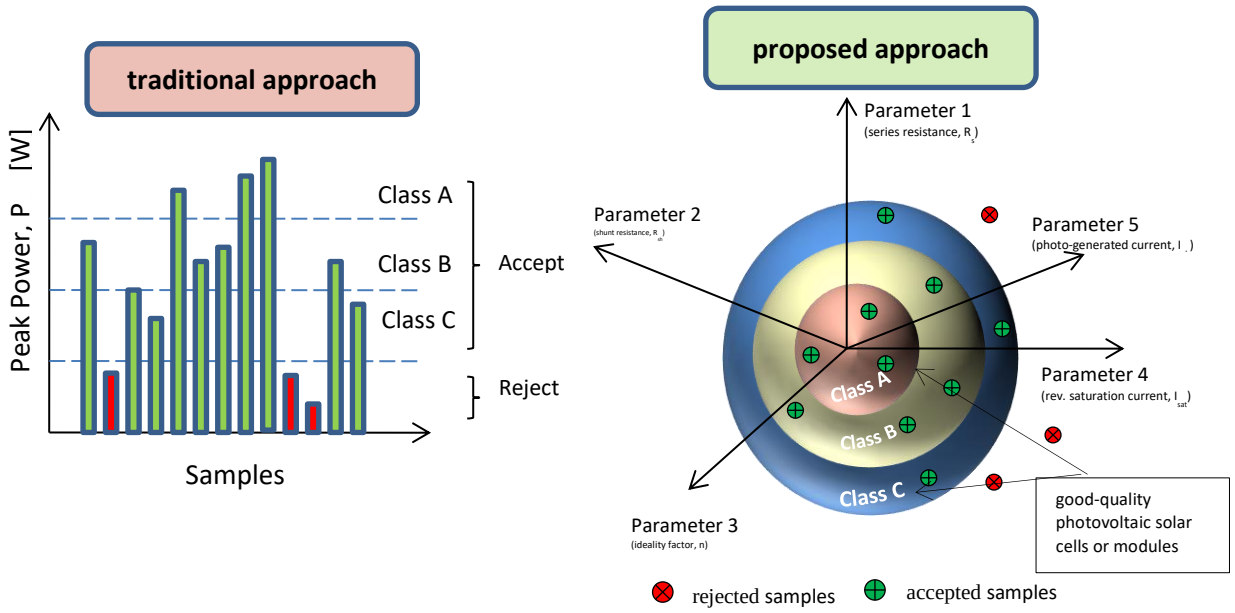

Figure 1.6 : Traditional approach versus an illustration of an n-dimensional hyper-space for the model parameter search. The model parameters selections that fall within the "good-quality" hyper-sphere are deemed to correspond to good-quality photovoltaic solar cells or modules. Those that fall outside are considered poor-quality photovoltaic solar cells or modules. The online version of this figure is in color.

parameter extraction as a multivariate optimization problem and a means whereby such model parameter extraction may be pursed, is developed. In particular, within the framework of a single-diode circuit model, representing the current-voltage characteristic of a photovoltaic device, using a least-squares fitting approach based on a trust region optimization, formal means of model parameter extraction are developed. This approach represents an improvement over the status quo, wherein model parameters are usually determined through a visual process, i.e., the so-called chi-by-the-eye approach. The use of this approach for quality-control applications lies beyond the scope of this particular thesis, in particular, due to the lack of control that was exercised over the composition of the constituent components and processes involved in the fabrication of the samples of the photovoltaic device used in the study for measurement of current-voltage characteristics. The focus of this study is on accurate parameter extraction based on curve-fitting techniques which have been implemented via an optimization algorithm scripted in MATLAB®.

1.4 Thesis outline

The thesis is organized into five individual chapters. Chapter 2 begins with details related to device physics, especially the structure and principle of operation of a photovoltaic solar cell. It then proceeds to present a review of the literature available with regards to model parameter extraction for the modeling of a photovoltaic device. Building upon the contents of Chapter 2, Chapter 3 first presents empirical models of photovoltaic devices. It then discusses the sensitivity of the current-voltage characteristics with respect to the variations in the underlying model parameters. Then, the algorithm, whereby model

parameters may be extracted from a measured current-voltage characteristic, is presented. Chapter 4 provides further details related to the model parameter extraction process for photovoltaic devices, based on measured current-voltage characteristics. In this regard, both experimental data and standard data, available in the literature, are used. Chapter 5 concludes by presenting the main contributions of the thesis. It also discusses possible future work that builds upon these results.

Chapter 2 Background

2.1 Introduction

For the informed modeling of a photovoltaic system, awareness of the underlying physics is crucial. Photovoltaic systems are comprised of an ensemble of photovoltaic solar cells, these being fabricated from semiconductor materials. Certain semiconductor materials possess properties which enable them to convert sunlight into electrical energy. A detailed presentation of the underlying semiconductor material physics is an elaborate exercise, beyond the scope of this particular thesis. Therefore, only a brief introduction to semiconductor materials is presented here together with a discussion on how such materials interact with sunlight. Readers are encouraged to refer to the scientific literature for more detailed studies into this subject matter [23].

In this chapter, I begin by presenting some of the fundamental physics concepts that are needed in order to perform the subsequent research. In particular, the material structure and the basic properties associated with the semiconductors used within photovoltaic solar cells, are discussed, and the interaction of light with photovoltaic solar cells is presented, light-material interactions being at the heart of the performance of a photovoltaic solar cell. The typical structure of a photovoltaic solar cell, its characteristics, and the process of manufacturing such cells, are then presented. The concept of the solar spectrum, and its interaction with a photovoltaic solar cell, is then featured. This is followed by a brief discussion of the various circuit models used to describe the current-voltage characteristics of a photovoltaic solar cell and a review of the literature corresponding to model parameter extraction from such characteristics is featured.

This chapter is organized in the following manner. In Section 2.2, a selection of important semiconductor characteristics is presented. In Sections 2.3 and 2.4, a discussion on the structure and operating principles of photovoltaic solar cells are presented, followed by the study of the solar spectrum in Section 2.5. In Section 2.6, a typical commercial photovoltaic solar cell and its characteristics are presented. The process of commercial fabrication and the testing of photovoltaic solar cells are discussed in Sections 2.7 and 2.8, respectively. Sections 2.9 through 2.11 is where the electrical models of the photovoltaic solar cells is discussed and some of the established approaches used for extracting model parameters corresponding to such cells is looked into.

2. 2 Semiconductors materials

For the fabrication of photovoltaic solar cells, silicon (Si) is the dominant semiconductor material [24]. Besides silicon, compound semiconductors, such as gallium arsenide (GaAs), cadmium telluride (CdTe), copper indium gallium selenide (CIGS), and gallium indium phosphide (GaInP), may also be used for photovoltaic solar cell fabrication. Semiconductors are materials with electrical properties that lie between those associated with insulators and conductors, in the sense that the conduction of charge carriers, through a semiconductor material, can be controlled in some manner. The control of the conductive processes within a semiconductor is usually achieved through the application of a voltage, current, light, or mechanical stress.

For the case of crystalline Si (c-Si), each Si atom bonds with four neighboring Si atoms. The atoms within c-Si are laid out in a periodic and ordered fashion, i.e., there is long-range order. Si is a group IV

element in the periodic table and the electronic configuration of Si is $1s^2 2s^2 2p^6 3s^2 3p^2$; this can alternatively be expressed as $[Ne]3s^2 3p^2$. Each Si atom has four valence electrons in its outermost shell, and shares these electrons with four of its nearest neighboring atoms, thereby forming covalent bonds. This arrangement results in a tetrahedral structure, wherein each covalent bond is directed as far away from the others as possible, i.e., at an angle of approximately 109.5° with respect to each other. The repetition of such a structure in all directions around any given silicon atom allows for the formation of the ideal c-Si lattice. Figure 2.1 shows the unit cell associated with a Si crystal lattice, where the Si atoms are represented by the solid spheres while the covalent bonds, comprised of two valence electrons, are represented with solid lines joining the neighboring Si atoms. This resulting unit cell of a diamond crystal structure possesses a unit cell lattice constant, a, of 5.43 $\AA$.

In two-dimensional form, the arrangement of silicon atoms within c-Si can be pictorially represented, as depicted in Figure 2.2. Here, the two lines between each pair of silicon atoms represent the covalent bonds between two neighboring Si atoms, each line representing a valence electron. Figure 2.2 suggests that the covalent bonds between all silicon atoms are completely satisfied and that there are no free electrons within the crystal. This representation is only valid at absolute zero temperature, with no impurities, any sort of defect, and thermal vibrations being present within the crystal.

An isolated atom will have a discrete spectrum of energy levels associated with it, these energy levels corresponding to the electron energy levels associated with the different quantum states with an atom. As atoms are brought together in order to form a solid, however, the situation changes and the

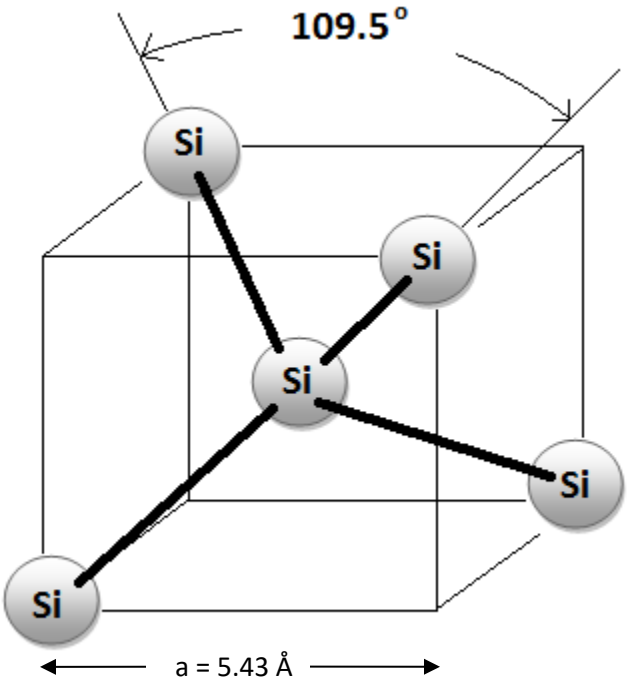

Figure 2.1: The unit-cell associated with c-Si. The silicon atoms are represented with the spheres, while the covalent bonds are depicted with the thick solid lines joining the silicon atoms. The figure is adapted from Hu [25].

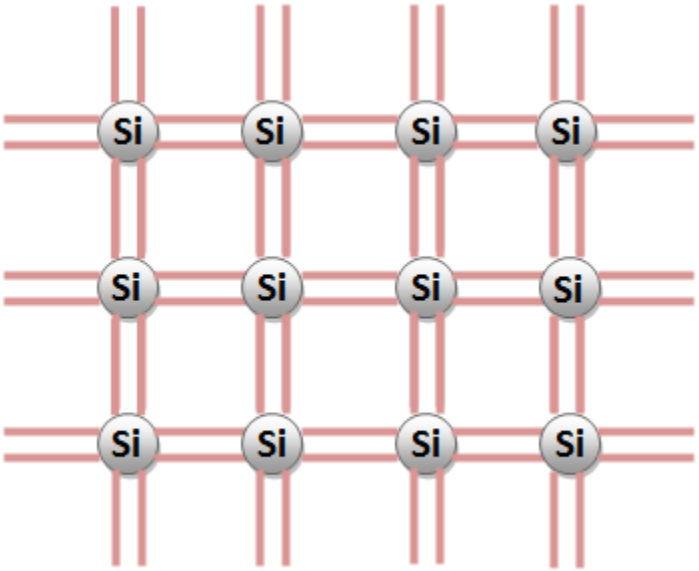

Figure 2.2: A two-dimensional representation of the crystalline silicon (c-Si) crystal structure. This figure is adapted from Kasap [23]. The online version of this figure is in color.

energy levels change owing to the wave functions overlapping between the neighboring atoms. For an isolated Si atom, all such electrons occupy discrete energy levels. When *N* isolated Si atoms are brought together into close proximity, however, these discrete energy levels overlap and are replaced with bands of energy states separated by gaps between the bands. The dependence of the energy level locations on the inter-atomic separation distance, *d*, for the case of crystalline Si, is depicted in Figure 2.3. This broadening of the energy levels into bands occurs because, with the close proximity of any two Si atoms, each discrete energy level splits into two levels. For the case of *N* atoms in close proximity, the discrete energy levels split into *N* energy levels, whereas *N* goes to infinity, the discrete energy levels become a continuum, i.e., a band. This phenomenon is related to the Pauli exclusion principle which does not allow electron energy levels to be the same so that a set of very closely spaced energy levels is formed when a large number of atoms are confined into a small volume. These closely spaced energy levels appear as a band of energy levels, as shown in Figure 2.3. The electron energy levels associated with the core electrons also experience broadening but over smaller inter-atomic distances owing to the limited extent over which their wavefunctions range. Here we are focusing on the two outermost orbitals (3s and 3p) corresponding the highest energy levels. The other energy levels, especially the lower energy levels, are completely filled and do not take part in inter-atomic interactions. Hence, only the 3s and 3p orbital are shown in the Figure 2.3 to demonstrate the splitting of energy levels of each of the N Si atoms brought together into close proximity. The properties of a material vary critically based on how the bands associated with the material are occupied. Bands can be completely or partially filled or unoccupied.

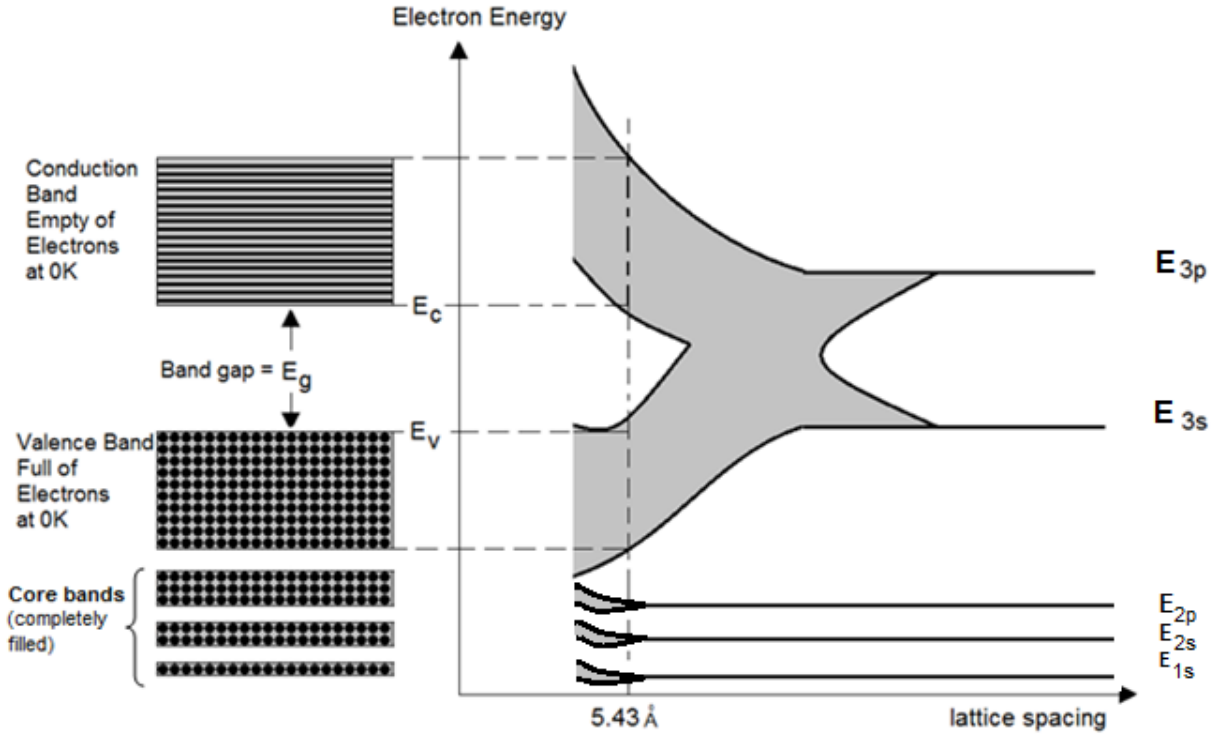

Figure 2.3: The formation of energy bands when N isolated Si atoms are brought together into close proximity at absolute-zero temperature (0K). This figure is after Kasap [23].

Hence, of the different energy bands associated with a semiconductor, we are particularly interested in the two highest energy level bands, i.e., the valence band and the conduction band.

At absolute-zero temperature, all of the lower energy bands are completely filled while the higher energy bands are completely empty, i.e., the valence band is completely full of valence electrons while the conduction band contains empty energy states. The gap between the valence band and the conduction band is referred to as the energy band gap, E_g , and is a material property of the semiconductor in question. With the valence band completely filled with electrons and the conduction band completely devoid of electrons, there is no net velocity of electrons, and hence, no electrical conduction at absolute-zero.

At temperatures above absolute-zero, the atoms within the crystal begin to vibrate due to the absorption of thermal energy. This lattice vibration will result in the stretching of the covalent bonds between the Si atoms. In response to thermally generated vibrations, some of the covalent bonds may become over-stretched, resulting in a rupturing of that covalent bond and the release of a "free" electron into the conduction band. Figure 2.4 illustrates how thermally generated vibrations lead to the generation of electron-hole pairs. The amount of charge carriers generated based on thermal vibrations depends critically on the temperature. The "free" electron or conduction electron, as it is commonly referred to, is free to drift through the crystal lattice. With the absorption of additional thermal energy, the conduction electron is promoted into the conduction band where it can contribute to the electrical conduction under the influence of an applied electric field. The breaking away of the conduction electron results in a void

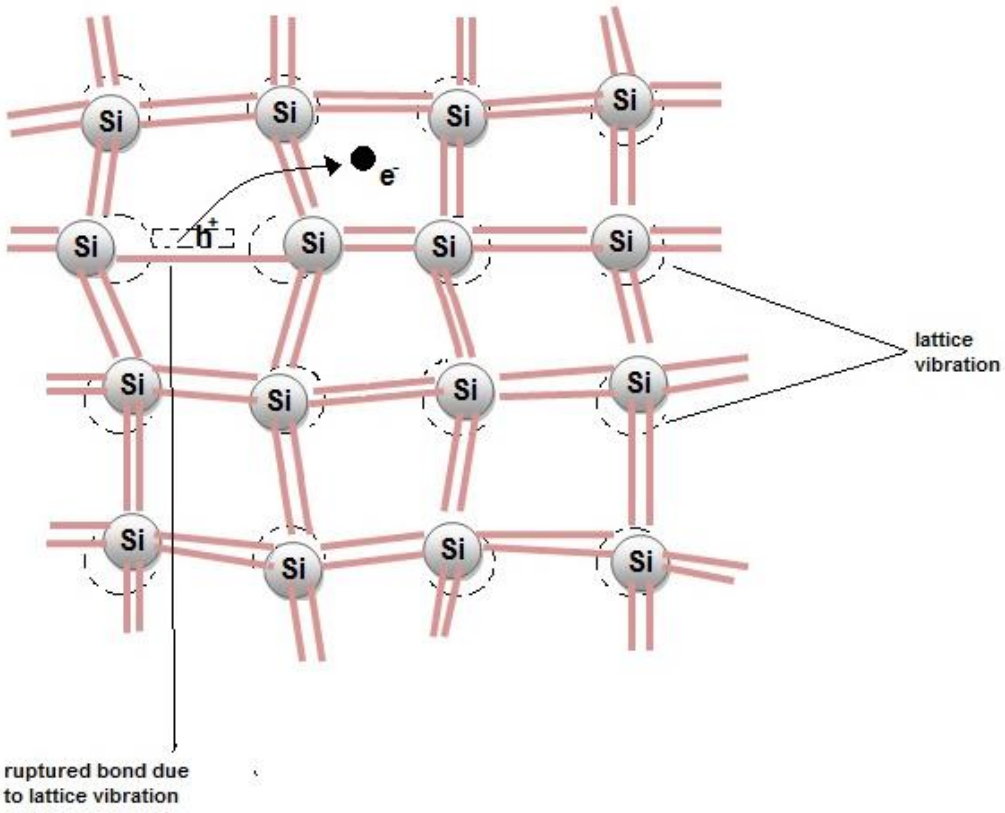

Figure 2.4: Thermal vibrations of Si atoms as a result of the absorption of thermal energy, above absolute zero temperature, rupturing some of the covalent bond due to the overstretching of the bonds. This figure is adapted from Kasap [23]. The online version of this figure is in color.

with a net positive charge in an otherwise neutral region of the crystal. This vacancy, or the absence of the electron, results in an empty electronic state within the valence band and is referred to as a hole, an entity with a net positive charge.

Similar to conduction electrons, holes, with a positive charge, drift under the influence of an applied electric field, and therefore also contribute to the electrical conduction of the crystal. The movement of a hole in a crystal lattice is essentially another electron ”jumping” or tunneling from a neighboring bond to occupy the void left by the conduction electron in the original bond. This is effectively equivalent to the hole moving in the opposite direction within the crystal. This process can repeat itself. As a result, the hole appears to be a positive charge carrier that can drift within the crystal lattice, thereby contributing to the electrical conduction. Therefore, electrons and holes are the two charge carriers within the semiconductor crystal that contribute to the electrical conduction.

The thermal vibration of the Si atoms within the crystal is one of the processes resulting in the generation of charge carriers (electron-hole pair) but it is not the only one. An electron in the valence band can also gain additional energy from an incident photon to become a conduction electron at a higher energy level and therefore contribute to the electrical conduction. In fact, the creation of electron-hole pairs (EHP) in semiconductors due to the absorption of the incident sunlight is the driving principle underlying photovoltaic solar cells. The valence band consists of electrons at an energy level, lower by an amount of at least the energy band gap, E_g, with respect to the higher energy empty electronic states in the conduction band. The excitation of valence electrons into the conduction band where the electron

occupies one of the empty electronic states and becomes a conduction electron requires a minimum amount of energy equivalent to E_g. This is achieved when a photon of energy, $hf > E_g$, is incident on the electron in the valence band, where h is Planck's' constant and f is the frequency of the incident photon. The electron absorbs the incident photon and gains sufficient energy to overcome the energy band gap, E_g, and move into the conduction band, leaving behind a hole in the valence band. This results in the generation of charge carriers or electron-hole pairs that contribute to the electrical conduction. Figure 2.5 illustrates the process of charge carrier generation when a photon, with energy greater that the energy band gap, E_g, is incident within the crystal. Figure 2.6 shows the change in the energy band diagram due to the excitation of an electron from the valence band to the conduction band leaving behind a hole.

2.2.1 Doping of semiconductors

For a pure semiconductor, the density of the thermally generated charge carriers is small at room temperature, for example, 10^{10} cm^{-3} for Si and 10^{7} cm^{-3} for GaAs. Such a pure semiconductor is typically referred to as an intrinsic semiconductor. Figure 2.7 illustrates an intrinsic Si semiconductor with a representative energy band diagram at room temperature. Such lower concentrations of charge carriers, which results in a lower conductivity of the intrinsic semiconductor, may not be useful in solid state electronics and necessities increases in the concentration of charge carriers so as to improve the conductivity. The conductivity of a semiconductor may be increased by intentionally adding impurities, or foreign atoms, to an intrinsic semiconductor. This process is referred to as doping and the resulting semiconductor is referred to as an extrinsic semiconductor.

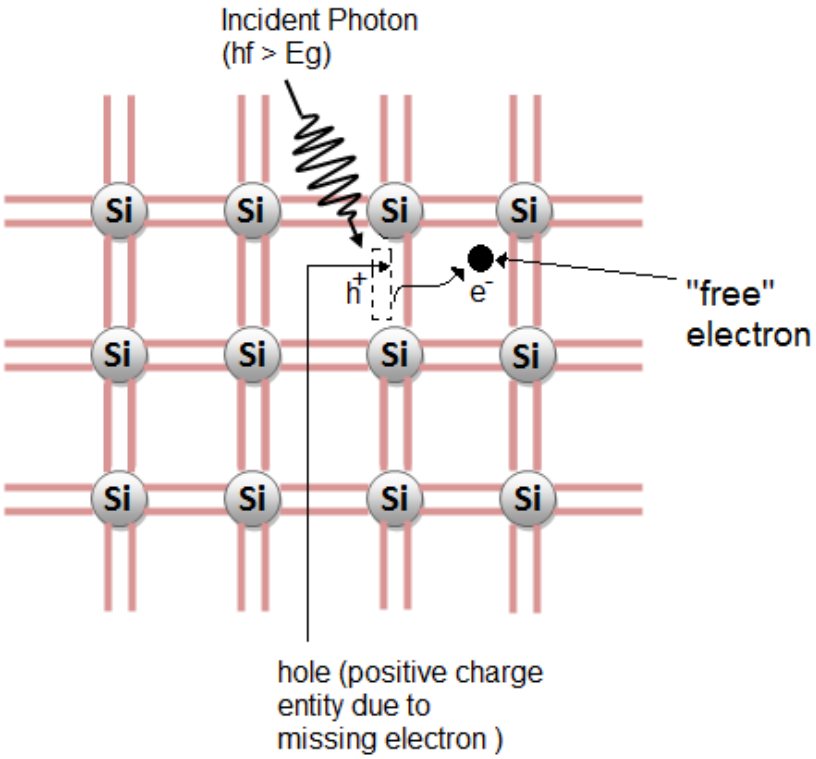

Figure 2.5: The breaking of “free” electron (e-) and thereby leaving a net positive charge entity called hole (h^+), within a Si crystal due to thermal energy absorption, which breaks some of the covalent bonds. This figure is adapted from Kasap [23]. The online version of this figure is in color.

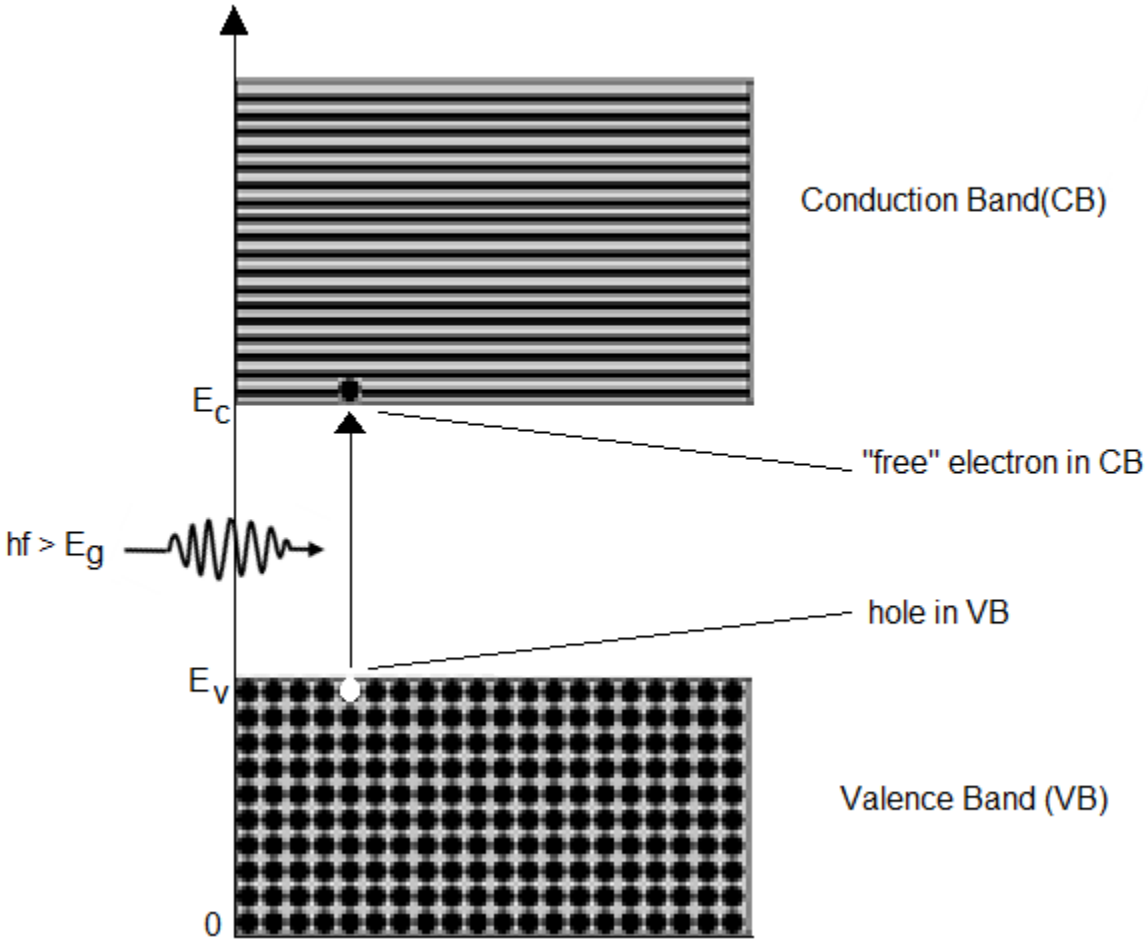

Figure 2.6: Energy band diagram showing the excitation of an electron from the valence band into the conduction band due to the absorption of an incident photon of energy with $hf > E_g$. This figure is adapted from Kasap [23].

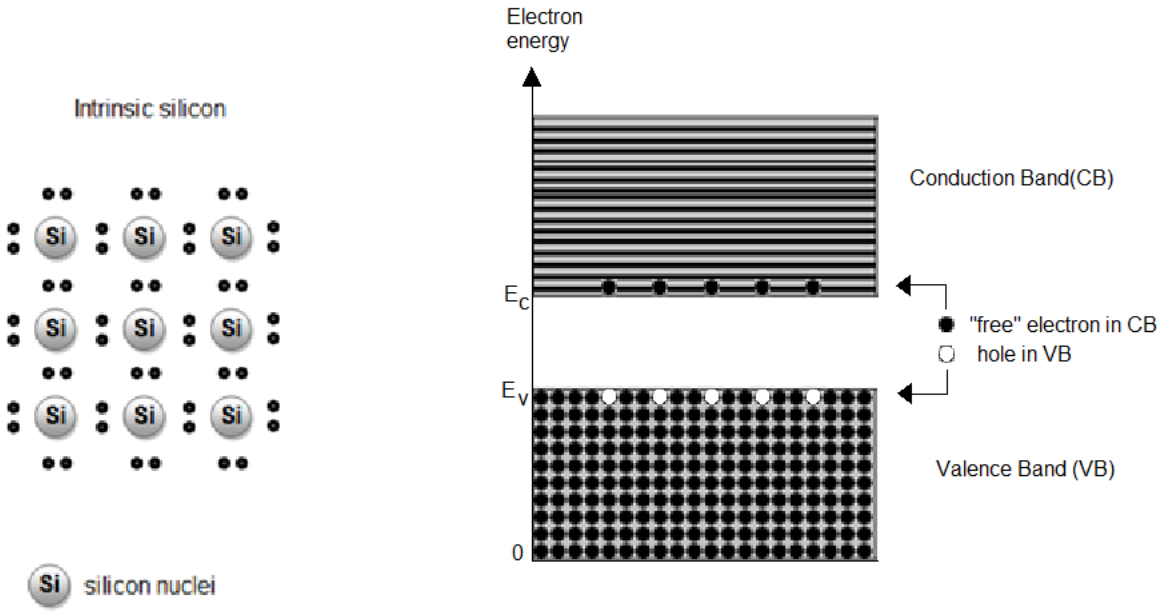

Figure 2.7: Intrinsic Si semiconductor and its typical energy band diagram at room temperature. This figure is adapted from Hu [25].

When a pentavalent element, such as phosphorus (P), is added in small quantities to the crystal lattice of Si, the P atoms displace some of the Si atoms in the crystal. The small amount of impurity atoms (one P atom for every million Si atoms) ensures that the P atom bonds with the Si atoms in the same diamond crystal lattice. While four of the five valence electrons of the P atom are shared with four neighboring Si atoms, thus forming a covalent bond, the fifth valence electron escapes and becomes a mobile electron orbiting around the P nucleus. This results in an excess of electrons in the crystal lattice which is loosely bound to the P atom. The excess electron gains sufficient energy and become free to move within the crystal lattice. The creation of such free electrons around immobile P^+ ions forms an n-type Si semiconductor with a typical energy band diagram at room temperature, as shown in Figure 2.8. The energy required to release the "free" electrons orbiting around the P^+ ion into conduction band is very small (32 meV for Si at room temperature). This small energy, also referred to as the binding energy, can be readily supplied by the average energy of a thermal vibration at room temperature, which is typically 70 meV. By controlling the concentration of impurity atoms, the required concentration of the free or mobile electrons for the desired electrical conductivity, can be obtained. In this process, there is no hole creation associated with the process of the creation of electrons and the semiconductor thus formed is referred to as an n-type semiconductor, which has an excess of one type of charge carrier, i.e., electrons.

Similarly, when a trivalent element, such as boron (B), is used to replace the silicon atoms in the crystal lattice, three valence electrons of the impurity B atom (B) form covalent bonds with three of the four neighboring Si atoms. This results in one of the bond missing one electron to complete the bond.

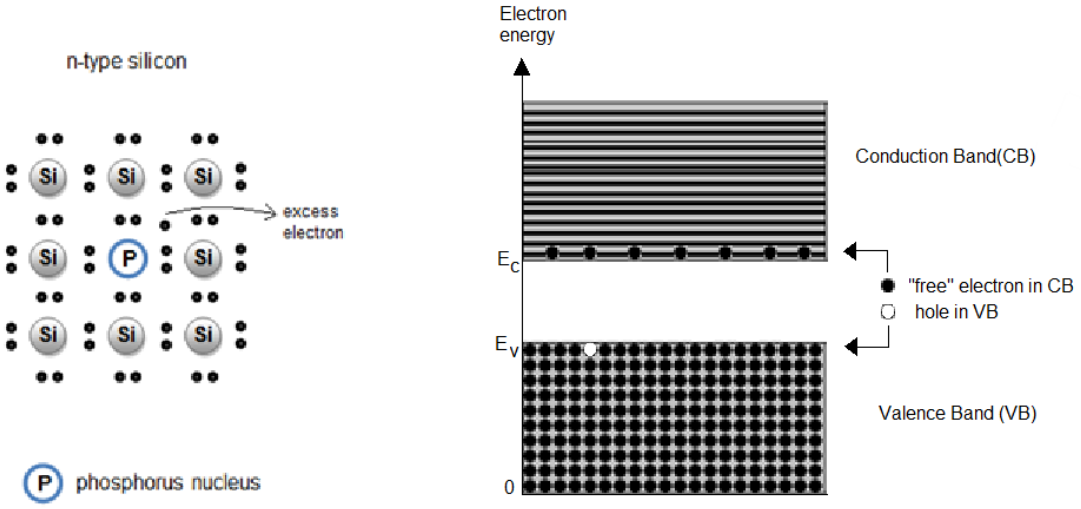

Figure 2.8: An n-type Si semiconductor and its typical energy band diagram at room temperature. This figure is adapted from Hu [25].

This void or absence of an electron, created in the lattice, is termed as a hole, which is a positive charge entity. It refers to an empty electronic state in the valence band. With the hole thus formed, an electron from the nearest neighboring Si atom can tunnel and occupy the empty state, which is equivalent to the hole being displaced in the opposite direction. This hole orbits around the negatively charged B ion before gaining sufficient energy, through the absorption of thermal energy, to move away from the B ion. The binding energy is very small (for example, 50 meV for Si at room temperature) and is therefore easily supplied by the average energy of lattice vibration due to the thermal energy. Figure 2.9 shows p-type Si semiconductor formed by doping it with B atom and the associated typical energy band diagram at room temperature.

2.2.2 Carrier concentration and Fermi Function

The electrical conductivity of the semiconductor material can be ascertained based on knowledge of concentration of the charged carriers (electrons in the conduction band and holes in the valence band). The conduction band of a semiconductor can be thought of as being comprised of number of allowed empty energy levels. The concentration of electrons is related to the density of these available states, $g(E)$, and the probability that each of these states is occupied. i.e., the number of allowed energy levels in the conduction band and the likelihood of these states being populated by an electron. This likelihood, or the probability, of a given energy state being occupied by an electron is given by the Fermi-Dirac distribution function, $f(E)$. The product of the density of states and the Fermi–Dirac probability function gives the number of electrons per unit energy per unit volume in the conduction band. Integrating this

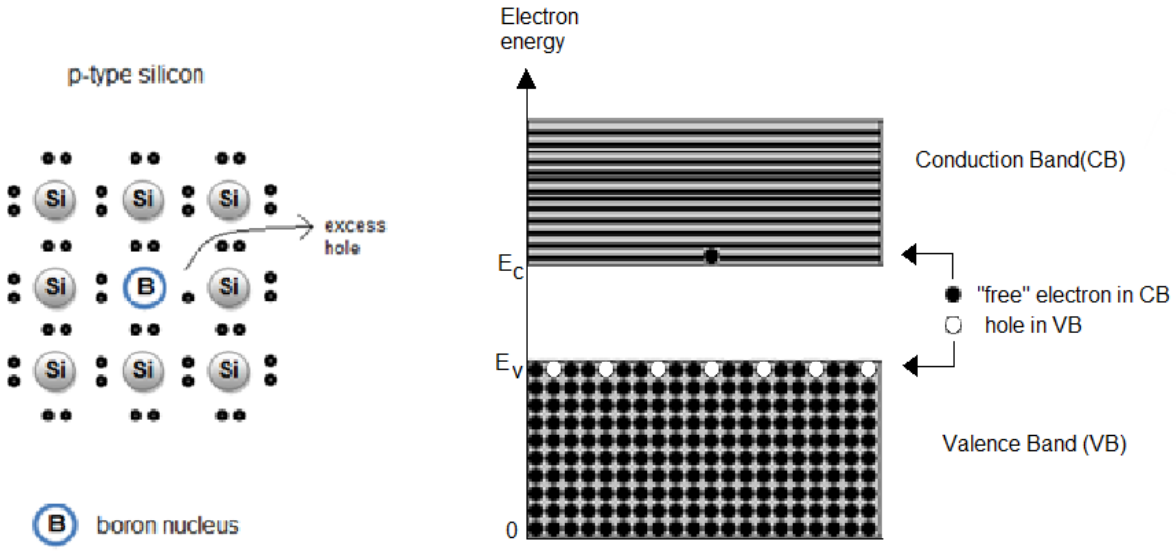

Figure 2.9: A p-type Si semiconductor and its typical energy band diagram at room temperature. This figure is from Hu [25].

product over the entire conduction band gives the concentration of electrons. As for the density of holes, i.e., empty state in the valence band, the probability of having a hole equals the probability that a particular state is not filled. Hence, the product of the probability of the state being empty and the density of the state in valence band gives the concentration of holes in the valence band.

For intrinsic Si, since the electrons and holes are generated in pairs, there is an equal concentration of electrons in the conduction band and holes in the valence band. Furthermore, for a symmetric distribution of parameters, at the edge of the conduction and valence bands, there will be equal number of states. This suggests that the probability of finding an electron in a conduction band state is equal to the probability of finding a hole in a corresponding valence band state. Therefore, the Fermi level, E_F, for the case of intrinsic Si, appears at the middle of the band gap, as depicted in Figure 2.10 (a). For n-type Si, there are more electrons in the conduction band than there are holes in the valence band, which suggests that the probability of finding an electron near the conduction band edge is greater than the probability of finding a hole at the valence band edge. Therefore, the Fermi level is closer to the conduction band in an n-type Si, as depicted in Figure 2.10 (b). For p-type Si, however, there are more holes in the valence band than there are electrons in the conduction band, suggesting that the probability of finding an electron near the conduction band edge is less than the probability of finding a hole near the valence band edge. Therefore, the Fermi level is closer to the valence band edge in a p-type semiconductor, as depicted in Figure 2.10 (c).

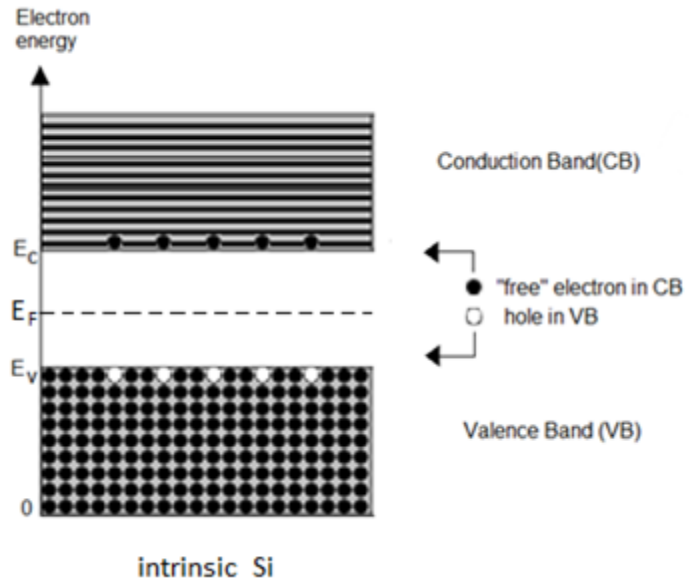

(a)

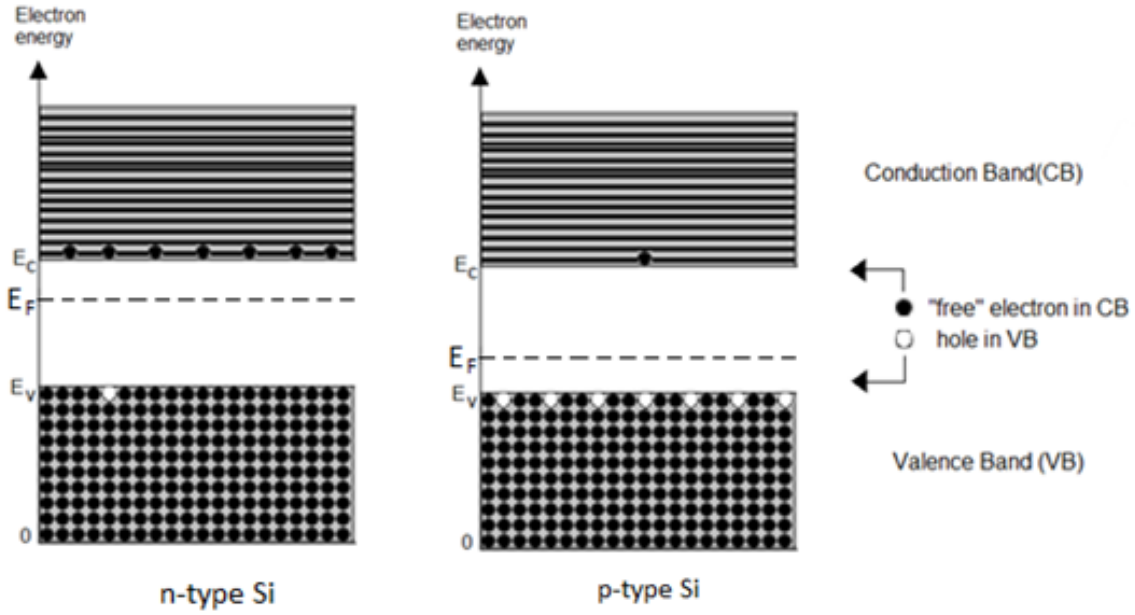

(b) (c)

Figure 2.10: Energy band diagram with the Fermi level indicated for (a) intrinsic, (b) n-type, and (c) p-type Si. This figure is after Kasap [23].

2.2.3 p-n junction

A p-n junction is formed when an n-type semiconductor is interfaced with a p-type semiconductor forming the very basic building block of modern day electronics. Figure 2.11 shows the formation of a p-n junction due to the interfacing of n-type and p-type semiconductors and the associated energy band diagram of the p-n junction. The metallurgical junction thus formed possesses rectifying properties in the sense that current can flow in one direction easily while the flow of current in the opposite direction is limited to a very small leakage current. As a result of doping, there are large numbers of electrons on the n-side, but very few on the p-side. Similarly, there are large numbers of holes on the p-side with very few holes on the n-side. When these two types of semiconductor are brought together to form the p-n junction, electrons from the n-side diffuse to the p-side due to the concentration gradient resulting in a depletion of electrons on the n-side near the junction. With this, the conduction band edge, E_C, moves away from E_F at the n-region towards the metallurgical junction. Similarly, holes diffuse from the p-side to the n-side due to the concentration gradient, depleting the p-region near the junction of holes. This causes the valence band edge, E_V, to move away from E_F towards the junction. At the junction, the Fermi level, E_F, is close to neither E_C nor E_V, indicating that the charge carrier concentrations are much less than that in the neutral region.

The diffusion of electrons from the n-side towards the p-side leaves behind positively charged immobile ions near the metallurgical junction on the n-side. Similarly, holes in the p-type region diffuse towards the n-type side, leaving behind negatively charged boron ions. This forms a region depleted of

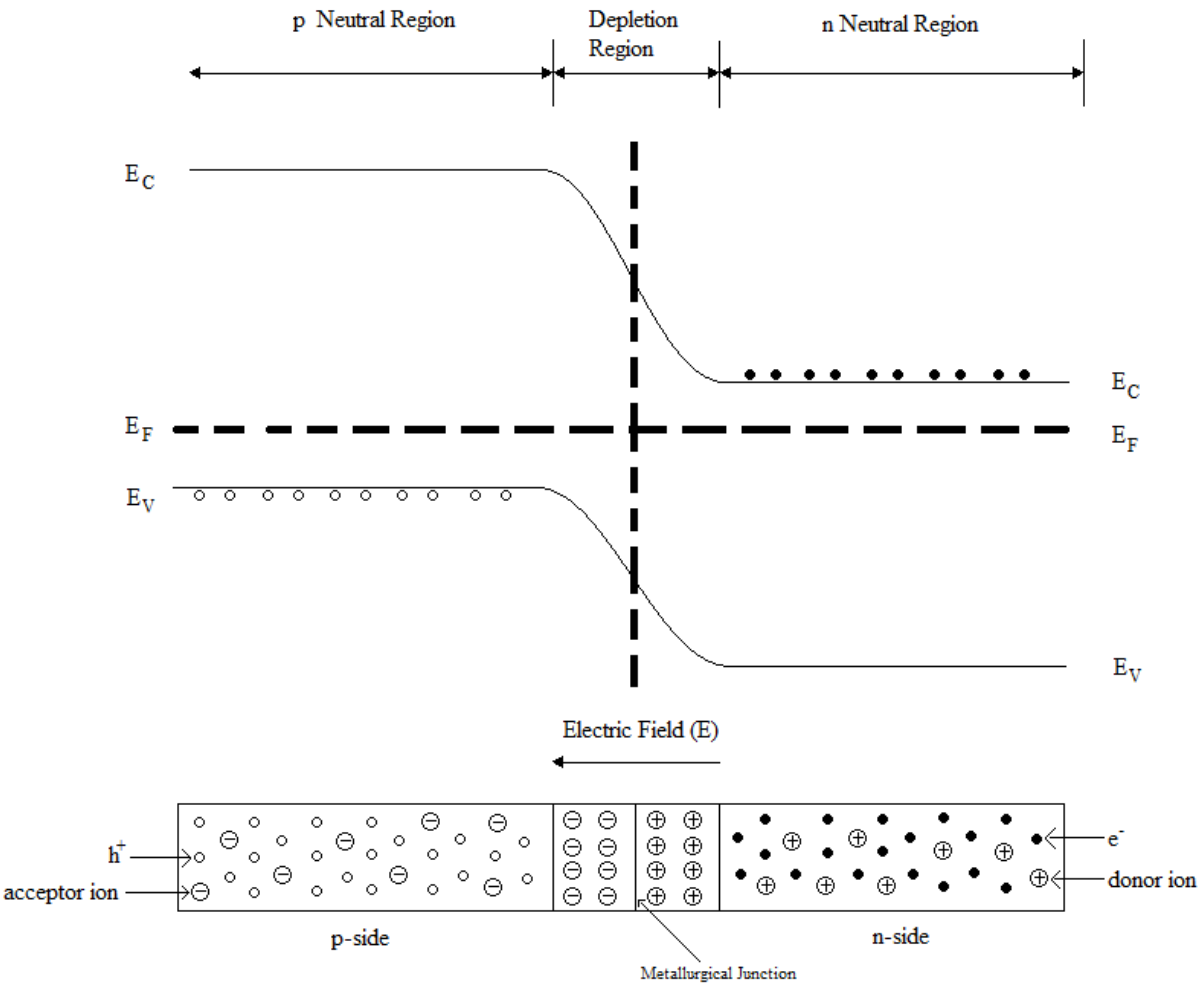

Figure 2.11: A p-n junction and the corresponding energy band diagram associated with such a junction.

This figure is adapted from Kasap [23].

charge carriers, referred to as the depletion region, near the junction. The fixed ions left behind set up an electric field at the junction, resulting in a “built-in” potential across the junction. Under the influence of “built-in” electric field, some of the electrons and holes to drift in the opposite direction to the flow caused by diffusion, i.e., electrons or holes near the junction are swept back into its original volume. Thus, at the junction, there are two effects occurring; electrons diffusing from the n-side to the p-side due to the concentration gradient and electrons drifting under the influence of the “built-in" electric field back into the n-side. A similar argument applies to the holes, but in the opposite direction. Eventually, the current component due to diffusion of electrons is balanced by the current component due to the drift of electrons under influence of the “built-in” potential, resulting in a zero-net current.

When the p-n junction is forward-biased with the application of positive voltage to the p-side, current can flow, which depends on the magnitude of the applied bias voltage. With this, the applied electric filed is in opposition to the "built-in" electric field, so that the resultant field at the junction is smaller. The electrons on the n-side can now easily overcome the potential barrier and diffuse to the p-side. In silicon, this occurs at about 0.6 V forward bias. When a negative voltage is applied to the p-n junction, to reverse-bias the junction, the “built-in” electric field and the applied field are in the same direction such that the resultant field is at the junction is large. In this case, a negligible reverse saturation current will flow across the junction. Solar cells operate as p-n junctions under forward-bias conditions.

2.3 Structure of photovoltaic solar cell

Doped semiconductors are used to fabricate photovoltaic solar cells which as suggested earlier

consist of n-type silicon interfaced with p-type silicon, effectively forming a p-n junction. The choice semiconductor material to be used for the fabrication of a photovoltaic solar cell is governed by two factors; how well the semiconductor absorbs light and how economical the cost of fabrication is. Therefore, silicon (Si), with fairly good absorption characteristics and well developed and a cost effective fabrication technology, is a predominantly used semiconductor for photovoltaic solar cell fabrication, albeit other semiconductors, such as gallium arsenide, and cadmium telluride, etc., with better absorption characteristics, are available [7]. The ability of semiconductor materials to absorb photons incident from the sunlight and generate free charge carriers (electrons and holes) for electrical conductivity is a key concept underlying the operation of photovoltaic solar cells. Figure 2.12 illustrates the structure of a typical photovoltaic cell.

Photovoltaic solar cells are large area p-n junction diodes formed by interfacing a layer of p-type silicon with another layer of n-type silicon, with the n-layer on top (sun facing side) of the p-layer. The n-layer and p-layer are selectively formed on a single bulk Si wafer through doping to form a metallurgical junction (p-n junction), which separates the charge carrier pairs, i.e., electrons and holes, generated by the sunlight. The top surface of the photovoltaic cell is exposed to solar radiation for the absorption of incident energy. A thin metallic grid on the top surface forms the front electrode, which allows for the maximum amount of sunlight to be absorbed into the diode and carry the electrical current, thus generated, into the preferred direction. The top surface (between the metallic grids) has a layer of anti-reflective coating to minimize surface reflection. A metallic layer, deposited on the back of the

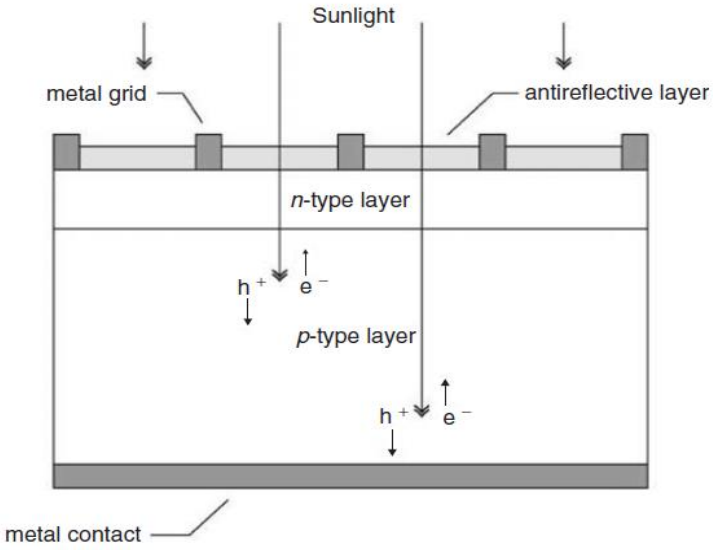

Figure 2.12: Cross-section of a typical photovoltaic solar cell. This figure is adapted from Kasap [23].

photovoltaic solar cell, forms the back electrode. The two electrodes, when connected to the load through external wiring connection, complete the circuit.

2.4 Operation of a photovoltaic solar cell

As the photovoltaic solar cell is basically a p-n junction, at finite temperature, in the region near the junction, the diffusion of charge carriers from either side of the junction leaves behind positively charged ions on the n-side and negatively charged ions on the p-side. The immediate vicinity of the metallurgical junction is depleted of charged carriers, and thus, is appropriately termed the depletion region or the space-charge region. The "built-in" electric field developed across the space-charge region deters further diffusion of charge carriers and separates them on either side of the junction. When such a p-n junction is illuminated with electromagnetic radiation, such as sunlight, it results in the generation of electron-hole pairs in the bulk of the silicon. Solar radiation is comprised of discrete packets of energy, known as photons; these photons are absorbed resulting in the generation of electrons and holes. The amount of energy within each photon depends on the wavelength of the radiation. The motion of these generated charge carriers generates an electric current when the two terminals are connected externally. For the generation of such charge carriers, the energy in the incident photon has to be greater than the energy band gap, E_g, such that it can break "free" electrons from the covalent bonds. Any photon with energy less than the energy band gap simply passes through the bulk and does not contribution to the electrical current. For the case of photons with energy greater than the energy band gap, the excess energy is dissipated as heat in the crystal lattice. The thickness of the n-type and p-type layer within the

photovoltaic solar cell is optimized for the maximum absorption of photons and subsequent charge carrier generation. A typical photovoltaic solar cell, with incident photons and charge carriers generated as a result, is depicted in Figure 2.13.

2.5 Solar Spectrum

The spectral distribution of the incident solar radiation dictates the energy conversion capability of the photovoltaic solar cell. The energy generated by a photovoltaic solar cell depends on the amount of photon flux incident on it and the energy associated with such photons. As sunlight can be thought of as streams of photons of different wavelength, the energy associated with each photon, E_λ, is given by Eq (2.1), as,

$$E_\lambda = \frac{hc}{\lambda} \qquad \text{…….. (2.1)}$$

where h is Planck's constant, c is the speed of light, and λ is the wavelength of the associated radiation. The emission of radiation from the Sun, which has a surface temperature of about 5300 K, can be approximated by black body radiation at the surface temperature. The distance travelled (150 million kilometers) to reach the Earth and the influence of the Earth's atmosphere alters the radiation intensity of the sunlight. The solar radiation intensity at just above the Earth's atmosphere is defined as extraterrestrial solar radiation while the radiation intensity that reaches Earth's surface, after passing through the atmosphere, is termed as terrestrial solar radiation. The difference in the spectral distributions is characterized with a coefficient referred to as the "air-mass (AM)", which basically defines the influence of the atmosphere on the spectral content and the change in the spectral distribution with

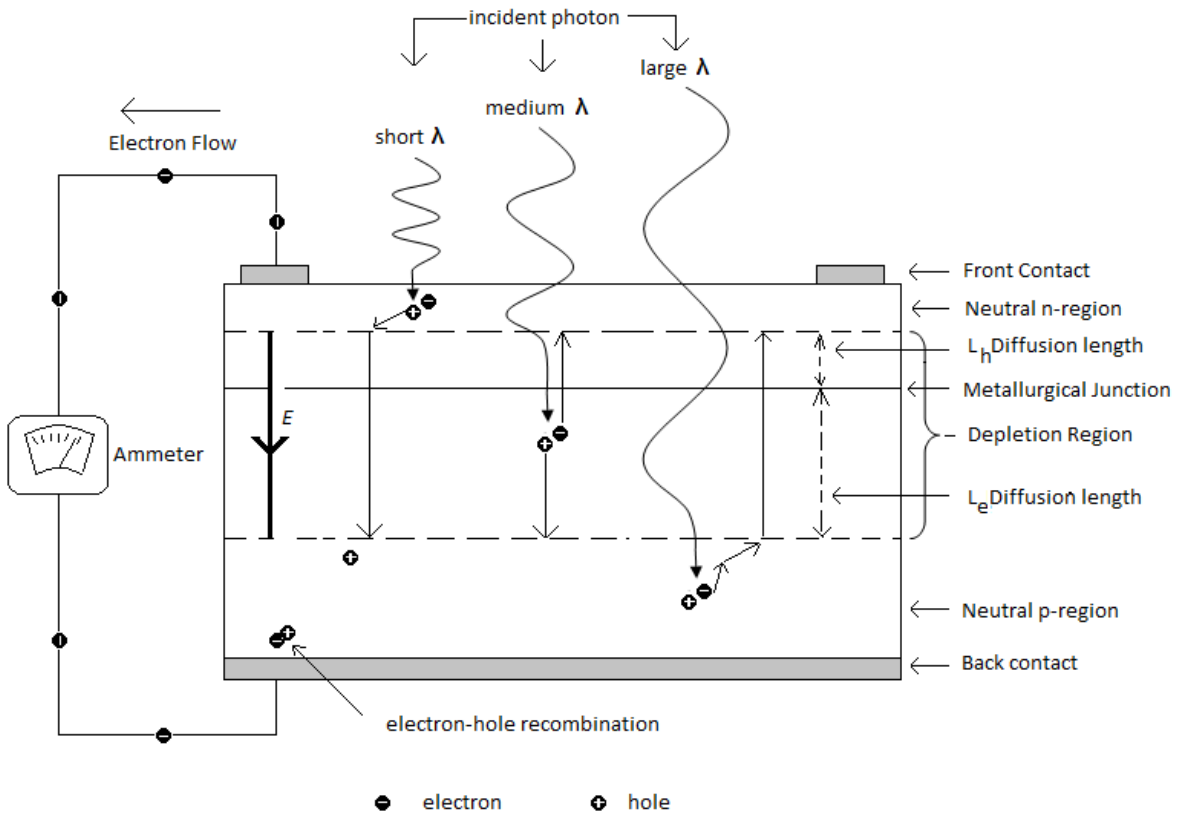

Figure 2.13: A typical photovoltaic solar cell with p-n junction between front and back electrical contact. The incident photons generate electron-hole pairs within the solar cell which are then collected by the electrodes. This figure is adapted from Kasap [23].

respect to the optical path length. The air-mass (AM) number can be given by Eq. (2.2),

$$Air\ Mass\ (AM) = \frac{1}{cos\theta} \quad \text{…….. (2.2)}$$

where θ is the angle of incidence with respect to zenith.

In extraterrestrial space, the intensity of the radiated solar energy is 1.353 kW·m^{-2} and the spectrum is referred to as air-mass 0 (AM0) [7]. Photovoltaic solar cells designed for space applications, such as satellites, are generally characterized using AM0. Similarly, the spectral content at sea level, when the solar radiation has traversed through the Earth's atmosphere with the Sun exactly at zenith, is characterized by air-mass 1 (AM1) with an angle of incidence of 0°. For all practical purposes for terrestrial applications, the solar spectrum is defined by the standard air-mass 1.5 (AM1.5) spectral distribution with an integrated power density of 1 kW·m^{-2}. AM1.5 has two spectral distributions defined to account for direct sunlight and the diffused component of sunlight. For the sake of uniformity in comparison and evaluation, the electrical (power) output of commercial photovoltaic solar cells is generally measured under standard testing conditions. Standard testing conditions are industry-wide standards to rate the performance of photovoltaic cells or modules and are described by the cell temperature of 25°C and an irradiance of 1 kW·m^{-2} with an air-mass 1.5 (AM1.5) spectrum. Figure 2.14 shows the spectral distribution of a black body radiation along with that of extraterrestrial solar radiation and terrestrial solar radiation.

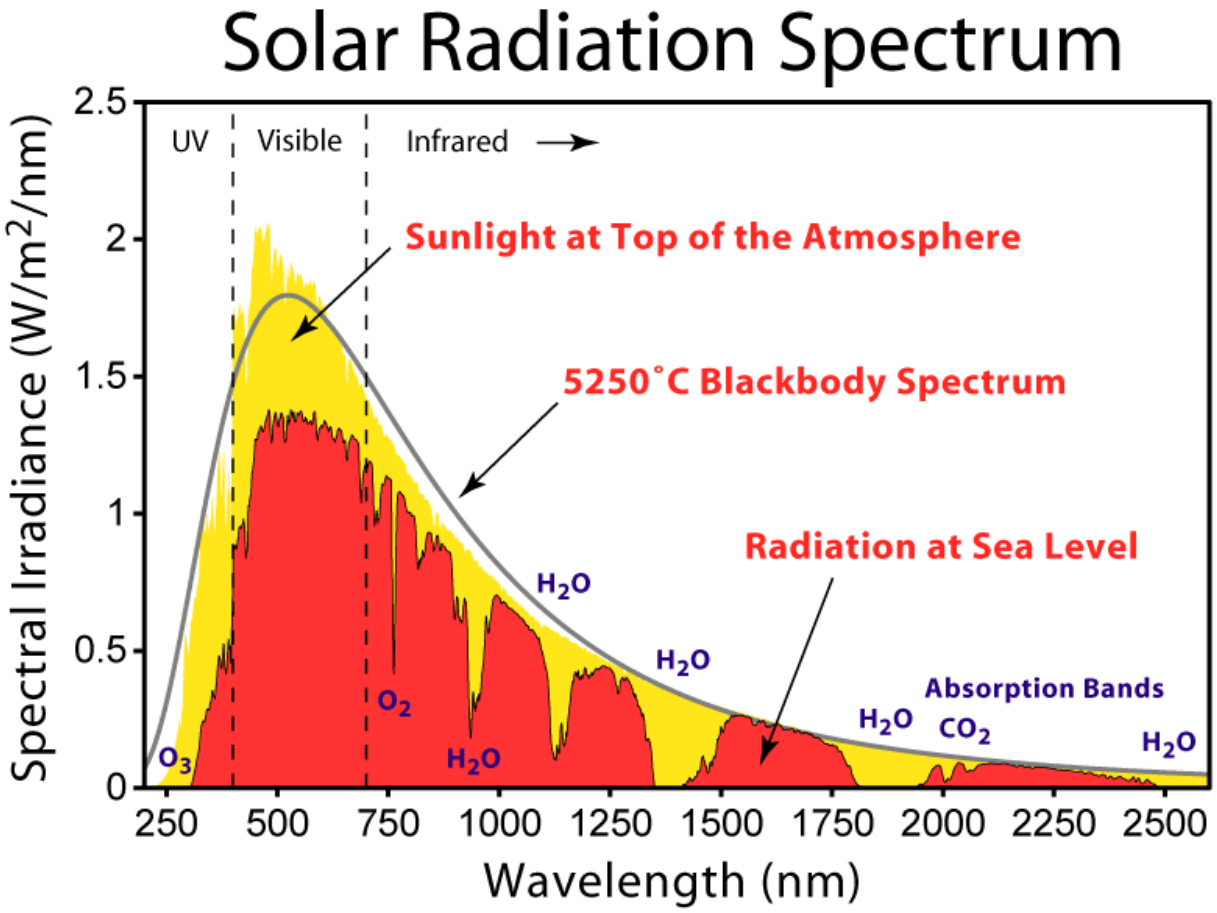

Figure 2.14: Spectral distribution of black body radiation, at the top of the Earth's atmosphere and sea level. Image by Robert A. Rohde, used under Creative Commons Attribution-Share Alike 3.0 Unported. The online version of this figure is in color.

2.6 Photovoltaic solar cell and I-V characteristic curve

Photovoltaic solar cells are grouped together in special arrangements of series and parallel connections to form a photovoltaic module (panel). The module delivers required voltages and currents to its terminals. Many such photovoltaic modules are connected in a special arrangement of series and parallel connections to form photovoltaic arrays. They can be directly connected to drive DC loads or through inverters for the requirement of AC transmission or usage. Under illumination, a photovoltaic cell (or module or array) produces an electrical current and dc voltage at its terminal. The currents and voltages thus generated can be represented by the current-voltage characteristic curve, which gives ideas about the photovoltaic solar cell power generation capacity and efficiency. The amount of current and voltage depends upon the amount of incident sunlight and temperature of the photovoltaic solar cell. Similarly, the product of current and voltage at each point, which translates to the power output, can be represented by similar curves, called the power-voltage characteristic curve.

Photovoltaic devices exhibit a non-linear current-voltage characteristic, and consequently, a non-linear power-voltage characteristic, as illustrated in Figure 2.15, results. The current-voltage characteristic describes the current as a function of the voltage corresponding to a given photovoltaic device, giving a detailed description of its solar energy conversion ability and efficiency. The current-voltage characteristic of a photovoltaic device is strongly influenced by the device temperature and the intensity of the solar radiation, particularly, the output voltage being strong function of the temperature and the output current being a strong function of the incident irradiance. A typical current-voltage characteristic of a

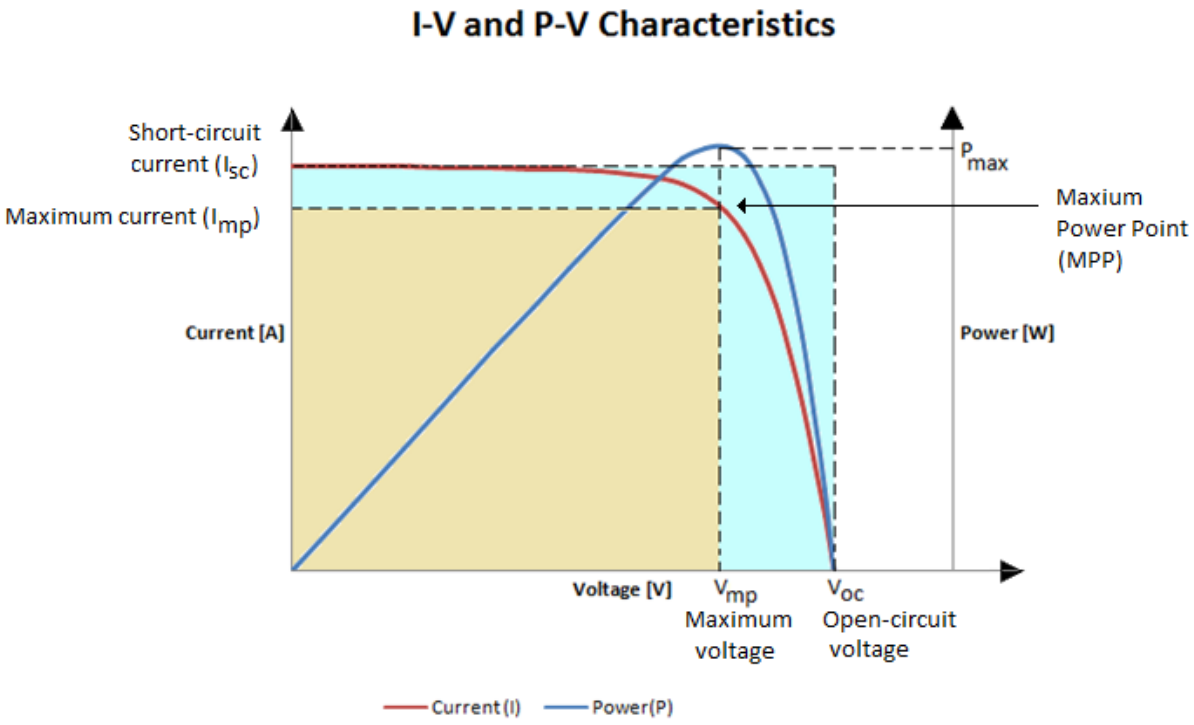

Figure 2.15: Representative current-voltage and power-voltage characteristic curves corresponding to a photovoltaic device i.e., solar cell or module. The online version of this figure is in color.

photovoltaic device, as shown in Figure 2.15, exhibits three significant points: the short-circuit point, the open-circuit point, and the maximum-power point. These significant points are figures-of-merits upon which the energy conversion ability and efficiency of a photovoltaic solar cell may be characterized. The open-circuit voltage, V_{oc}, is the maximum voltage that the photovoltaic device provides when the terminals are not connected to any load, i.e., when the photovoltaic device is in an open- circuit condition. The short-circuit current, I_{sc}, corresponds to the current provided by the photovoltaic device when its terminals are shorted together, i.e., under a short-circuit condition. When short-circuited, the voltage across the photovoltaic device is at zero, and the current flowing out of the photovoltaic device is referred to as the short-circuit current. Independent of these two extremes in the current-voltage characteristic, i.e., V_{oc} and I_{sc}, respectively, neither of these two conditions corresponds to the generation of any electrical power. In between these two points, however, there is a point, referred to as the maximum-power point (MPP), where the power supplied by the photovoltaic device, connected to a load, is at its maximum value. The voltage and current corresponding to the maximum power point are referred to as the voltage at the maximum power point, V_{mp}, and the current at the maximum power point, I_{sc}, respectively.

Two additional figures-of-merit, namely the fill-factor and the efficiency, are also used to describe the performance capability of a photovoltaic device. The fill-factor, FF, is the ratio of the maximum power delivered by the photovoltaic device and the product of the open-circuit voltage times the short-circuit current (V_{oc} x I_{sc}). It is a measure of how well the photovoltaic device is capable of converting the

available energy supplied by the Sun into electrical energy. It may be expressed as

$$FF = \frac{I_{mp}V_{mp}}{I_{sc}V_{oc}}. \quad \text{..... (2.3)}$$

The efficiency, η, is the ratio of the maximum electrical power produced compared to the total solar energy incident on a given photovoltaic device, i.e., it provides for the fraction of the incident solar power that may be delivered to the load. The efficiency may be expressed as a percentage, i.e.,

$$\eta_{(\%)} = \frac{I_{mp}V_{mp}}{P_{in}} \times 100\,, \quad \text{..... (2.4)}$$

where P_{in} is the incident solar irradiance on the surface area of the photovoltaic device.

2.7 Commercial manufacturing and performance testing

Photovoltaic solar cells are grouped together in series and parallel combinations in order to form a solar module which outputs a certain level of voltage and current that is used for practical applications. Parallel combinations of photovoltaic solar cells increase currents while a series combination of photovoltaic solar cells increases voltages. In the process of solar module assembly, multiple photovoltaic solar cells (36, 54, 60, 72 being popular combinations) are soldered together to form a string. A string of photovoltaic solar cells is laid out in between two layers of encapsulants, such as EVA (Ethylene Vinyl Acetate), which provides optical and electrical transmissivity and keeps out moisture. This ensemble is then laminated with a toughened glass on top and a polymer backsheet on the back. Metal (often

aluminum) frames are fixed along the edge in order to support the mounting on the panel and provide mechanical strength. Figure 2.16 shows the steps of the solar module assembly process within a representative solar module manufacturing plant.

2.8 Post production performance rating (flash tester or solar simulator)

After the final stage of production, every photovoltaic solar module must be tested for output performance by measuring its current-voltage characteristics, under standard testing conditions. For uniformity across the industry, photovoltaic solar modules are tested in standard testing conditions, which translates to 25°C of device temperature and an irradiance intensity set to 1000 $W \cdot m^{-2}$ with an air-mass 1.5 spectrum. This test is conducted by means of a solar simulator (or what is more commonly known as a flash-tester) wherein the photovoltaic solar modules is exposed to a short pulse of light produced by an artificial source, such as a xenon arc lamp, whose spectrum is close to that of solar radiation. A typical flash-tester setup is depicted in Fig 2.17. The bias voltage across the photovoltaic solar module is varied, and the corresponding current generated as a response to the incident light, is measured. In addition to the current, voltage, and power levels, the measurement results of the flash tester also record the maximum rated power, open-circuit voltage, short-circuit current, maximum-power voltage, maximum-power current, temperature coefficient, fill-factor, efficiency, etc. Module parameters, thus measured under standard testing conditions, are then printed on a label on the back of the module for future reference.

Figure 2.16: A flash tester (Class AAA solar simulator) measuring the current-voltage characteristics of photovoltaic devices. The online version of this figure is in color.

2.9 Models of photovoltaic solar cell and equivalent electrical circuit

As is evident from Figure 2.15, photovoltaic devices exhibit nonlinear current-voltage characteristics. Typically, the electrical characteristics of a photovoltaic device are represented by an equivalent circuit model, as shown in Figure 2.18. This particular equivalent circuit model is known as the single-diode circuit model of a photovoltaic device. The circuit model consists of a current source driven by sunlight in parallel with an ideal diode with a shunt and series resistance [26]. Mathematically, the current-voltage characteristics associated with this circuit model can be represented as,

$$I = I_{ph} - I_{sat}\left(exp\left(\frac{qV}{nk_BT}\right) - 1\right) - \frac{(V+IR_s)}{R_{sh}}, \quad \text{..... (2.5)}$$

where I is the output current at the terminals, V is the output voltage across the terminals, I_{ph} is the photo-generated current, I_{sat} is the diode reverse saturation current, representing the diffusion mechanism, η is the diode ideality factor, R_s is the series parasitic resistance, and R_{sh} is the shunt parasitic resistance, k_B is Boltzmann's constant (1.38 x 10^{-23} joules per Kelvin), T is the temperature for the p-n junction (normally set to room temperature, i.e., 298 K), and q is the charge of the electron (1.9x10^{-19} C). Within the framework of this circuit model, the current-voltage characteristic may be specified through knowledge of the parameters, such as $I_{ph}, I_{sat}, n, R_s,$ and R_{sh}.

Increased accuracy in modeling the behavior of photovoltaic device can be achieved with models with increased complexity. Including a second diode, for example, in order to account for the recombination of charge carriers, is often used [27]. Such a circuit model is termed as the double-diode

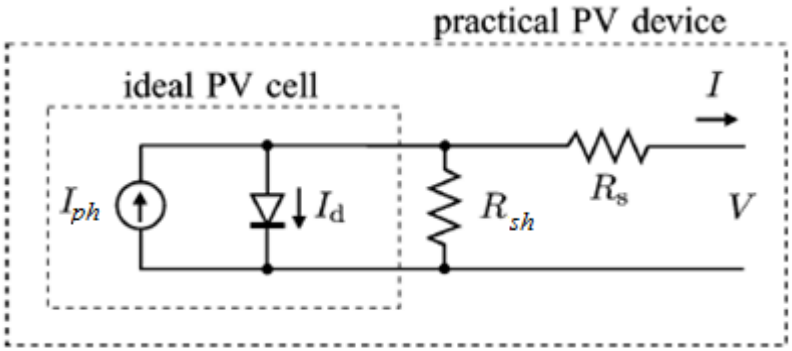

Figure 2.17: A single diode circuit model representing the current-voltage characteristic associated with a photovoltaic device.

circuit model. Figure 2.19 shows the equivalent circuit model representing the double-diode circuit model.

Mathematically, the corresponding current-voltage relationship may be expressed as

$$I = I_{ph} - I_{sat1}\left(exp\left(\frac{qV}{n_1 k_B T}\right) - 1\right) - I_{sat2}\left(exp\left(\frac{qV}{n_2 k_B T}\right) - 1\right) - \frac{(V+IR_s)}{R_{sh}}, \quad \text{..... (2.6)}$$

where,

- R_s is the series resistance of the solar cell,
- R_{sh} is the shunt resistance of the solar cell resulting from defects within cell's crystal structure,
- I_{ph} is the photo-generated current,
- I_{sat1} is the reverse saturation current for diode 1 to represent the diffusion mechanism,
- I_{sat2} is the reverse saturation current for diode 2 to represent the recombination mechanism,
- n_1 and n_2 are the ideality factors associated with diodes 1 and 2, respectively.

From a modeling perspective, the accuracy achieved by the single-diode model is often viewed as being adequate; therefore, the double diode model will not be considered for the purposes of this analysis.

It is evident from Eqs. (2.5) and (2.6), that the behavior of a photovoltaic solar cell may be represented by a non-linear equation, with five parameters, for the case of the single-diode model, or the seven parameters, for the case of double-diode model. Therefore, modeling of a photovoltaic solar cell (or module) becomes a two-step process. The first step is to identify the five parameters (single-diode model) depending on the type of model used and, in the second step, use those estimated parameters to get the corresponding current-voltage characteristics. This can be done in two ways. The problem can be

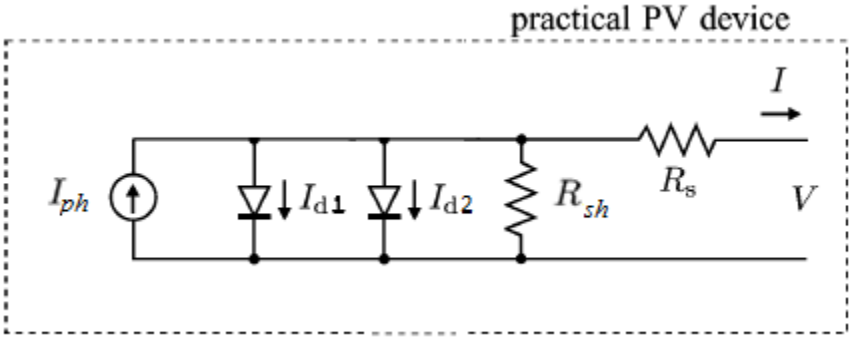

Figure 2.18: Double-diode circuit model representing the current-voltage characteristic associated with a photovoltaic device.

either solved through numerical methods, which rely on powerful mathematical tools, such as iterative methods, to solve the implicit nonlinear equations, or by analytical methods, which introduces a round of simplifications and approximations, and produces simpler solutions to the model with acceptable accuracy [28].

2.10 Analytical Approach

Ample literature is available that suggests the use of various forms of approximations and simplifications to arrive at a reasonably accurate estimation of the parameters for the solutions of the non-linear implicit transcendental equation. The analytical approach of parameter extraction offers relatively simple and convenient computational steps towards the solution. Such approaches use certain significant data points of the current-voltage curves, such as the open circuit voltage (V_{oc}), the short circuit current (I_{sc}), the maximum power voltage (V_{mp}), and the maximum power current (I_{mp}) to solve a system of equations. This scheme of solution is computationally fast but the accuracy of the extracted parameters depends on the selected points on the current-voltage curve [29]. Many authors have adopted the analytical approach for the modeling of photovoltaic systems.

Building upon the five sets of equations, suggested by Kennerud [26], obtained by evaluating the single-diode equation with values of $V_{oc}, I_{sc}, V_{mp}, I_{mp}, R_{so}$ and, R_{sho}, Phang *et al.* [30] suggested using typical parameters values of a standard photovoltaic solar cell at standard testing conditions, to make inference and approximations that can be made to arrive at simple analytical expressions for the five parameters. Using the typical parameter values of a standard 3” photovoltaic solar cell at standard testing

conditions, the authors arrived at five simplified analytical expressions for the parameters based on the approximations deduced. The authors examined the error associated with the estimated values for the five parameters, i.e., $R_s, R_{sh}\ I_{ph}, I_o$, and n based on a numerical approach to that of the analytical approach, for two different cells. For suitably selected values of R_s and R_{sh}, the authors claim that the error contours (within the error grid of R_s and R_{sh}) of the extracted parameters, were within 1% and 4% for the two cells using experimental data retrieved from Charles *et al.* [31]. The authors claim that this approach offers a simple and rapid determination of parameters.

Furthermore, Phang *et al.* [27], in order to improve the accuracy of the extracted parameters, suggest adopting a double-diode model instead of the single-diode model in their analysis. Here again, the double-diode equation was evaluated at significant points, and the derivative of the double-diode equation were expressed at the V_{oc}, I_{sc}, and P_{mp} points. Based on typical values of a standard photovoltaic solar cell, some approximations were made by the various authors, which helped deduce four expressions for four of the parameters, R_{sh}, I_{ph}, I_{sat1}, and I_{sat2}. Additionally, for the series resistance, R_s, further manipulation of such expressions produced a non-linear equation in terms of the series resistance, R_s. Quadratic or cubic solutions of the expression thus obtained were used to solve for R_s. With R_s known, the remaining four parameters were identified using the analytical expressions.

Villalva *et al.* suggest one approach to finding the parameters of a photovoltaic solar module by adjusting the current-voltage curve at three significant points: the open-circuit voltage, the short-circuit current, and maximum power point [32]. The authors suggest that for only one pair of series and shunt

resistances, the modeled power will be the same as the experimental power within a defined tolerance. The author uses expressions derived from the single-diode equation to obtain the values of three parameters, I_{ph}, I_{sat}, and n, while values of R_s are varied starting, from 0, with small steps and the corresponding R_{sh} is calculated. Current-voltage and power-voltage characteristics generated for every combination of the five parameters, $R_s, R_{sh}, I_{ph}, I_{sat}$, and n, thus calculated, is produced, and the combination of parameters that produced the least error between the modeled and experimental power is extracted as the optimal parameter set. Weixiang *et al,* adopted a double-diode model to arrive at a mathematical model comprising of analytical expressions for all the other parameters while reasonably ignoring the shunt resistance [33].

2.11 Numerical or iterative approach

The approximation and simplification used in the analytical approach may result in errors as one chooses to ignore the effort of either single or multiple parameters. Numerical approaches, on the other hand, use complex mathematical tools for the analysis and give superior accuracy as compared to analytical approaches. Researchers have suggested numerous approaches of finding analytical solutions in terms of parameter estimation of photovoltaic modules. While it will be an extensive review work to go through all the available numerical approaches that researchers have followed, the review here will be limited to select literatures which in a broad sense, covers the essence of all of the approaches defined so far.

Kennerud suggest approximating five sets of equations, comprising of the five unknown parameters $R_s, R_{sh}, I_{ph}, I_{sat}$, and n, and solving them simultaneously for the solution [26]. Three of these equations were obtained by evaluating the single-diode equation at the open-circuit point (V_{oc}), the short-circuit point (I_{sc}), the maximum power point (V_{mp}, I_{mp}), while the remaining two equations were obtained by differentiating the single-diode equation at V_{oc} and (V_{mp}, I_{mp}). These five sets of equations with five unknown parameters were solved by the Newton-Raphson iterative approach to extract the five unknown parameters, $R_s, R_{sh}, I_{ph}, I_{sat}$, and n.

Charles *et al.* suggest deriving four sets of equations to solve for the four parameters R_s, R_{sh}, I_{ph}, and I_{sat}, using the experimental values of $V_{oc}, I_{sc}, V_{mp}, I_{mp}, R_{so}$ and, R_{sho}, of the two cells differing in size [31]. For the given set of values of ideality factor, n, these four equations are solved numerically and those set of five parameters that produced the least deviation from the experimental and calculated currents is chosen. Additionally, with the knowledge of the four parameters, a modified form of the single-diode equation at the maximum power point, is solved using the Newton-Raphson method to find the optimal value of the ideality factor, n.

Chan *et al.*, present an analytical method, using the Newton-Raphson method, to estimate the parameter using significant data points on the I-V curve of a commercial photovoltaic solar module and the slope of the current-voltage characteristic at the open-circuit and the short-circuit point [27]. Similarly, the numerical approach involves a complex algorithm which uses all points in the current-voltage characteristics to provide for more accurate model parameters. This approach, however, requires

extensive computational effort and the accuracy of the extracted parameters are highly influenced by the initial values selected for the extracted parameters [29]. Studies suggest that the convergence of such an algorithm depends on the accurate selection of the initial guess values [34].

Manning *et al.* proposes using a heuristic approach for parameter estimation followed by the application of a Newton-Raphson method for the solution of the implicit nonlinear double-diode equation [21]. The authors suggest that the model could be used for circuit based simulation platform, available such as SABER and SPICE. For actual modeling, using the Levenberg Marquardt approach, they proposed to estimate the five parameters $R_s, R_{sh}, I_{ph}, I_{sat1}$, and I_{sat2}, while keeping the ideality factor, n, at a constant value of 2 for the double-diode model. They define a set of five equations representing approximation of $R_s, R_{sh}, I_{ph}, I_{sat1}$, and I_{sat2}, to serve as initial values for the parameters for the Levenberg-Marquardt approach and another set of five equations to iteratively find the optimal parameter based on curve fitting with experimental current-voltage data points data. Although the authors were able to predict parameters with acceptable accuracy for the fit, this approach required the definition of 10 sets of independent equations just for the parameters. The heuristic approach made is computationally complex when the initial values assigned were not a close guess of the parameters.

Al Qahtani suggest, using the MATLAB® built-in function, *fsolve*, for the simultaneous solution of system of non-linear equations to extract the five parameters [35]. The three sets of equations are derived by evaluating the single-diode equation at three significant points, i.e., the open-circuit voltage, the short-circuit current, and the maximum power point. For the remaining two equations, the author suggests

using the derivation of power with respect to current and voltage at the maximum power-point and equating each to zero. The author claims using the derivative of power, as opposed to the common technique of using the derivative of current with respective to voltage at the open-circuit voltage point and equating to negative reciprocal of the shunt resistance, R_{sh}, results in a less complex calculation, less iterations, and less model adjustments for the estimation of the parameters.

El Tayyan, suggests using Lambert W function to derive an explicit analytical expression for the current and voltage using the single-diode equation [36]. The analytical expressions were evaluated with experimental values of $V_{oc}, I_{sc}, V_{mp}, I_{mp}$ etc., to arrive at three analytical expressions. Furthermore, differentiating power with respect to voltage and current and equating to zero produced the remaining two expressions. The author suggests extracting the five parameters, $R_s, R_{sh}, I_{ph}, I_{sat}$, and n, of the single-diode equation by simultaneously solving these five equations. To make the simultaneous solution more manageable, the author suggests solving any four subsets of the five equations, while increasing the value of one of the parameters, I_{ph}, in steps. Parameters set, which produce the least- root measured squared error (RMSE), are used as the extracted parameters, and the results showed a higher degree of agreement with values expressed in other literature. The modeling was implemented in the MAPLE software using one of the in-built function, "*fsolve*", for simultaneous solution of (any) four equations.

Azab suggest using an evolutionary computational approach, such as particle swarm optimization (PSO) followed by a least-squares curve fitting algorithm based on knowledge of three significant points, namely, the open-circuit voltage, the short-circuit current, and the maximum power point, to extract the

parameters of a single diode equation [37]. The author defines an objective function, comprising of the nameplate data of V_{oc}, I_{sc}, V_{mp} and I_{mp} of the photovoltaic solar module and used PSO technique to find optimal values for the model parameters. Particle swarm optimization uses the social interaction of particles, which represent the vector of the parameters to be identified, within a defined search-space, wherein the individual particle's position and velocity is updated with every iteration, followed by an evaluation of the objective function. In order to increase the accuracy, the extracted parameters were fed to the least-squares curve fitting algorithm to produce a final optimal set of the parameters. This was implemented using a specific function in the optimization toolbox of MATLAB®.

Additionally, several meta-heuristic based optimization techniques have also been employed for parameter extraction corresponding to photovoltaic solar devices. As opposed to the aforementioned general analytical and numerical approaches, heuristic based optimizations use complex evolutionary algorithms for curve fitting of the entire current-voltage characteristics corresponding to a given photovoltaic device, resulting in parameter extraction with improved accuracy. In this regard, El Naggar *et al.* suggest using an algorithm based on simulated annealing which emulate the physical cooling process (annealing) to produce high quality crystals, resulting from a state with the minimum energy [38]. Hamid *et al.* use algorithms based on particle-swarm, which as mentioned earlier, is based on social interaction of solutions represented by a set of particles that swim through a multi-dimensional space with the velocity updated iteratively [39]. Wei *et al.* also suggest using chaos particle swarm optimization, which is a modified form of particle swarm optimization [40]. Bouzidi *et al.* suggest representing the output voltage

as function of the current and determining resulting factors of such a function that provide for the determination of the parameters [41]. Similarly, Al Rashidi *et al.* have used optimization based on pattern search [42, 43] and Askarzadeh *et al.* suggest using optimization based on artificial-bee swarm [44]. In general, these optimization algorithms have been developed based on observations of some form of behavior (physical or social) of processes and entities.

Chapter 3 : Methodology

3.1 Overview

The performance of a given photovoltaic device, i.e., a photovoltaic solar cell or module, may be characterized in terms of its current-voltage characteristic. This characteristic defines the current delivered by the device as a function of the applied voltage across its terminals. Following fabrication, the current-voltage characteristic of the photovoltaic device in question is often acquired under standard testing conditions, i.e., a specific set of conditions pertaining to the intensity and spectral distribution of the incident radiant energy and the device temperature. This measurement is performed within the framework of the guidelines defined by the relevant national and international photovoltaic device standards [45, 46]. The testing of photovoltaic devices is aimed at achieving a measure of quality-control, i.e., rejecting the devices that do not meet the required minimum performance standard, and, for the devices that are deemed to be acceptable, classifying such devices in terms of their device performance. From the measured current-voltage characteristics, three device performance metrics are often employed in order to characterize the performance of such a photovoltaic device: (1) the open-circuit voltage, V_{oc}, (2) the short-circuit current, I_{sc}, and (3) the maximum power point, (I_{mp}, V_{mp}), corresponding to the point on the current-voltage characteristic where the delivered power achieves a maximum. Any deviation in these parameters from the "norm", as defined by the particular manufacturing process being considered, may arise owing to variations in the preparation conditions and the materials employed. Photovoltaic devices that are deemed to have a performance that is deemed insufficient can be rejected

prior to shipping. This testing and evaluation process, which is employed in order to guarantee the quality of the shipped products, is detailed by the International Electrotechnical Commission (IEC) [47, 48].

The focus of this chapter is twofold. First, the methodology associated with measurement of the current-voltage characteristic of a typical photovoltaic device is presented. Second, means whereby model parameters may be extracted from such a measured current-voltage characteristic based on a proposed optimization algorithm is featured. Towards this requirement, I begin by presenting the current-voltage characteristic of a typical photovoltaic device and figures of merit associated with it which are used in order to characterize the device. Following this, means, whereby measurements of the current-voltage characteristics of a given photovoltaic devices are performed under standard testing conditions using a solar simulator, are presented. For the realization of the second goal of this chapter, the empirical models, used to describe the current-voltage characteristic of a typical photovoltaic device, are presented in detail. The discussion on photovoltaic device behavior is cast within the framework of the equivalent circuit models that were introduced in Chapter 2 and highlights the model parameters of interest for the purposes of this particular study. A study of the sensitivity of the current-voltage characteristics, with respect to the model parameters, is then pursued in order to further understand the impact of each model parameters on the corresponding current-voltage characteristic; this is in anticipation that such knowledge may be utilized during the course of the model parameter extraction based on the proposed optimization algorithm. Finally, the task of model parameter extraction, from the measured current-

voltage characteristic, is formulated as a non-linear least-squares fitting problem and trust region based optimization algorithm.

The chapter is organized in the following manner. Section 3.2 discusses how current-voltage characteristic measurements are performed and highlights the principles and processes involved in the measurement of the current-voltage characteristics of photovoltaic devices, in particular, for the case of solar modules. In Section 3.3, empirical models, associated with photovoltaic device current-voltage characteristics, are presented. Section 3.4 discusses the model parameters of interest based on the discussed empirical models, and the sensitivity of the current-voltage characteristics with respect to such modeling parameters is explored. Sections 3.5 and 3.6 detail the task of model parameter estimation based on the current-voltage characteristic of a typical photovoltaic device; I formulate the approach as a non-linear least-squares optimization problem and the application of a proposed trust region optimization algorithm for such model parameter extraction from the measured current-voltage characteristic is pursued.

3.2 Current-voltage characteristic measurement

Measurement of the current-voltage characteristic is one of the most fundamental characterization techniques used for photovoltaic devices. In a manufacturing environment, this serves as a verification step for the quality of photovoltaic devices and will allow for a sorting out of the finished product, i.e., photovoltaic solar cell or module, according to its power and efficiency. The solar simulator, often referred to as a flash-tester, is used in order to characterize the photovoltaic device performance

based on well-established standards that define the measurement components and processes. These standards, designed by standardization bodies, such as International Electrotechnical Commission, provide guidelines that regulate different aspects of photovoltaic energy systems, ranging from device production, testing, and measurement.

In order to ensure measurement uniformity, a given photovoltaic device performance is measured under standard test conditions or standard rating conditions. The standard testing conditions correspond to an irradiance level of 1000 $W \cdot m^{-2}$ of AM1.5 solar spectrum, the photovoltaic solar cell temperature being set to 25°C [49]. The solar simulator comprises of an artificial light source that can generate illumination closely approximating natural sunlight, along with the required optics and filters used to modify the output spectrum of the light source to fit the classification requirement for the test involved, such as AM0 and AM1.5, and the associated power supply. The photovoltaic device post production is tested using the solar simulator, wherein the device is exposed to a flash of light from the light source in the solar simulator. Its response, in terms of the voltage and current, is then measured in order to obtain the current-voltage characteristic for the device under test. For the purposes of this thesis, the current-voltage characteristics of representative mono-crystalline and poly-crystalline silicon solar modules were measured and recorded. These measurements were performed in the solar module manufacturing plant of our industrial partner using Endeas' QuickSun® (AAA) solar simulator. Figure 3.1 illustrates the measurement principle of a typical pulsed solar simulator (flash tester).

The working of a pulsed light solar simulator, used for measurements of the current-voltage

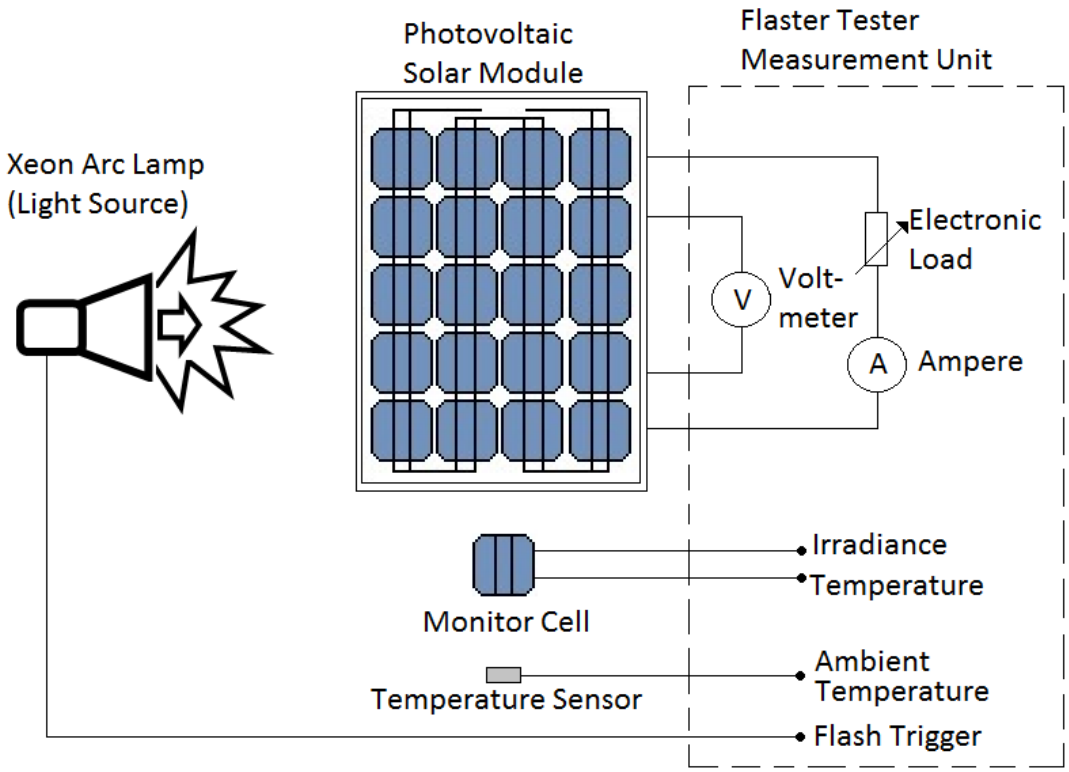

Figure 3.1: Four wire measurement setup for current-voltage measurements using a flash-tester. This figure is adopted from [50]. The online version of this figure is in color.

characteristics, is explained as follows [50]; when the flash is triggered, the irradiance level is measured within a monitor cell. The pulse reaches its peak and then gradually decays. The measurement is typically started at an irradiance level a little over 1000 $W \cdot m^{-2}$ so that for the following short duration of the measurement time, all current-voltage measurements being taken around an irradiance level of 1000 $W \cdot m^{-2}$. Each measurement point is then corrected or transposed to the required irradiance level of 1000 $W \cdot m^{-2}$. In this case, when the target irradiance, which is typically at 1150 $W \cdot m^{-2}$ for the onset of the current-voltage measurement is reached, the photovoltaic module is swept from the short-circuit condition to the open-circuit condition, and the voltage, current, and irradiance signals are recorded for approximately 2 ms of measurement time.

As illustrated in Figure 3.1, the QuickSun® solar simulator (flash-tester) uses a four-wire measurement in order to minimize the influence of the probe contact resistance. When measuring the current-voltage characteristics of a crystalline silicon based photovoltaic module, the contact pins of the measurement units are connected directly to the ribbons on the rear side of the module, which are housed in a protective box, referred to as a junction box. The resistive loss, caused by current flow through the ribbons, will influence the measured fill-factor, which is closer to the actual operating conditions of the photovoltaic solar cell in a photovoltaic system. Once the contact pins are in contact with the ribbon, a flash is triggered, and the operating current and voltage of the device can be obtained by changing an electronic load resistance, which is swept from short-circuit to open-circuit.

The measurement time depends on the measurement device electronics, and can vary from 2 to 30 ms, depending on the manufacturer. The measurement electronics of the QuickSun® (AAA) solar simulator, measured at 4096 individual data points of voltage, current, and irradiance signal, within the 2 ms interval. These data points are then averaged in groups of eight in order to obtain 512 current-voltage data points. The averaged measured data is then corrected for temperature and irradiance conditions as per the IEC 60891 standard, which is a standard published by the IEC that defines the procedures for temperature and irradiance corrections to the measured current-voltage characteristics of crystalline silicon photovoltaic devices. This standard basically defines the procedure to mathematically transpose the current-voltage characteristics measured at one irradiance and temperature level to different irradiance and temperature levels. Figure 3.2 illustrates the snapshot of the irradiance trace, which illustrates the onset of measurements of the voltage, current, and irradiance signals near the required level and continues for approximately 2 ms. Additionally, Figure 3.3 shows the user interface of Endeas' QuickSun® measurement systems used to perform the I-V measurement. Figure 3.4 shows the actual test apparatus, Endeas' QuickSun® Class AAA solar simulator (flaster tester), used for the current–voltage measurements.

3.3 Empirical model of photovoltaic device

The current-voltage characteristic of a photovoltaic device is modeled based on the underlying physics of the charge-carrier generation within the semiconductor material as a consequence of the absorption of solar energy. For modeling purposes, a photovoltaic device will be considered in its

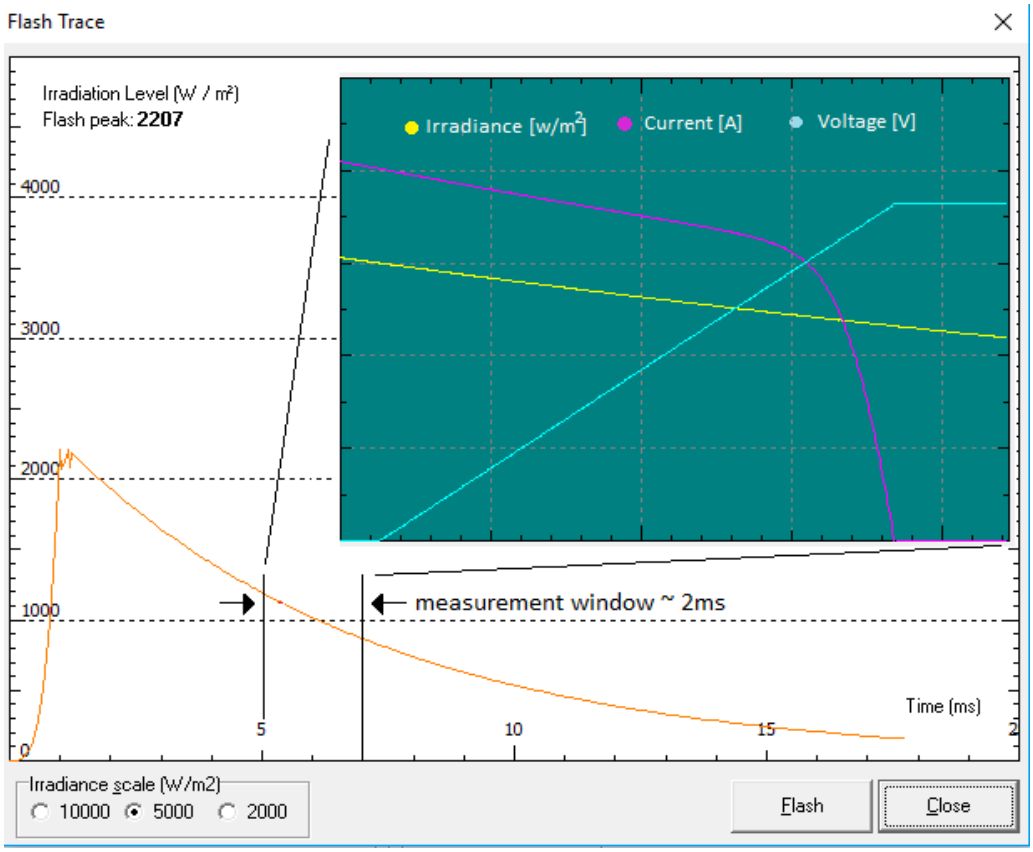

Figure 3.2: Modified snapshot of the flash trace of a typical trigger of flash in QuickSun® solar simulator.

The online version of this figure is in color.

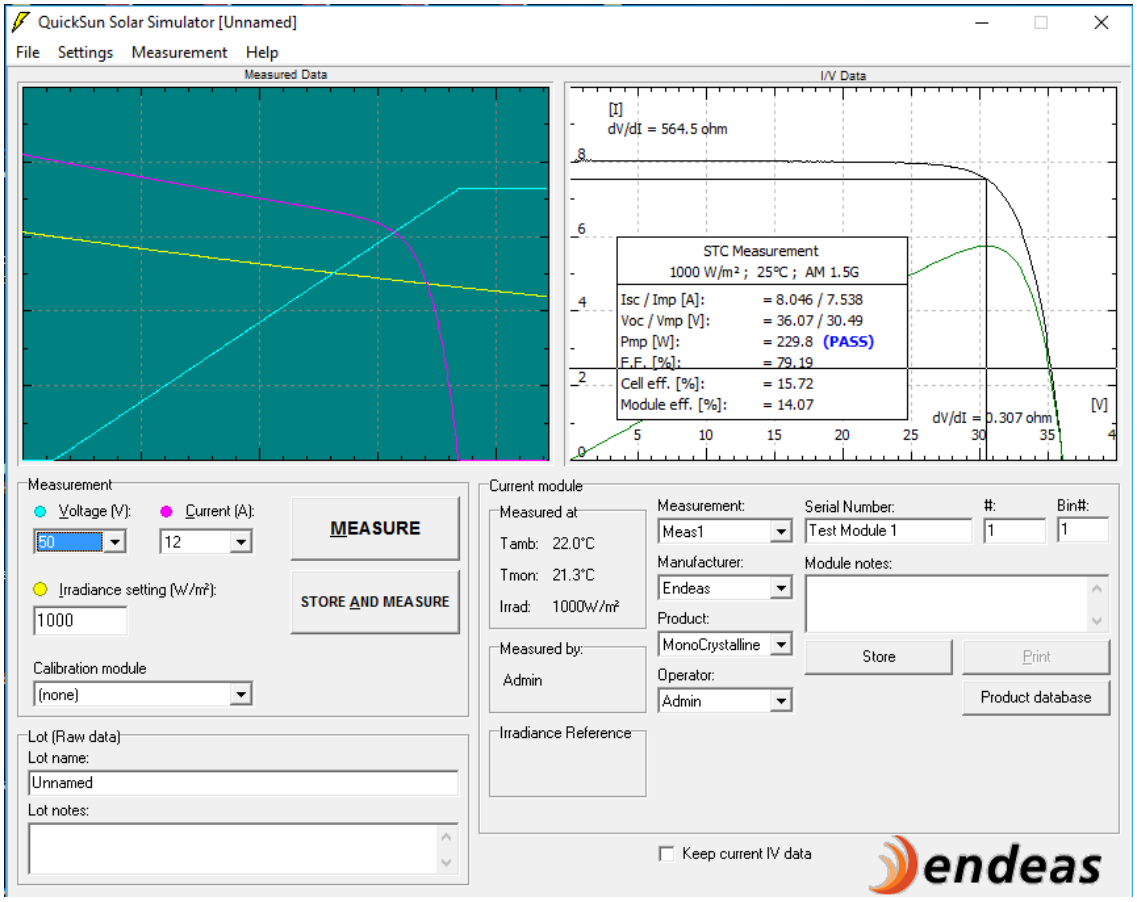

Figure 3.3: User interface of the measurement system of the QuickSun® solar simulator. The online version of this figure is in color.

Figure 3.4: The Endeas Flash tester (Class AAA solar simulator) used for measuring the current-voltage characteristics of a solar module on the premises of our industrial partner. The online version of this figure is in color.

elemental form, i.e., a photovoltaic solar cell, and then expand the model to cover solar modules. Essentially, a photovoltaic solar cell is a large area p-n junction, formed by interfacing two dissimilarly doped layers of semiconductor materials, i.e., n-type and p-type. The high density of charged carriers, i.e., electrons on the n-side of the junction and holes on the p-side of the junction, create a potential difference across the p-n junction. Exposing such a p-n junction to solar radiation results in the generation of excess electron-hole pairs, i.e., excess charge carriers (electron and holes), in response to the absorption of incident photons from the sunlight by the atoms within the semiconductor crystal. These light generated electron-hole pairs are separated under the action of the developed built-in potential (and the associated electric field) across the junction. These excess charge carriers drift under the action of this electric field, and are ultimately collected by the contacts, which interface the interior of the device with the peripheral circuitry.

3.3.1 Ideal Model

Ideally, an illuminated photovoltaic solar cell can be represented by an equivalent electrical circuit, as depicted in Figure 3.5 [32]. In this circuit model, the photovoltaic solar cell is viewed as being comprised of a constant-current source operating in parallel with a p-n junction diode. Here, the constant current source models the charge carrier generation mechanism while the diode models the separation of such charge carriers under the influence of the built-in electric field. Kirchhoff's current law suggests that the output current, *I*, of the equivalent circuit may be expressed as

$$I = I_{ph} - I_d, \qquad \text{..... (3.1)}$$

where I_{ph} and I_d are the photo-generated and diode current of the illuminated photovoltaic solar cell, respectively. The photo-generated current, I_{ph}, is proportional to the intensity of the solar irradiance and the diode current, I_d, is given by the Shockley equation [51], i.e.,

$$I_d = I_{sat}\left[exp\left(\frac{qV}{nk_BT}\right) - 1\right], \quad \text{..... (3.2)}$$

where

- I_{sat} : is the diode reverse saturation current, representing the diffusion mechanism,
- n: is the diode ideality factor,
- k_B: is Boltzmann's constant,
- T : is the temperature for the p-n junction, and
- q : it the fundamental charge of the electron.

Substituting Eq. (3.2) into Eq. (3.1), the output current of an ideal photovoltaic solar cell, I, may be expressed as

$$I = I_{ph} - I_{sat}\ \left(exp\left(\frac{qV}{nk_BT}\right) - 1\right). \quad \text{..... (3.3)}$$

The thermal voltage, V_t, is a term that is often employed in the analysis of the performance of a photovoltaic solar cell. The thermal voltage is given by,

$$V_t = \frac{k_BT}{q}, \quad \text{..... (3.4)}$$

Table 3.1 : The values for the fundamental constants introduced in Eq.(3.2)

Parameters	Values [unit]
k_B	1.38 x 10^{-23} [J·s]
q	1.9 x 10^{-19} [C]

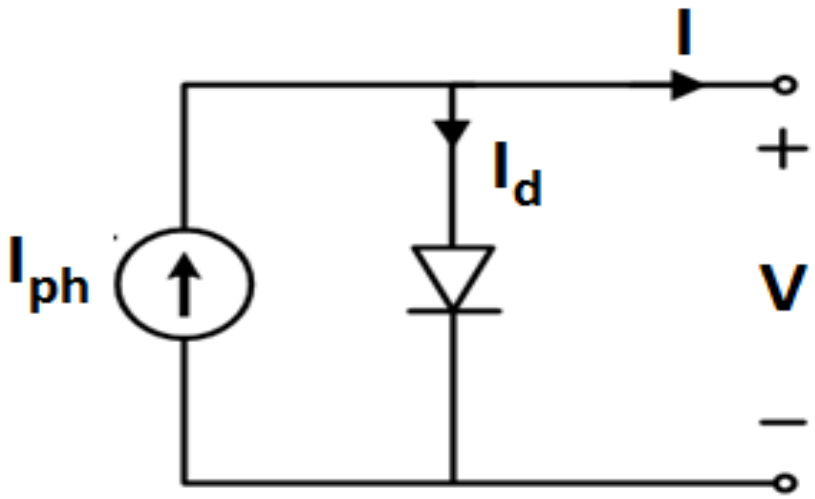

Figure 3.5: The equivalent electrical circuit model representing the behavior of an ideal photovoltaic solar cell. This model is in the single-diode form; the parasitic resistances associated with the typical single-diode are not present.

where the terms k_B and q in Eq (3.4) are as previously defined and T represents the device temperature. Table 3.1 provides standard values for the constants introduced in Eq. (3.2).

3.3.2 Single-diode equivalent model

Photovoltaic solar cells, in practice, however, exhibit a number of non-idealities on account of the inherent parasitic resistances that are present within such a cell [52]. In order to account for the power losses that occur within such cells due to such parasitic resistances, an equivalent circuit model, which is a generalization of that depicted in Figure 3.5, is presented in Figure 3.6. This circuit model is termed the single-diode equivalent model, as only one-diode is included [27]. Like the ideal case, the single-diode equivalent circuit of a photovoltaic solar cell consists of a constant current source in parallel with a single p-n junction diode. In this case, however, series and shunt (or parallel) parasitic resistances are included in order to account for the non-idealities that are present [26, 32]. In the equivalent circuit of the single-diode model, the constant current source, I_{ph}, represents the photo-generated current and the current through the single diode, I_d, represents the diffusion within the p-n junction. The series resistance is mainly due to the contact resistance on the front and back surfaces between the interface of the metal and the semiconductor layers and the ohmic resistances of the n and p diffused layers within the photovoltaic solar cell itself [53]. Power losses due to series resistances are dissipated in the form of thermal energy. Shunt resistances, on the other hand, arise from defects within the semiconductor that provide alternative paths for leakage currents, resulting in power losses, especially due to leakage currents along the edges of the photovoltaic solar cell [53].

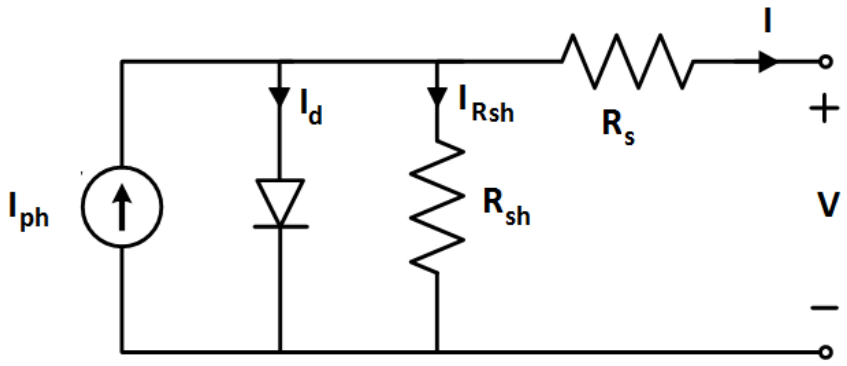

Figure 3.6: The single-diode photovoltaic equivalent electrical circuit model of a photovoltaic solar cell including the parasitic resistances.

The output current of the photovoltaic cell, I, can be represented in terms of the photo-generated current, I_{ph}, the current through the diode, I_d, and the leakage current through the shunt resistance, I_{Rsh}, , i.e.,

$$I = I_{ph} - I_d - I_{Rsh}, \quad \text{..... (3.5)}$$

where, in addition to $I_{ph}$and I_d, the leakage current, I_{Rsh},

$$I_{Rsh} = \frac{V+IR_s}{R_{sh}}, \quad \text{..... (3.6)}$$

is added, where R_s is the series resistance and R_{sh} is the shunt resistance. Hence, the output current, I, of the photovoltaic cell, as suggested by the equivalent circuit single-diode model, may be expressed as,

$$I = I_{ph} - I_{sat}\left(exp\left(\frac{q(V+IR_s)}{nk_BT}\right) - 1\right) - \frac{(V+IR_s)}{R_{sh}}. \quad \text{..... (3.7)}$$

3.3.3 Double-diode equivalent model

In the single-diode model, the recombination of charge carriers in the space-charge region is neglected. If greater accuracy is required, more complex models, incorporating additional diodes, representing the recombination of charge carriers in the space-charge region, have been suggested [27,33, 54,55]. The first-order variant of this model is referred to as the double-diode circuit model, and is presented in Figure 3.7. The double-diode circuit model of a photovoltaic solar cell is comprised of a constant-current source in parallel with two diodes, one diode accounting for the current due to charge carrier diffusion, the other accounting for recombination processes within the space-charge region;

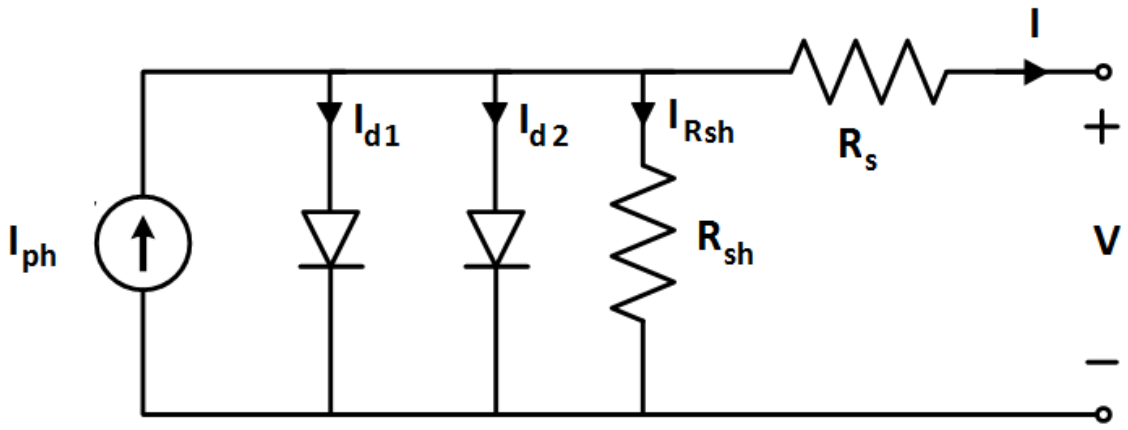

Figure 3.7: The double-diode photovoltaic equivalent electrical circuit model of a photovoltaic solar cell including the parasitic resistances.

parasitic resistances are also included. Hence, the output current, I, of the photovoltaic cell, based on the double-diode circuit model, comprised with an additional diode, is given by Eq. (3.8) as,

$$I = I_{ph} - I_{d1} - I_{d2} - I_{Rsh}. \quad \text{…….. (3.8)}$$

The two diode currents, $I_{d1}$and I_{d2}, are as given by the Shockley equation for each diode [51], where

$$I_{d1} = I_{sat1}(exp\left(\frac{q(V+IR_s)}{n_1 k_B T}\right) - 1), \quad \text{…….. (3.9)}$$

and

$$I_{d2} = I_{sat2}(exp\left(\frac{q(V+IR_s)}{n_2 k_B T}\right) - 1), \quad \text{…….. (3.10)}$$

where

- I_{sat1}: is the diode reverse saturation current used to represent the diffusion mechanism
- I_{sat2}: is the diode reverse saturation current used to represent the recombination mechanism

The ideality factor, n_1, corresponding to the first diode accounts for the diffusion current, while the second ideality factor, n_2, corresponding to the second diode, accounts for the recombination current. The diode ideality factors, n_1 and n_2, may be approximated as being numerically equal to 1 and 2, respectively [51]. Placing Eqs. (3.9) and (3.10) into Eq. (3.8), the corresponding output current, I, of the photovoltaic cell, based on the double-diode equivalent circuit model, is seen to yield,

$$I = I_{ph} - I_{sat1}\left(exp\left(\frac{q(V+IR_s)}{n_1 k_B T}\right) - 1\right) - I_{sat2}\left(exp\left(\frac{q(V+IR_s)}{n_2 k_B T}\right) - 1\right) - \frac{(V+IR_s)}{R_{sh}}. \quad \text{..... (3.11)}$$

Although, the double-diode equivalent circuit model is considered to offer superior accuracy, the single-diode equivalent circuit model is found to adequately fit the current-voltage characteristics while offering less computational complexity with respect to the required parameterization, and is thus, the widely adopted model for photovoltaic solar cell (or module) performance [35, 55–57]. Therefore, for the purposes of this thesis, the single-diode equivalent circuit model for the photovoltaic solar cell is adopted. For commercial purposes, photovoltaic solar cells seldom are used individually but instead are grouped together to form solar modules, in appropriate series and parallel configurations. Therefore, the model equations (single or double diode model) are modified to describe the characteristics of these generalized forms of device. This modification is discussed in the following section.

3.3.4 Cell to module characteristics change

An individual crystalline silicon based photovoltaic solar cell typically generates a voltage of just under 0.6 V at 25°C when subjected to 1000 Watts per meter squared of incident solar radiation. In order to generate higher voltages and current levels for commercial applications, such cells are connected in series and/or parallel configurations, and are encapsulated with an environmentally protective laminate, thus forming a photovoltaic module. A number of such photovoltaic modules, connected together in series and/or parallel configurations form a complete power generation unit, referred to as a photovoltaic array, that will produce commercial or utility scale currents and voltages. This is illustrated in Figure 3.8.

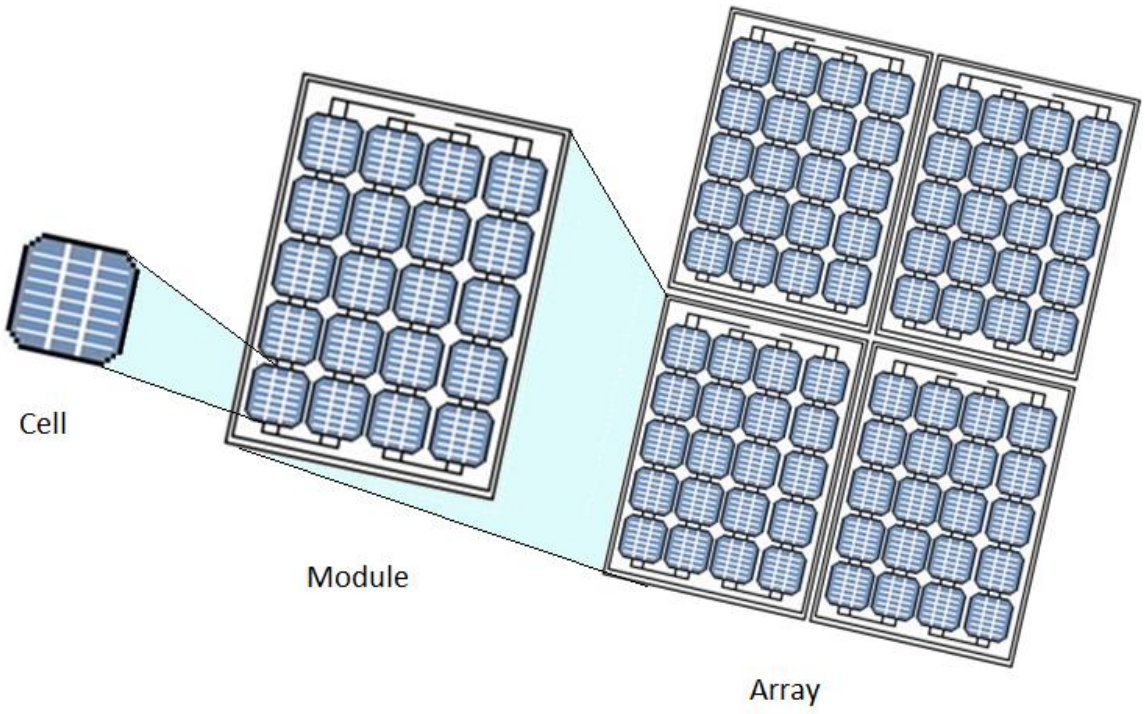

Figure 3.8: Illustration of a photovoltaic solar cell, a module, and an array. The online version of the figure is in color.

To attain higher voltages, photovoltaic modules are connected in series, and for the requirement of a higher level of current, the photovoltaic modules are connected in parallel. To be able to extract model parameters corresponding to an individual photovoltaic solar cell, module, or array, a generalization of the single-diode equation for photovoltaic solar cells connected in series, as was suggested by Tian *et al.*, will be employed [58]. For a photovoltaic module, comprised of N_s cells connected in series, the model equation, based on the single-diode expression, may be expressed as

$$I = I_{ph} - I_{sat}\left(exp\left(\frac{q(V+IN_sR_{s1})}{nN_sk_BT}\right)-1\right)-\frac{(V+IN_sR_{s1})}{N_sR_{sh1}}. \quad \text{..... (3.12)}$$

where I and V are the output current and voltage of the photovoltaic module, respectively, and the five model parameters are as defined earlier. Figure 3.10 illustrates the modified single-diode equivalent strings connected in parallel required to build a large module (or array). In this case, the model equation based circuit is for the case of a series connection of N_s photovoltaic solar cell to form a photovoltaic solar module. This model can be further adjusted, for the case of N_s cells (or modules) connected in series on a string, and N_p such identical units on the single-diode expression, which may be cast as [58],

$$I = N_pI_{ph} - N_pI_{sat}\left(exp\left(\frac{q(V+\frac{N_s}{N_p}IR_{s1})}{n_1N_sk_BT}\right)-1\right)-\frac{\left(V+\frac{N_s}{N_p}IR_{s1}\right)}{\frac{N_s}{N_p}R_{sh1}}, \quad \text{..... (3.13)}$$

where I and V are the output current and voltage of the photovoltaic module (or array), respectively.

3.4 Model parameters

The empirical model of a photovoltaic device in its elementary form, suggested by Eq. (3.7), or its generalization given by Eq. (3.15), is comprised of five model parameters (coefficients), which collectively define the current-voltage characteristic. As indicated earlier, these model parameters include the shunt resistance, the series resistance, the diode saturation current, the diode ideality factor, and the photo-generated current corresponding to a single-diode model. With the knowledge of these parameters, the behavior of the photovoltaic device can be simulated for a variety of different operating conditions. Prior to the extraction of model parameters corresponding to the current-voltage characteristics of a given photovoltaic device, it is instructive to examine the sensitivity of the current- voltage characteristic of a photovoltaic solar cell (or module) with respect to each of the model parameters. In this regard, the analysis of the sensitivity of a given current-voltage characteristic with respect to these model parameters is expected to help develop a strong intuition about how the computational approach adopted will fare during its implementation. The sensitivity will be examined through means of a nominal synthetic parameter set assumed for a photovoltaic solar cell. The current-voltage characteristic is studied through the selection of the aforementioned five model parameters. The influences of these parameters are studied individually by examining the effects on the current-voltage characteristics through variations of one model parameter of interest while holding the remaining model parameters constant. It is worth mentioning that the accuracy of the magnitude of the parameters considered here may be overlooked since the intent here is to understand the degree of influence of the respective parameters on the current-

voltage characteristics. Hence, nominal values corresponding to a typical photovoltaic device, i.e., a photovoltaic solar cell, have been used in this case. Ultimately, the extraction of model parameters, as is shown in the next chapter, from experimentally measured current-voltage characteristics curve, will be used.

3.4.1 Effect of series resistance

As is evident from the series of current-voltage characteristics generated for a wide variety of series resistance value, illustrated in Figure 3.9, an increase in the series resistance will affect the fill-factor of the photovoltaic cell. The open-circuit voltage and the short-circuit current are not influenced by the variation in series resistance, however. Power loses due to series resistance are the result of the limited conductivity of the metal contacts, the metal-semiconductor contact resistance, the substrate resistance, and the emitter sheet resistance [59]. Resistance to the flow of charge carriers, through the bulk of the semiconductor lattice is the predominant factor determining the series resistance. Besides this, the quality of the metallization also has a significant impact on the series resistance, and any physical damage to the metal contacts, such as broken fingers (metal electrodes), will further increase the series resistance, thereby causing power losses, and ultimately, leading to a reduction in the corresponding fill-factor.

3.4.2 Effect of shunt resistance

Ideally, the shunt resistance should be as high as possible. From the series of current-voltage characteristics generated over a wide variety of shunt resistance values, shown in Figure 3.10, it is

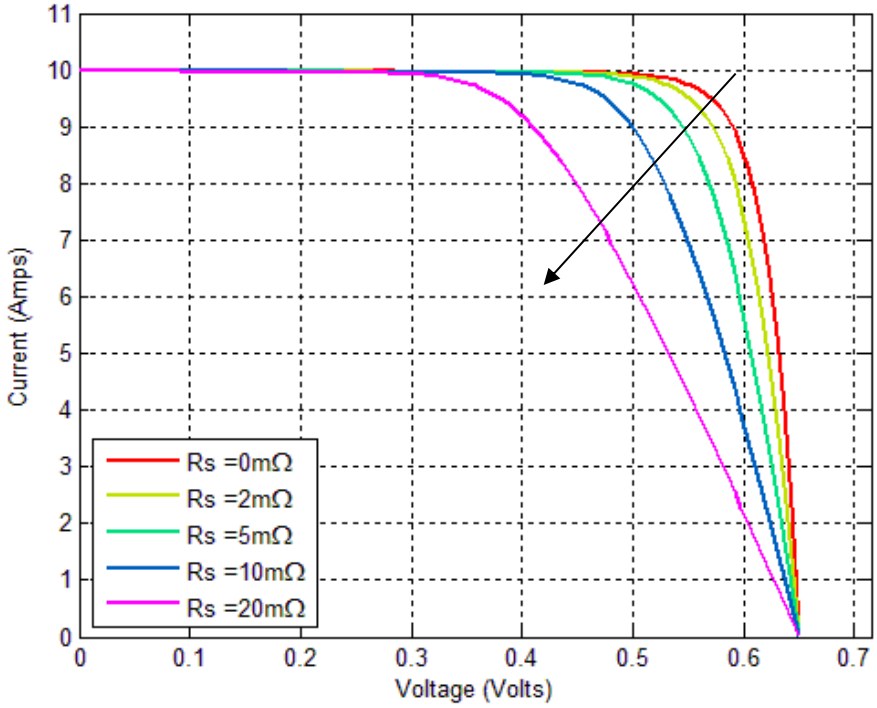

Figure 3.9: The sensitivity of the current-voltage characteristics to variations in the selection of series resistance, $\boldsymbol{R_s}$. All other parameters are set to their nominal values, i.e., $\boldsymbol{R_{sh}} = \boldsymbol{10\,\Omega}$, $\boldsymbol{n} = \boldsymbol{1}, \boldsymbol{I_{sat}} = \boldsymbol{1\times 10^{-10}}\ \boldsymbol{A}$, and $\boldsymbol{I_{ph}} = \boldsymbol{10\,A}$. The direction of the arrow indicates increase in the magnitude of respective model parameter of interest. The online version of this figure is in color.

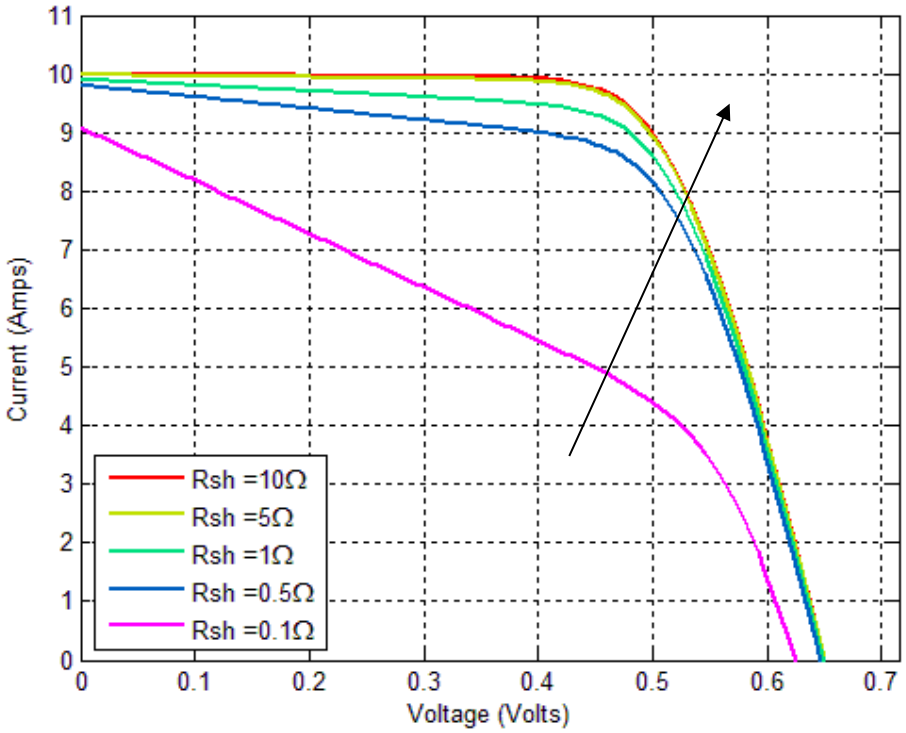

Figure 3.10: The sensitivity of the current-voltage characteristics dependence to variations in the selection of shunt resistance, $\boldsymbol{R_{sh}}$. All other parameters are set to their nominal values, i.e., $\boldsymbol{R_s = 3\,m\Omega}$, $\boldsymbol{n = 1}$, $\boldsymbol{I_{sat} = 1\times 10^{-10}\,A}$, and $\boldsymbol{I_{ph} = 10\,A}$. The direction of the arrow indicates increase in the magnitude of respective model parameter of interest. The online version of this figure is in color.

observed that a decrease in the shunt resistance reduces the fill-factor significantly. Significant reductions in the shunt resistance will decrease the short-circuit current and the open-circuit voltage of the photovoltaic solar cell. Shunt resistances of the photovoltaic solar cell originate from manufacturing defects, especially at the cell edges, which provide an alternative path for the current to flow, thereby decreasing the delivered power. Furthermore, defects, such as metal particles at the cell surface, cracks, and holes, etc., also reduces the current flowing through the junction.

3.4.3 Effect of photo-generated current

Based on the series of current-voltage characteristic curves shown in Figure 3.11, in response to the changes in the photo-generated current, I_{ph}, it can be said that the current-voltage characteristics of a photovoltaic solar cell are linearly proportional to the photo-generated current. Linear increases in the photo-generated current, I_{ph}, translate into increases in the intensity of the solar irradiance, which increases all factors, such as the fill-factor, the peak-power, the short-circuit current, and the open-circuit voltage. The change in short-circuit current is larger than that of the open-circuit voltage.

3.4.4 Effect of diode reverse saturation current

Figure 3.11 shows a series of current-voltage characteristics corresponding to changes in the reverse saturation current. Increases in the saturation currents result in a decrease in the peak power, the fill-factor, and the open-circuit voltage. Since the reverse saturation current and the diode ideality factors influence each other, it is difficult to analyze the change in the current-voltage characteristics based on the change in the reverse saturation current while the diode ideality factor is kept constant.

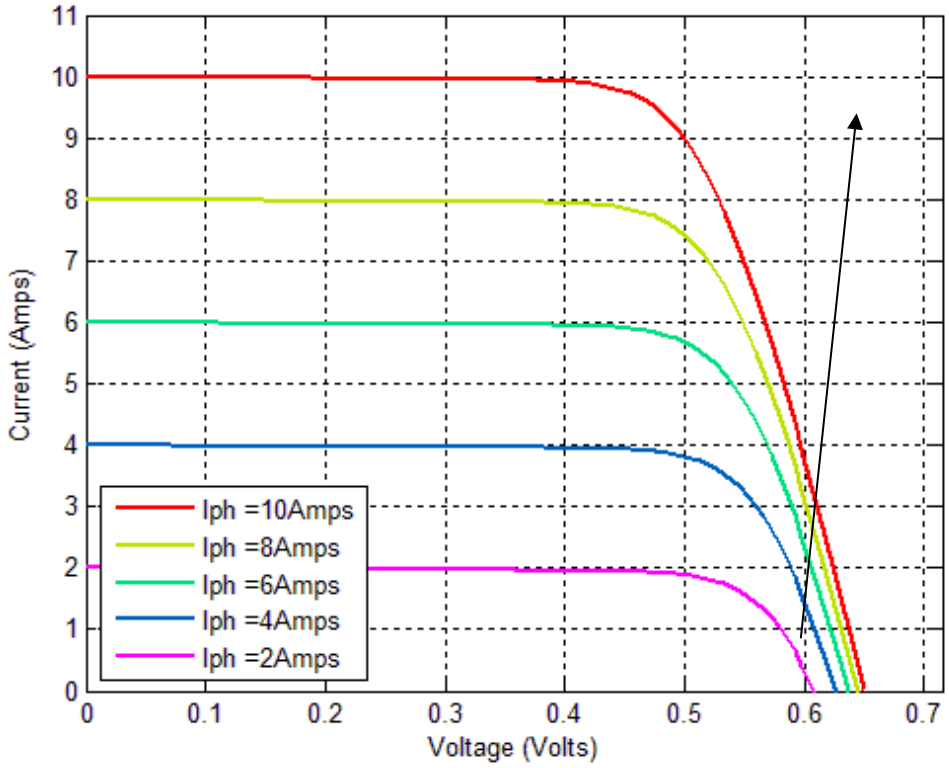

Figure 3.11: The sensitivity of the current-voltage characteristics to variations in the selection of the photo-generated current, $\boldsymbol{I_{ph}}$. All other parameters are set to their nominal values, i.e., $\boldsymbol{R_s = 3\ m\Omega}$, $\boldsymbol{R_{sh} = 10\ \Omega}$, $\boldsymbol{n = 1}$, and $\boldsymbol{I_{sat} = 1\times 10^{-10}\ A}$. The direction of the arrow indicates increase in the magnitude of respective model parameter of interest. The online version of this figure is in color.

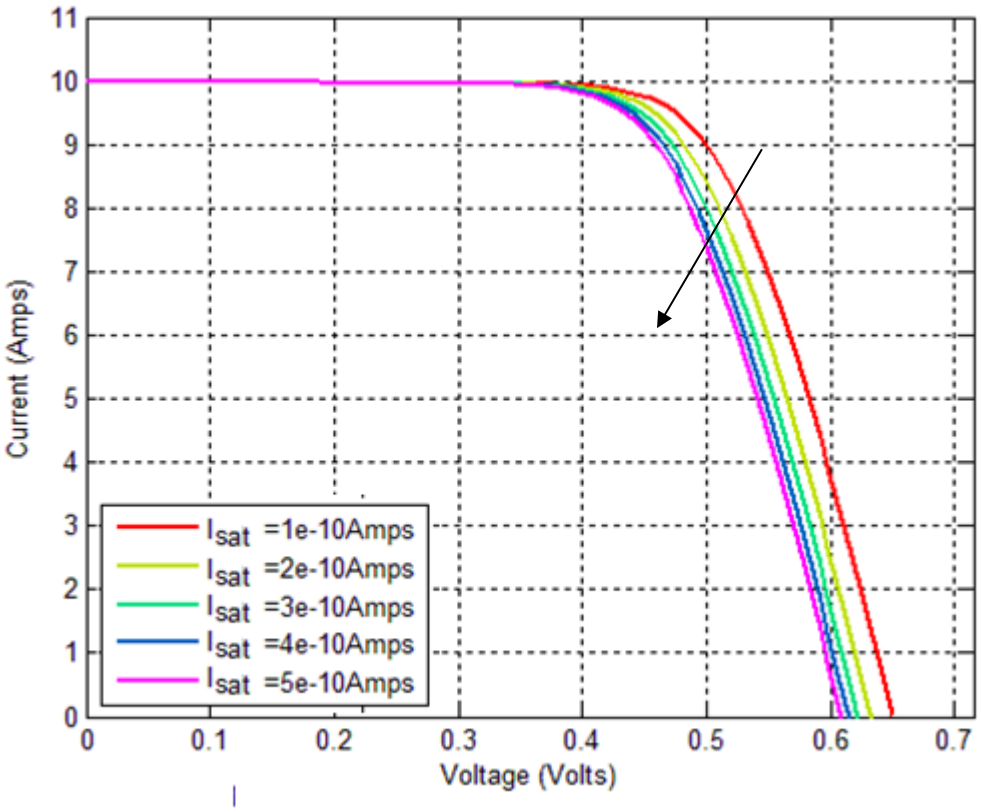

Figure 3.12: The sensitivity of the current-voltage characteristics to variations in the selection of reverse saturation current, $\boldsymbol{I_{sat}}$. All other parameters are set to their nominal values, i.e., $\boldsymbol{R_s = 3\,m\Omega}$, $\boldsymbol{R_{sh} = 10\,\Omega}$, $\boldsymbol{n = 1}$, and $\boldsymbol{I_{ph} = 10\,A}$. The direction of the arrow indicates increase in the magnitude of respective model parameter of interest. The online version of this figure is in color.

3.4.5 Effect of diode ideality factor

For understanding the influence of the diode ideality factor on the current-voltage (*I-V*) characteristics of a photovoltaic solar cell, the influence of changing the ideality factor on the other parameters has to be considered carefully. Figure 3.13 shows a series of the current-voltage characteristics corresponding to changes in the diode ideality factor, n. The series of the current-voltage characteristics appears to suggest that as the p-n junction's behavior moves away from the ideal diode behavior, indicated by the increase in the diode ideality factor, the peak power and the fill-factor increase with the diode ideality factor. This is because, in this case, the ideality factor is changed while keeping all other parameters, including, especially the reverse saturation current, constant. However, it should be noted that any changes in the diode ideality factor are bound to have an influence on the reverse saturation current. More specifically, an increase in the diode ideality factor is associated with increases in the reverse saturation current. Therefore, as the characteristic of the diode moves away from ideality, i.e., the ideality factor increases, the power and the fill-factor may be expected to decrease. Therefore, for this case, considering the variation of diode ideality factor and associated influence on the reverse saturation current, Figure 3.14 correctly represents the current-voltage characteristics.

3.5 Model Parameter Extraction

Depending on the adopted equivalent electrical model, either five or seven model parameters (unknowns) are required to be extracted. Since the model equations are non-linear transcendental equations, obtaining an exact solution on the basis of elementary algebraic manipulations is simply not

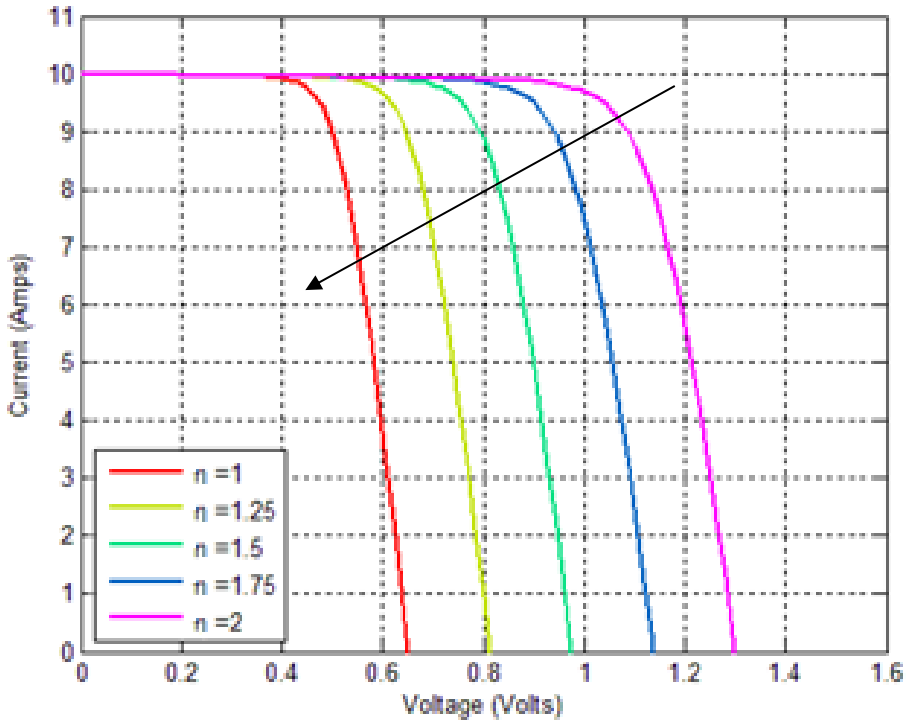

Figure 3.13: The sensitivity of the current-voltage characteristics to variations in the selection of ideality factor, $\boldsymbol{n}$. All other parameters are set to their nominal values, i.e., $\boldsymbol{R_s = 3\,m\Omega}$, $\boldsymbol{R_{sh} = 10\,\Omega}$, $\boldsymbol{I_{sat} = 1\times10^{-10}A}$, and $\boldsymbol{I_{ph} = 10\,A}$. The direction of the arrow indicates increase in the magnitude of respective model parameter of interest. The online version of this figure is in color.

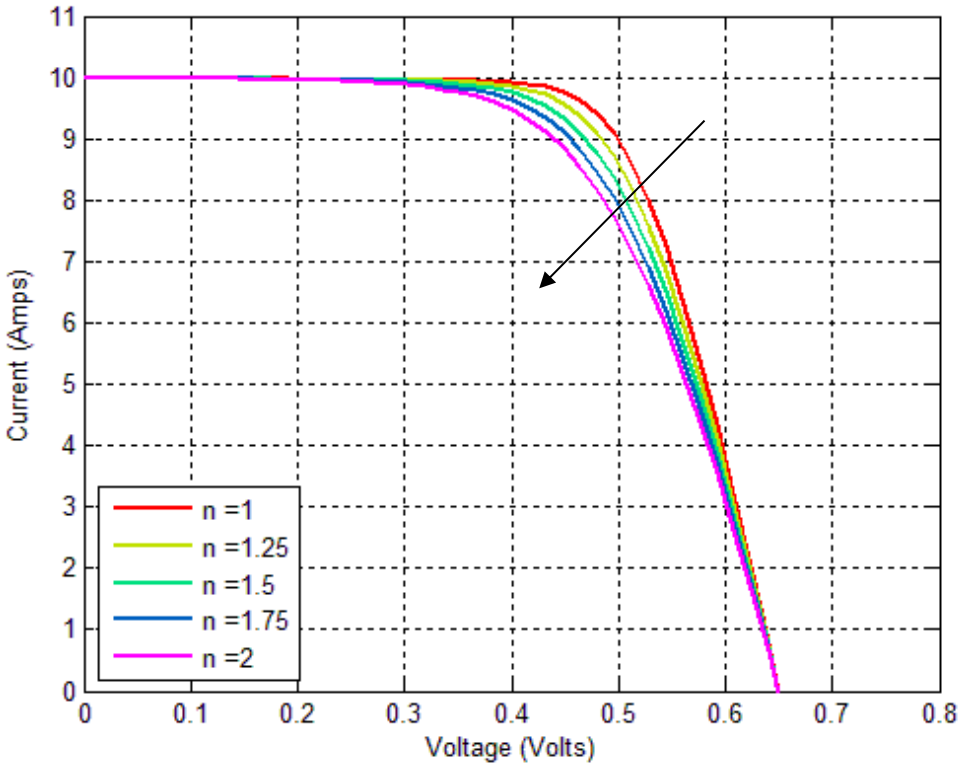

Figure 3.14: The sensitivity of the current-voltage characteristics to variation in the selection of ideality factor, $\boldsymbol{n}$, and the reverse saturation current, $\boldsymbol{I_{sat}}$. All other material parameters are set to their nominal values, i.e., $\boldsymbol{R_s = 3\ m\Omega}$, $\boldsymbol{R_{sh} = 10\ \Omega}$, and $\boldsymbol{I_{ph} = 10}$ A. The direction of the arrow indicates increase in the magnitude of the respective model parameters of interest. The online version of this figure is in color.

possible [26]. Analytical methods, based on certain approximations and subsequent simplifications to obtain the model parameters, have been adopted [32,60]. Owing to reduced complexity with acceptable accuracy, numerous researchers have used the single-diode equivalent model for the simulation of the photovoltaic device performance [32, 61, 62].

Towards more complex approaches, for better fits, complex mathematical tools, such as iterative or numerical analyze, may be used in order to extract the model parameters that had best be used [26, 63]. Furthermore, evolutionary optimization techniques, such as the genetic algorithm, particle swarm, etc., have also been proposed to extract parameter for better fits [29, 64]. The accuracy with which the model parameters will be extracted from the current-voltage characteristics is very important, especially for the purpose of device and materials characterization. Least-squares fitting of the experimental data, with the desired current-voltage model, is an obvious choice for such data fitting requirement. In this regards, to ensure an optimal fit, the specific case of trust-region optimization approach is explored to work out the computational scheme for model parameter extraction based on the least-squares fit of the measured current-voltage characteristics of a given photovoltaic device.

3.6 Least-squares optimization based on trust-region method

In most applications, complex system behavior is often described in terms of a model created via certain relationships such as

$$y = f(z; x_1, x_2, \dots, x_n), \quad \dots (3.14)$$

where f defines the model or relationship between the variables, $x_1, x_2, \ldots, x_n$ being the model parameters (also referred to as design variables), z is the control variable or input, and y is the expected response or output to z. Such a model often defines certain objective functions as a measure of the performance of the system that one wishes to optimize, which based on requirements, may either mean minimizing or maximizing the objective function, for example, maximizing the profit in business, minimizing the overall system energy function, etc. Thus, optimization is the minimization (or maximization) of an objective function subject to constraints (if applicable) on its model parameters and can be expressed as

$$\min_{\bar{x} \in R^n} f(z; \bar{x}), \ \ subject\ to \ \begin{cases} c_i(\bar{x}) = 0, i \ \in E \\ c_i(\bar{x}) \geq 0, i \ \in I \end{cases}, \qquad \ldots (3.15)$$

where $\bar{x}$ is the vector of model parameters or variables, $f(z; \bar{x})$ is the objective function in real coordinate space of n dimensions, i.e., $f: R^n \rightarrow R$, $c_i(\bar{x})$ is the constraints that the model parameters must satisfy, E is the set of equality constraints, and I is the set of inequality constraints. Such problems form the class of multivariate optimization problems which are very common in a variety of disciplines, such as economics, manufacturing, medicine, engineering, and science, etc.

A crucial step in optimization is to classify the optimization problems since algorithms used to solve such optimization problems are often designed to suit the particular type of problem at hand. Accordingly, depending on the nature of the objective functions and/or constraints functions, the optimization problems can be classified as being linear and non-linear, unconstrained and constrained, discrete and continuous, deterministic and stochastic optimization problems, etc. For our requirements

of parameter estimation of photovoltaic device, the associated model functions and constraints functions constitutes differentiable non-linear functions which can be appropriately bounded within certain constraints, and hence can be formulated as continuous non-linear optimization problems.

Before proceeding with the parameter estimation of a photovoltaic device, it is intuitive to formulate the optimization problem based on the mathematical model that represents the electrical characteristics of the photovoltaic device. For this requirement, the single diode equivalent model represented by Eq. (3.12) will be employed. As is evident from Eq. (3.7), or its generalized form Eq. (3.12), the defining equation of the model are implicit non-linear transcendental functions with the output current appearing on both sides of the equation. Hence, there is no explicit analytical solution for the output current. The parameter estimation problem can be formulated as a nonlinear least squares optimization problem in order to estimate the parameters by minimizing a pre-selected objective function. The error function or the objective function to be minimized can be defined as the sum of the squared differences between the measured current value and the modeled current value for the range of voltages considered. Expressed mathematically, one wishes to determine the model parameters I_{ph}, I_{sat}, n, R_s, and R_{sh}, such that the sum of the squared errors is minimized, i.e.,

$$\min_{I_{ph},I_{sat},n,R_s,R_{sh}} f = \sum_1^m \left(I_{model_i}\left(V_{meas_i}; I_{ph}, I_{sat}, n, R_s, R_{sh}\right) - I_{meas_i}\right)^2, \quad \text{... (3.16)}$$

where m is the number of experimental data points, I_{meas_i} and V_{meas_i} are i^{th} measured current and voltage pairs, respectively, I_{model_i} is the modeled current, f is the objective function to be minimized that provides for the squares of the difference between the measured current modeled current. Explicitly,

this objective function may be written as,

$$\min_{I_{ph},I_{sat},n,R_s,R_{sh}} f = \sum_{1}^{m}\left(\left\{I_{ph} - I_{sat}\left[\exp\left(\frac{V_{meas_i} + I_{meas_i}R_s}{nV_t}\right) - 1\right] - \frac{V_{meas_i} + I_{meas_i}R_s}{R_{sh}}\right\} - I_{meas_i}\right)^2.$$

… (3.17)

While a variety of approaches are available for solving such an optimization problem, the gradient based optimization technique is proposed due to the continuous nature of the model functions associated with the photovoltaic parameter estimation. In general, for the case of an objective function that takes in a vector of model parameters and returns a scalar, the solution of an unconstrained optimization problem is a point $\bar{x}^* \in N$ such that

$$\bar{x}^* = \underset{\bar{x} \in N}{\operatorname{argmin}}\ f(\bar{x}),\ such\ that\quad f(\bar{x}^*) \leq f(\bar{x}),\quad \forall\, \bar{x} \in N. \qquad \ldots(3.18)$$

In this case, such a point $\bar{x}^* \in R^n$ is a local minimizer for a neighborhood N of $\bar{x}^* \in R^n$ where the neighborhood of $\bar{x}^*$ constitutes an open set which contains $\bar{x}^*$, a local minimizer. These algorithms begin with an initial but sub-optimal guess, $\bar{x}_0$, and generate a sequence of iterations $\{\bar{x}_k\}\ k = 1,2,\ N$ to get closer to optimal solution with every iteration. The sequence is terminated when either an approximated solution with the desired accuracy is achieved or no further appreciable progress can be made. Different algorithms make different decisions in determining the direction of the search, i.e., how to move from current iterate $\bar{x}_k$ to the next iterate $\bar{x}_{k+1}$. In gradient based algorithms, the information of the first and second order partial derivatives of the objective functions is used to find the next iteration. The first order derivative of the objective function at a given point gives the gradient (slope) denoted as $\nabla f\ (\bar{x}) \in R^n$.

The second order derivative of the objective function at a point gives the Hessian (curvature) denoted as $\nabla^2 f\ (\bar{x})$. The gradient and Hessian are expressed as,

$$\text{Gradient, } \nabla f = \left[\frac{\partial f}{\partial x_1} \quad \frac{\partial f}{\partial x_2} \quad \cdots \quad \frac{\partial f}{\partial x_n}\right]^T, \qquad \text{... (3.19)}$$

$$\text{Hessian, } \nabla^2 f = \begin{bmatrix} \frac{\partial^2 f}{\partial x_1^2} & \cdots & \frac{\partial^2}{\partial x_1 \partial x_n} \\ \vdots & \ddots & \vdots \\ \frac{\partial^2 f}{\partial x_n \partial x_1} & \cdots & \frac{\partial^2 f}{\partial x_n^2} \end{bmatrix}. \qquad \text{... (3.20)}$$

The gradient and Hessian of the objective function are used to define the two sufficient conditions for the convergence to a solution, often referred to as first order and second order optimality conditions, respectively. These conditions are defined as;

1. First order optimality: If $f\ (\bar{x}^*)$ is a local minimizer and f is continuously differentiable in an open neighborhood of $\bar{x}^*$, then

$$\nabla f\ (\bar{x}^*) = 0. \qquad \text{... (3.21)}$$

2. Second order optimality: If $f\ (\bar{x}^*)$ is a local minimizer of f and $\nabla^2 f\ (\bar{x}^*)$ is continuous in an open neighborhood of $\bar{x}^*$, then $\nabla f\ (\bar{x}^*) = 0$ and

$$\nabla^2 f\ (\bar{x}^*) \text{ is positive semi-definite (i.e., } \nabla^2 f\ (\bar{x}^*) \geq 0). \qquad \text{... (3.22)}$$

These are sufficient conditions for a solution, i.e., if $\bar{x}^*$ is a minimum, then the two conditions must hold. The first order condition ensures that $\bar{x}^*$ is a minimum. The second order sufficient conditions guarantees that $\bar{x}^*$ is a local minimizer of f and the convexity of f guarantees that any local minimizer is a global minimizer. Gradient-based optimization algorithms find a minimizer by searching for points that

satisfy these optimality conditions. Such algorithms use one of the two fundamental strategies for finding the next iterate, which are;

1. Line Search Method: These algorithms reduce the n-dimensional optimization problem,

$$\min_{\bar{x} \in R^n} f(\bar{x}),$$

to a one-dimensional problem

$$\min_{\alpha>0} f(\bar{x}_k + \alpha \bar{s}_k),$$

where $\bar{s}_k$ is the search direction of choice. This search direction is the descent direction, typically given by the negative of the gradient vector, i.e., $-\nabla f\ (\bar{x}^*)$ at the current iteration, $\bar{x}_k$. In each iteration, a line search controlled by step length α, is employed in the search direction of $\bar{s}_k$ to find the next iteration. The approach employed to select $\bar{s}_k$ determines how the algorithm progresses.

2. Trust region method: The trust region method works in a different manner, wherein instead of searching along a line, the next iteration is computed by searching in a "trust region", which is in the neighborhood of the current iteration. With respect to nonlinear parameter estimation, trust region strategies are a relatively new optimization technique that has matured in recent years [65]. Leverberg's pioneering work on modifying the Hessian [66] and the subsequent contribution of Marquardt in controlling the step length [67], are some of the early works that laid the foundation for trust region algorithms. The trust region concept was suggested by Powell for the convergence of an unconstrained optimization problem [68]. Trust region strategies have gained significant attention

from researchers and have been used extensively in many software packages, including MATLAB, R, Wolfram, Python, etc.

These algorithms use information about the objective function, gradient, Hessian, etc., to generate simpler models for the objective function around a given point (current iteration). This simple model function, m_k, that approximates the behavior of the objective function, f, in a neighborhood of a point, $\bar{x}_k$, may be given by a Taylor expansion as

$$m(x_k + s) = f(\bar{x}_k) + \bar{s}^T \nabla f(\bar{x}_k) + \frac{1}{2} \bar{s}^T H_k \bar{s}\,, \quad \ldots (3.23)$$

where H_k is either the full Hessian $\nabla^2 f(\bar{x})$ which is expensive to produce or some clever approximation for the Hessian. The choice of the model function is kept simple, such as, the quadratic approximation for the objective function, so that the optimization sub-problem

$$\min_{s \in N(x_k)} m_k(\bar{x}_k + \bar{s}_k),$$

can be solved with little effort. The neighborhood $N(\bar{x}_k)$ of $\bar{x}_k$ specifies the region in which the model is trusted to represent the local behavior of the objective function more or less adequately. This neighborhood is referred to as the "trust region", and is typically a ball of radius Δ_k in R^n i.e.,

$$N(\bar{x}_k) = \{\bar{s} : \|\bar{s} - \bar{x}_k\| \leq \Delta_k\}. \quad \ldots (3.24)$$

Depending on the optimization problem, the trust region occasionally can be elliptical or box-shaped trust regions. The trust region sub-problem thus formed is solved to determine the trial step, $\bar{s}_k$, in the search direction [69]. Towards minimizing the trust region sub-problem, i.e., solving for $\bar{s}_k$, the sub-problem can be differentiated and set equal to 0, i.e.,

$$\nabla m_k(\bar{x}_k + \bar{s}_k) = \nabla f(\bar{x}_k) + \bar{s}_k H_k = 0$$

$$\Rightarrow \bar{s}_k = H_k^{-1} \nabla f(\bar{x}_k) \, . \quad \ldots (3.25)$$

The search direction is computed from the dot product of inverse of the Hessian matrix (or some approximate form of Hessian) and the gradient vector. When the full Hessian information is used for the computation of the trial step, the algorithm is called the Newton's algorithm, used in conjunction with the trust region strategy. Thus, starting with the initial sub-optimal solution, $\bar{x}_k$, the algorithm uses information about the slope (gradient) and curvature (Hessian) to solve for the trial step, $\bar{s}_k$, that is expected to produce a sufficient decrease in the model. For a decision regarding the success or failure of the computed trial step, the objective function at $\bar{x}_{k+1}$ is evaluated and a comparison is made between the achieved reduction in the objective function and the predicted reduction in the model. This comparison is defined via a merit function given as,

$$\rho_k = \frac{actual\ reduction}{predicted\ reduction} = \frac{f(x_k) - f(x_k + s_k)}{m_k(0) - m_k(s_k)}. \quad \ldots (3.26)$$

In the above expression, the predicted reduction is always non-negative, since the trial step, $\bar{s}_k$, is within the trust region. The merit function, ρ_k, can thus yield a negative value only when the function evaluated at the next iteration is greater that the function value at current iteration, i.e., $f(x_k + s_k) > f(x_k)$, a condition that is not desired. The decision on the size of the trust region, and whether to accept or reject the next computed trial step, is taken based on the state of the merit function, ρ_k, depending on the following decision criteria;

If $\rho_k < 0$, it is referred that the model is not a good approximation for the objective function and

hence, the trial step is rejected and the size of the trust region is reduced.

If $\rho_k \approx 0$, it suggests that the model is still a poor approximation, and therefore, the trial step may or may not be accepted; however, the size of the trust region is reduced.

If $\rho_k > 0 \; but \; not \approx 1,$ it suggests that the model is reasonable. Therefore, the trial step may be accepted while keeping the size of the trust region unchanged.

If $\rho_k \approx 1$, it is inferred that the model is a good approximation to the trust region, and hence, the trial step is accepted and the size of the trust region is increased.

This is repeated for each iteration until convergence is achieved. Figure 3.15 illustrates the scheme of convergence of trust region algorithm for a representative multivariate optimization problem $f(x_1, x_2)$ consisting of two design variables, x_1 and x_2. From the above discussion, it is clear that the most important part of a trust region algorithm is in finding the solution of the trust region sub-problem, which generates the trial step. The trust region trial step, s_k is computed by solving the trust-region sub-problem, i.e.,

$$\min_{\|s_k\| \leq \Delta_k} f_k + \nabla f(\bar{x}_k)^T s_k + \frac{1}{2} s_k^T H_k s_k.$$

Different trust region strategies are available to solve for the trust region sub-problem. The choice of the algorithm is governed by the condition of the Hessian of the objective function. One of the fundamental approaches to calculate the trial step is to minimize the model function along the steepest descent direction, $-\nabla f(x_k)$, which is termed the Cauchy point. The Cauchy point is readily computed from a vector of length Δ_k in the steepest descent direction, i.e.,

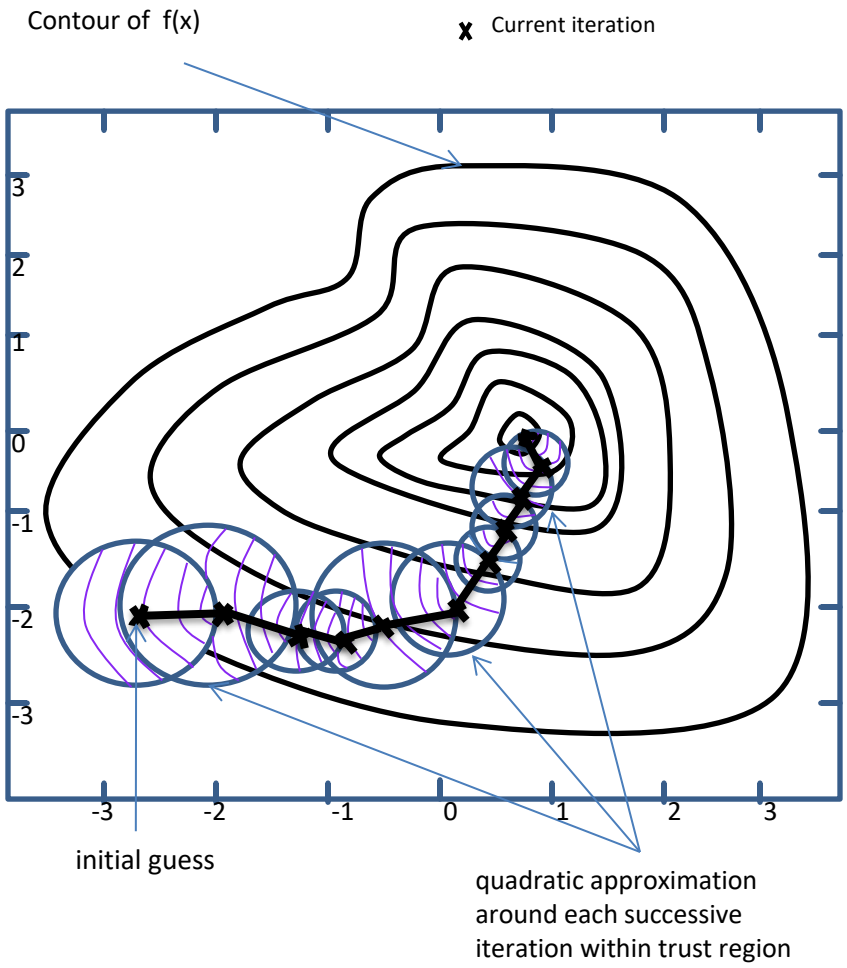

Figure 3.15: Illustration of the scheme of convergence of a representative multivariate (two variables for this case) optimization problem based on trust region optimization algorithm. The online version of this figure is in color.

$$s_k^s = \frac{-\nabla f(x_k)}{\|\nabla f(x_k)\|}\Delta_k \, . \quad \text{... (3.27)}$$

where $\bar{s}_k$ is the steepest descent point. The Cauchy point, in explicit form, can be given by

$$s_k^c = \tau_k s_k^s, \quad \text{... (3.28)}$$

where the choice of τ_k is based on the condition of the Hessian, so that the trust region condition of the trial step being within the trust region, i.e., $\|s_k^c\| \leq \Delta_k$, is satisfied. Typically, τ_k is chosen based on following condition;

$$\tau_k = \begin{cases} 1, & \text{when the Hessian is positive definite} \\ min\left(1, \frac{\|\nabla f(x_k)\|^3}{\Delta_k \nabla f(x_k)^T H_k \nabla f(x_k)}\right), & \text{otherwise} \end{cases} . \quad \text{... (3.29)}$$

The Cauchy point is essentially a line search in the steepest descent direction within the trust region which results in slower convergence. The convergence can be improved using what is known as the Dogleg method when the Hessian is positive definite [68]. In this method, the solution of the trust region sub-problem is sought along a path consisting of two-line segments; a step along the steepest descent direction and a full step, or Newton step. The solution of the trust region sub-problem, when traced as a function of the radius of the trust region, indicates that for smaller radii, the search direction is approximately given by $-\nabla f(x_k)$, which is a step in the steepest descent direction. For a larger radii trust region, the solution is the minimum of the quadratic model given by the full step, i.e., $-H_k^{-1}\nabla f(x_k)$. Dogleg algorithms attempt to optimize the model $m_k(x_k)$ along this approximate path (formed by the two-line segments in the shape of a dog leg) subject to the trust region constraint. Along the steepest descent, the unconstrained minimum of $m_k(x_k)$ is given by

$$s_k^U = \frac{\nabla f(x_k)^T \nabla f(x_k)}{\nabla f(x_k)^T H_k \nabla f(x_k)}. \quad \ldots (3.30)$$

The global minimizer of the quadratic model is given by

$$s_k^B = -H_k^{-1} \nabla f(x_k). \quad \ldots (3.31)$$

The Dogleg path, $s_k(\tau), \tau \in [0,2]$, is defined by

$$s(\tau) = \begin{cases} \tau s_k^U, & 0 \leq \tau \leq 1 \\ \tau s_k^U + (\tau - 1)\left(s_k^B - s_k^U\right), & 1 \leq \tau \leq 2 \end{cases}. \quad \ldots (3.32)$$

The optimum along the Dogleg path is achieved at the point where this approximate path exits in the trust-region (if it does), otherwise the full step is allowed and optimal. Improvements to the Dogleg method can be achieved when, instead of searching for the optimal solution along the approximate (Dogleg) path in one-dimension, the solution can be extended to search for the optimal over the entire two-dimensional plane spanned by the steepest descent vector, s_k^U, and the full step vector, s_k^B [69]. This approach is called two-dimensional subspace optimization. For a positive definite Hessian, the optimum is computed by minimizing the following sub-problem

$$\min_{s_k} \left[f(x_k) + \nabla f(x_k)^T s_k + \frac{1}{2} s_k^T H_k s_k \right]$$

$$subject\ to\ \|s_k\| \leq \Delta_k,\ s_k \in span\left[\nabla f(x_k), H_k^{-1} \nabla f(x_k)\right]$$

A distinct advantage of this approach is that it can be extended to cases where the Hessian is indefinite. For an indefinite Hessian with negative eigenvalues, the two-dimensional subspace is modified as

$$s_k \in span[\nabla f(x_k), (H_k + \alpha I)^{-1} \nabla f(x_k)],\ \ \alpha \in (-\lambda_1, -2\lambda_1),$$

where λ_1 is the most negative eigenvalue of H_k. There are other similar optimization algorithms within

the trust region strategies that have been used for computing the trial step. For our requirement of parameter estimation, a two-dimensional subspace approach will be employed to compute the search direction.

Having established the trust region strategy to be employed, now the problem of formulating the optimization problem of parameter estimation from the current-voltage characteristics of a photovoltaic device is examined. The discussion so far considered that the objective function takes in a vector (of model parameters) and returns a scalar value. Often the model parameters and the input variable may be vectors, so that the output function is also a vector. This is especially true when the effects of measurement error are included or when the measurement is taken at different instances of input variable, which produces a different output for each measurement. In such a case, the optimization problem may be given as,

$$\min_{\bar{x} \in R^n} f_i(z_i; \bar{x}),\ i = 1,2,..m,\ \ subject\ to\ \begin{cases} c_j(\bar{x}) = 0, j\ \in E \\ c_j(\bar{x}) \geq 0, j\ \in I \end{cases}, \qquad \text{...(3.33)}$$

where $(z_i, f_i(z_i, \bar{x}\ ))$ is the set of input-output data pairs corresponding to each i^{th} measurement. Such specialized forms of the objective function are common in data fitting where the requirement is to find the optimal model parameter set that best fits some observed data and prior information. The objective function is essentially a measure of misfit or prediction error between the observed data and the values predicted by the model. The optimization problem is to find the model parameter values that satisfy the constraints and results in the smallest misfit, or prediction error, with the observed data. As suggested by Eqs. (3.18) and (3.19), parameter estimation, corresponding to the current-voltage characteristics of a

given photovoltaic device, can therefore be formulated as a non-linear least squares optimization problem.

In nonlinear least-squares optimization problems, given m observed data points is,

$$(z_i, y_i), i = 1,2, \dots m, \quad \dots (3.34)$$

where z_i is the input variable and y_i is the observed output or response, the vector, $\bar{x}_n$ of n model parameters, gives the "best fit" in the least squares sense to the model function

$$y_i = g(z_i; \bar{x}_n), \quad \dots (3.35)$$

where g is a nonlinear function of $\bar{x}_n$. In such optimization problems, the objective function may be given by a sum of large number of squared residuals,

$$f(\bar{x}_n) = \sum_{i=1}^{m} (g(z_i; \bar{x}_n) - y_i)^2 = \sum_{i=1}^{m} r_i(\bar{x}_n)^2 . \quad \dots (3.36)$$

Here, each residual, $r_i(\bar{x}_n)$, is non-linearly dependent on the model parameters, $\bar{x}_{n,}$ and the minimization of $f(\bar{x}_n)$ thus forms a nonlinear least squares problem. The objective function $f(\bar{x}_n)$ has a special form

$$f(\bar{x}_n) = \frac{1}{2}\sum_{i=1}^{m} r_i(\bar{x}_n)^2, \quad \bar{x}_n \in R^n, \quad \dots (3.37)$$

where the problem is scaled by $\frac{1}{2}$ to make the derivatives (to be used subsequently) less cluttered. Here $m \geq n$ so that there are more residuals (equations) than dimensions (model parameters or variables) and hence is referred to as an over-determined problem. This special form of the least-squares-objective makes it easier to solve than general non-linear minimization problems. For this, the residual vector can be represented as

$$r(\bar{x}_n) = [r_1(\bar{x}_n), r_2(\bar{x}_n), r_3(\bar{x}_n), \dots, r_m(\bar{x}_n)]^T. \quad \dots (3.38)$$

The objective can thus be written as

$$f(\bar{x}_n) = \frac{1}{2} r(\bar{x}_n)^T r(\bar{x}_n) = \frac{1}{2} \|r(\bar{x}_n)\|_2^2, \quad \text{… (3.39)}$$

where $\|.\|_2$ is the Euclidean norm. The derivative of the objective function, $f(\bar{x}_n)$, may be expressed in terms of Jacobian of $r(\bar{x}_n)$ which is an $m \times n$ matrix of the first order partial derivatives, given as

$$J(\bar{x}_n) = \left[\frac{\partial r_j(\bar{x}_n)}{\partial x_i}\right]_{\substack{j=1,2,\dots,m \\ i=1,2,\dots,n}} = \begin{bmatrix} \frac{\partial r_1}{\partial x_1} & \dots & \frac{\partial r_1}{\partial x_n} \\ \vdots & \ddots & \vdots \\ \frac{\partial r_m}{\partial x_1} & \dots & \frac{\partial r_m}{\partial x_n} \end{bmatrix}, \quad \text{… (3.40)}$$

where $J(\bar{x}_n)$ is the Jacobian of the objective function. Using the Jacobian notation, the gradient, $\nabla f(\bar{x}_n)$, can be expressed as

$$\begin{aligned} \text{Gradient, } \nabla f(\bar{x}_n) &= \sum_{j=1}^{m} r_j(\bar{x}_n) \frac{\partial r_j(\bar{x}_n)}{\partial x_i}, i = 1,2, \dots, n \\ &= \sum_{j=1}^{m} r_j(\bar{x}_n) \nabla r_j(\bar{x}_n) \\ &= J(\bar{x}_n)^T r_j(\bar{x}_n). \end{aligned} \quad \text{… (3.41)}$$

The gradient $\nabla f(\bar{x})$ can thus be easily computed using the Jacobian. Similarly, the Hessian, $\nabla^2 f(\bar{x}_n)$, of the objective function can be expressed as

$$\begin{aligned} \text{Hessian, } \nabla^2 f(\bar{x}_n) &= \sum_{j=1}^{m} \nabla r_j(\bar{x}_n) \nabla r_j(\bar{x}_n)^T + \sum_{j=1}^{m} r_j(\bar{x}_n) \nabla^2 r_j(\bar{x}_n) \\ &= J(\bar{x}_n)^T J(\bar{x}_n) + \sum_{j=1}^{m} r_j(\bar{x}_n) \nabla^2 r_j(\bar{x}_n). \end{aligned} \quad \text{… (3.42)}$$

It is evident that the second part of the Hessian is the product of the residuals $r(\bar{x}_n)$ and its second-order derivatives. In many applications, the residuals are typically small, and for a very good fit, can be equivalently taken to be 0. For this reason, the second-order term can be ignored and hence, an explicit

computation of the full Hessian can be avoided. Thus, the Jacobian gives us the first "half" of the Hessian $\nabla^2 f(\bar{x})$ without the need of computing any second order derivatives. With this, it can be approximated that $\nabla^2 f(\bar{x}) = J(\bar{x})^T J(\bar{x})$ so that a good approximation for the Hessian, without computing any second derivatives which can often be computationally challenging can be determined. This algorithm is termed as a Gauss-Newton algorithm, which exploits the special structure of the gradient and Hessian and, as such, can only be used for the case of minimization of sum of squared function values.

In summary, parameter estimation for photovoltaic devices can be explained as follows; the information of the gradient and Hessian computed based on the Gauss-Newton algorithm is used to minimize the quadratic approximation of the objective function, i.e., computation of the trial steps, s_k. For this, the Jacobian $J(\bar{x})$ of the objective function $F(\bar{x}_k)$ is used to help define the two-dimensional subspace. In this regard, calculations of the second derivatives of the residual function $r_i(\bar{x}_k)$ are not used. Based on the computed trial step, s_k, the state of the merit function, ρ_k, is evaluated. Depending on the merit function, ρ_k, the trust region radius is either expanded or shrunk and similarly the next iteration is accepted or rejected. The algorithm is given below;

1. Given the initial guess, $\bar{x}_0$, set, current iteration number $k = 1$, the maximum allowed trust region radius $\Delta_{max} > 0$, trust region radius for initial iteration $\Delta_0 \in (0, \Delta_{max})$ and constant $\eta \in \left(0, \frac{1}{4}\right)$.
2. While the optimality condition is not satisfied, continue with the following steps.
3. Formulate a trust region sub-problem using non-linear residual functions.

4. Form the Jacobian and Hessian approximation to get s_k', i.e., approximate the Gauss-Newton solution.

5. Use the Gauss-Newton solution to define the two-dimensional subspace, S, spanned by the steepest descent and full-step.

6. Optimize the approximate model in the two-dimensional subspace, S.

7. Evaluate, $\rho_k = \frac{f(x_k) - f(x_k + s_k)}{m_k(0) - m_k(s_k)}$.

8. If $\rho_k < \frac{1}{4}$, then reduce the trust region radius for the next iteration

$$\Delta_{k+1} = \frac{1}{4}$$

Else, if $\rho_k < \frac{3}{4}$, and $\|\bar{s}_k\| \leq \Delta_k$, then increase the trust region radius

$$\Delta_{k+1} = \min(2\Delta_k, \Delta_{max})$$

Else, keep the trust region radius unchanged

$$\Delta_{k+1} = \Delta_k$$

9. If $\rho_k > \eta$, then accept the computed trial step to go to next iterate

$$x_{k+1} = x_k + s_k$$

Else reject the computed trial step

$$x_{k+1} = x_k$$

10. Update the iteration counter and repeat until convergence is achieved.

Chapter 4 Analysis

4.1 Overview

Photovoltaic devices, i.e., solar cells or modules, can be characterized using a variety of different means. The approach employed is often tied with the level of abstraction within which the analysis is to be pursued. At the materials level, the materials found within such devices can be characterized in terms of the microscopic phenomena that occur within them. Accordingly, the charge-carrier generation rate, the charge-carrier recombination rate, the quantum efficiency, and other material related properties, become the performance metrics of interest. From these basic material parameters, the performance of a photovoltaic device may be predicted. At the device level, however, photovoltaic performance metrics, such as the maximum output power, the efficiency, the fill-factor, and other device performance metrics, become the priority. While material characteristics are extensively used in the research activities pursued during the design of a new photovoltaic device, for commercial applications, device characteristics are more often considered. This is because device characteristics are more closely related to the commercial applications envisaged for photovoltaic devices. For the purposes of this thesis, the macroscopic performance metrics corresponding to the photovoltaic devices, will be considered. The device performance of a given photovoltaic device is often ascertained through the measurement of the current-voltage characteristic at a specific set of controlled operating conditions, referred to as standard testing conditions. For the purposes of such a test, a solar simulator is often employed, such a simulator imitating the solar spectrum corresponding to the Sun.

The current-voltage characteristic associated with a given photovoltaic device, i.e., a solar cell or module, carries a wealth of information. Certain key features, embodied within the current-voltage characteristic, are commonly used in characterizing the performance of such a photovoltaic device, especially its electrical power generating capabilities. Photovoltaic device manufacturers usually perform quick measurements of the current-voltage characteristics corresponding to their mass produced photovoltaic devices, and then use these measurements as a quality-check for their finished products. This quality check may be used in order to reject photovoltaic devices that are deemed inadequate, or as a means of categorizing adequate photovoltaic devices into various groupings based on their performance, as determined from the corresponding current-voltage characteristics. Key features, in particular, the open-circuit voltage, the short-circuit current, and the maximum power output, are identified from the measured current-voltage characteristics, these values being used for this quality-control step. Quality control is ensured by selecting a minimum threshold of performance, as judged by the aforementioned photovoltaic performance metrics, rejecting any device that is judged to be less than the "minimum" standard, as defined by the application at hand. This approach utilizes a few salient features of the corresponding current-voltage characteristic in order to characterize a given device. It, however, does not utilize the full range of information that can be extracted from the current-voltage characteristic; this may be viewed as a weakness in the quality-control that is currently commonly used in the photovoltaic device fabrication processes.

In this analysis, an alternative approach is pursued. Rather than determining performance metrics

directly from the current-voltage characteristic, the modeling parameters corresponding to each acquired current-voltage characteristic will be extracted instead. These modeling parameters correspond to an empirical model for the current-voltage characteristic. In this thesis, a technique, whereby this parameter extraction process may be pursued, is developed, this technique offering an advantage over that commonly employed in the field. The eventual goal of this work is to be able to extract current-voltage modeling parameters directly from a given current-voltage characteristic, and to be able to ascertain, based on these modeling parameters, as to whether or not such a photovoltaic device meets the minimum required for the photovoltaic device application being considered. Categorizing photovoltaic devices based on the results of this parameter extraction approach could potentially be pursued building upon these results. We suspect that many of these empirical modeling parameters are directly related to the fundamental material properties of the materials being employed within photovoltaic devices, and thus, present parameter extraction as offering an opportunity to perform materials characterization, albeit indirectly. For the purposes of this particular analysis, however, parameter extraction in of itself will be the focus, which will be pursued within the framework of the elementary single-diode model defined in Chapter 3. In the single-diode model, the empirical model parameters to be considered include the photo-generated current, the reverse saturation current, the diode ideality factor, the series resistance, and the shunt resistance, these parameters being introduced in Eq. (3.3).

This chapter is organized in the following manner. Section 4.2 presents the experimental data at hand that is to be examined using the proposed parameter extraction process. In Section 4.3, the aim and

scope of the proposed work is defined. In Section 4.4, the computational scheme, through which the model parameters, corresponding to a given photovoltaic device, may be extracted from the experimentally measured current-voltage characteristic is featured. Section 4.5 discusses the conditioning of the measured data needed to provide an initial guess for the model parameters with respect to the requirements of the adopted algorithm so as to find an optimal solution. In Section 4.6, the application of the optimization algorithm is presented through use of the current-voltage characteristic corresponding to a representative sample photovoltaic module from the pool of the measured data at hand. In this regard, the intermediate results, that show the workings of the algorithm and the trend of convergence, are discussed along with the extracted parameters based on the optimization. A benchmark analysis, based on standard photovoltaic device experimental data, is then pursued in Section 4.6. Finally, building upon the findings of Section 4.6, in Section 4.7, the extracted model parameters corresponding to the experimental data is analyzed and discussed in its entirety.

4.2 Discussion of the experimental data

The current-voltage characteristics, corresponding to a variety of photovoltaic devices, are considered in this analysis. These characteristics have been acquired at the facility of our industrial partner, who wishes to remain anonymous. For every photovoltaic module considered, after the final stage of assembly, the current-voltage characteristics were acquired through the use of a solar simulator. Within this solar simulator, every module is exposed with a bright flash pulse discharged from a xenon arc lamp for a brief period of time. Simultaneously, the module is swept, from short-circuit to open-circuit

conditions via an electronic load, and the corresponding voltage and current signals are recorded. The details of the measurement process have been presented in Chapter 3. It should be noted that for the experimental measurements of the current-voltage characteristics, no control over the constituent components/materials used for the production of the photovoltaic modules under study was possible; these were determined solely by our industrial partner. That is, there was no option to choose the type of photovoltaic solar cells (or the number of cells connected in series) to be used in the photovoltaic modules under study. However, by aligning the schedule for the measurement of the current-voltage characteristics with the production schedule, current-voltage characteristics, corresponding to different categories of the photovoltaic product, were acquired, so as to include different semiconductor materials used and different device configurations (size) in the study. For this, the modules, made up of both mono-crystalline and poly-crystalline photovoltaic cell, were measured. Furthermore, since the photovoltaic modules come in different configurations or sizes based on the number of photovoltaic cells connected in series, in this study, modules of the two most popular sizes (configuration), i.e., 60 solar cells and 72 solar cells, are included. Therefore, in totality, the current- voltage characteristics, corresponding to the ten samples of each 60 cell modules with mono-crystalline and poly-crystalline photovoltaic cells, and eleven samples of 72 cell modules, with mono-crystalline cells, were recorded. Due to limitations on time, the current-voltage characteristics corresponding to 72 cell modules with poly-crystalline photovoltaic solar cells could not be measured. Table 4.1 tabulates the different photovoltaic modules, whose current-voltage characteristics were determined. For ease of identification, each module is labeled based on the

nomenclature indicated in Table 4.1. The label is a combination of alphanumeric characters beginning with either M for mono-crystalline or P for poly-crystalline, followed by two digits indicating the number of cells connected in series (size). This is followed by 3 digits indicating the rated peak power of the sample, while the alphanumeric series of 3 characters is an acronym for the sample, followed by a serial number indicated by the next 1 or 2 digits. Thus, the modules are classified based on the both types of semiconductor material (type of cell) and the number of cells connected in series. Figure 4.1 presents the current-voltage characteristic corresponding to one such representative photovoltaic module sample, M60-275-SMP1. For the purposes of this analysis, first this particular current-voltage characteristic, corresponding to the sample M60-275-SMP1 will be used. The same procedure is then used with the current-voltage characteristic corresponding to the other photovoltaic modules. It is worth mentioning that this analysis is equally applicable for the case of current-voltage characteristics of photovoltaic solar cells. For the purposes of describing the proposed algorithm, the following analysis will focus on the current-voltage characteristics associated with sample M60-P275-SMP1, which is a 60-cell mono crystalline silicon solar module.

4.3 Approach employed

In this chapter, the focus is on developing a computational approach that may be used for the extraction of model parameters corresponding to a given current-voltage characteristic.

Table 4.1: Classification of the different modules, whose current-voltage characteristics have been measured.

S.No.	Type of semiconductor material used	Number of Cells (connected in series)	Power category (peak Watts)	Sample Nomenclature
1	Poly-Crystalline	60	255	P60-P255-SMP1
2				P60-P255-SMP2
3				P60-P255-SMP3
4				P60-P255-SMP4
5				P60-P255-SMP5
6				P60-P255-SMP6
7				P60-P255-SMP7
8				P60-P255-SMP8
9				P60-P255-SMP9
10				P60-P255-SMP10
11	Mono-Crystalline	60	275	M60-P275-SMP1
12				M60-P275-SMP2
13				M60-P275-SMP3
14				M60-P275-SMP4
15				M60-P275-SMP5
16				M60-P275-SMP6
17				M60-P275-SMP7
18				M60-P275-SMP8
19				M60-P275-SMP9
20				M60-P275-SMP10
21		72	330	M72-P330-SMP1
22				M72-P330-SMP2
23				M72-P330-SMP3
24				M72-P330-SMP4
25				M72-P330-SMP5
26				M72-P330-SMP6
27				M72-P330-SMP7
28				M72-P330-SMP8
29				M72-P330-SMP9
30				M72-P330-SMP10
31				M72-P330-SMP11

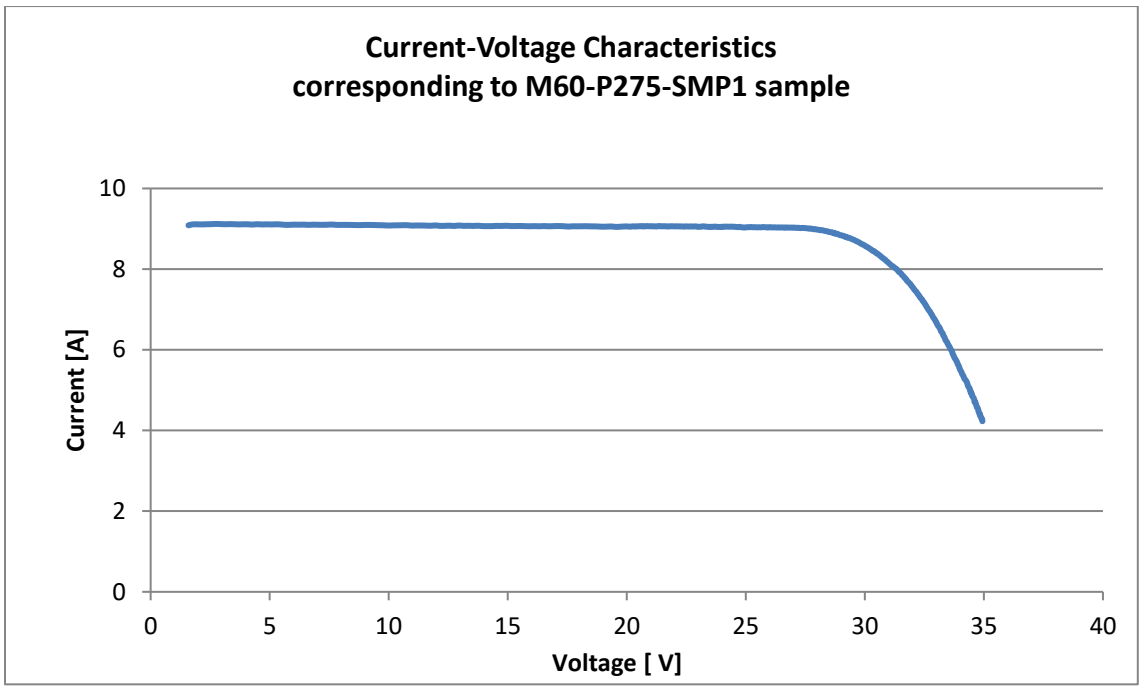

Figure 4.1: The current-voltage characteristic corresponding to the M60-P275-SMP1 sample (a 60-cell mono-crystalline silicon solar module) under standard testing conditions (defined as 1000 $W \cdot m^{-2}$ of irradiance of AM1.5G solar spectrum at a device temperature of 25°C). The online version of this figure is in color.

As discussed in Chapter 2, there are numerous techniques that have been employed for the extraction of model parameters corresponding to the current-voltage characteristics of a given photovoltaic device. These range from simple analytical methods that introduce a series of simplifications and approximations, resulting in a simpler solution using a reduced set of experimental data, to computationally demanding techniques that use powerful numerical tools. In recent years, many have adopted different advanced meta-heuristic optimization algorithms for curve fitting of the entire current-voltage characteristic, such techniques allowing for parameter extraction with improved accuracy. Optimizations, based on simulated annealing [38], particle-swarm [39] , pattern search [42], artificial-bee swarm [44], and other such approaches, represent the range of meta-heuristic optimization algorithms that have been used for photovoltaic parameter extraction of photovoltaic devices in the past. These optimization algorithms have been developed based on observations of some form of behavior (physical or social) of processes and entities. These algorithms will be compared and contrasted with the proposed algorithm based on an analysis of benchmark photovoltaic device experimental data.

The approach pursued within the framework of this thesis is based on a non-linear least-squares fitting with the measured current-voltage characteristic of a given photovoltaic device based on a simple trust-region optimization algorithm, the details of which are presented in Chapter 3. Using the proposed algorithm, parameter extraction will be performed corresponding to thirty photovoltaic devices based on their measured current-voltage characteristics. In this regard, as per the requirements of the adopted algorithm, an initial guess for the five model parameters based on the measured current-voltage data is

used. Since the adopted algorithm of the trust-region is an unconstrained optimization algorithm, a specific property of the algorithm will be utilized to constrain the search space of the model parameters to produce a feasible solution so that any possibility of unrealistic values of fitting parameters being extracted may be avoided. The progress of the algorithm is then traced through the analysis of a series of intermediate results. Finally, the optimal solution, i.e., the constellation of model parameters that corresponds to the least-squares error, is interpreted and contrasted with that obtained through the use of other approaches.

4.4 Non-linear least square optimization

Least-squares curve fitting approaches are widely used in statistical analyzes. The idea behind this approach is finding the set of model parameters which results in the least possible error between the modeled and experimentally measured values. For a least-squares fit of an experimentally acquired current-voltage characteristic corresponding to a photovoltaic device, i.e., the extraction of model parameters, one aims to minimize the least-squares sum of errors, i.e., the difference between the measured and modeled current values over the range of voltage values considered. For the purposes of this particular analysis, the trust-region reflective least-squares algorithm is employed, which is an iterative optimization approach that aims to minimize a given objective function.

For this optimization problem, the error function, or the objective function, to be minimized is defined as the sum of the squared differences between the measured current value and the modeled current value for the range of voltage values considered. Expressed mathematically, within the framework

of the single-diode model, one wishes to determine the model parameters, $R_s, R_{sh}, I_{ph}, I_{sat}$, and n, such that the sum of the errors is minimized. That is,

$$\min_{I_{ph},I_{sat},n,R_s,R_{sh}} e_i = \sum_{1}^{m} \left(I_{model_i}\left(I_{ph}, I_{sat}, n, R_s, R_{sh}\right) - I_{meas_i}\right)^2,$$

… (4.1)

where I_{model_i} is the model current based on the single-diode equivalent circuit model of the photovoltaic devices, as defined in Chapter 3, e_i is the objective function to be minimized, which provides for the sum of squares of the difference between the measured current, I_{meas_i} and the modeled current, I_{model_i}, m corresponding to the number of experimental data points. Explicitly, this objective function may be written as,

$$\min_{I_{ph},I_{sat},n,R_s,R_{sh}} e_i = \sum_{1}^{m} \left(\left\{ I_{ph} - I_{sat} \left[\exp\left(\frac{V_{meas_i} + I_{meas_i} R_s}{nV_t} \right) - 1 \right] - \frac{V_{meas_i} + I_{meas_i} R_s}{R_{sh}} \right\} - I_{meas_i} \right)^2 .$$

… (4.2)

where $R_s, R_{sh}, I_{ph}, I_{sat}$, and n are the five empirical model parameters introduced in Chapter 3.

4.5 Initial estimates of model parameters

The optimization algorithm, to be employed for the purposes of this analysis, requires a user-supplied initial estimate for the model parameters to initiate the iterative process. In our case, good starting estimates for the five model parameters to fit the measured current-voltage characteristic are

required. The five model parameters to be considered are the photo-generated current, the diode reverse saturation current, the diode ideality factor, the series resistance, and the shunt resistance. Initial estimates for the model parameters may be acquired directly from the current-voltage characteristics themselves. It is well known that the slope of the current-voltage characteristic at two distinct regions of the characteristic, namely, the short-circuit point and the open-circuit point, can be used to estimate the shunt and series resistance of a given photovoltaic device [28]. In particular, the negative of the reciprocal of the slope at the short-circuit point corresponds to an estimate of the shunt resistance, R_{sho}, and the negative of the reciprocal of the slope at the open-circuit point corresponds to an estimate of the series resistance, R_{so}. That is,

$$\text{Estimate of the shunt resistance, } R_{sho} = -\frac{dV}{dI}\Big|_{I_{sc}}, \quad \text{... (4.3)}$$

$$\text{Estimate of the series resistance, } R_{so} = -\frac{dV}{dI}\Big|_{V_{oc}}. \quad \text{... (4.4)}$$

For a given measured current-voltage characteristic, i.e., the 60-cell mono-crystalline silicon photovoltaic device (M60-P275-SMP1), illustrated in Figure 4.2, it can be seen that this characteristic exhibits two distinct gradients in the vicinity of the short-circuit and open-circuit points. To extract an initial estimate of the shunt resistance, linear regression is employed on the current-voltage characteristic over the linear region near the short-circuit point of the current-voltage characteristic, as depicted in Figure 4.3. Linear regression yields a negative slope of 0.00198 siemens over the linear region of the

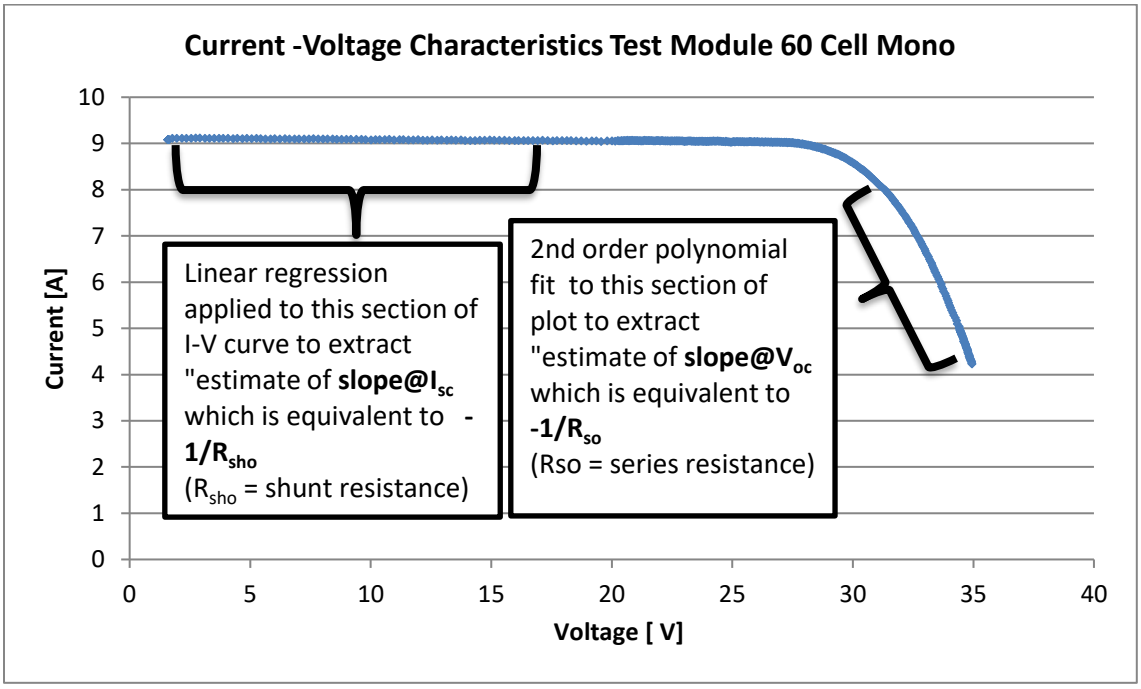

Figure 4.2: Current-voltage characteristics corresponding to M60-P275-SMP1 sample (a 60-cell mono-crystalline silicon solar module) under standard testing conditions. The section of the curve near the short-circuit point and the open-circuit point have been emphasized to indicate their correlation with the parasitic resistances. The online version of this figure is in color.

current-voltage characteristic. The negative reciprocal of this characteristic can be used to estimate the initial value of the shunt resistance, yielding a shunt resistance estimate of 505.051 Ω (standard regression error, R^2 = 0.72109). Similarly, another important deduction can be from the Figure 4.3 regarding the short-circuit current which is the fact that the short-circuit current of the photovoltaic device can be estimated through an extrapolation of the data based on the slope calculated from linear regression. Based on the obtained regression, it can be said that the short-circuit current through the photovoltaic device when the voltage is zero is calculated to be 9.10276 A (standard regression error, R^2 = 0.72109). Since the short-circuit current corresponds to the no-load condition, the photo-generated current is considered to be equivalent to the short-circuit current. Therefore, the initial estimate for the photo-generated current is set equivalent to the short-circuit current calculated from the earlier regression.

To extract an estimate for the series resistance, R_{so}, employing a second-order polynomial fit to the current-voltage data points over the region near the open-circuit voltage of the current-voltage characteristic, yields better results as compared with linear fitting. Figure 4.4 shows a second-order polynomial fit to the current-voltage characteristic near the open-circuit voltage point, V_{oc}, in the current-voltage characteristics. The solution of the second-order polynomial fit for the current-voltage data points can be used to extrapolate the data and gives the open-circuit voltage, which in this particular case was found out to be 37.342 V (standard regression error, R^2 = 0.999). Furthermore, the derivative of the same second-order polynomial evaluated at the open-circuit point yields the slope of the curve at the open-circuit voltage. This yields a negative slope of 2.07713 siemens over the region near the open-circuit point

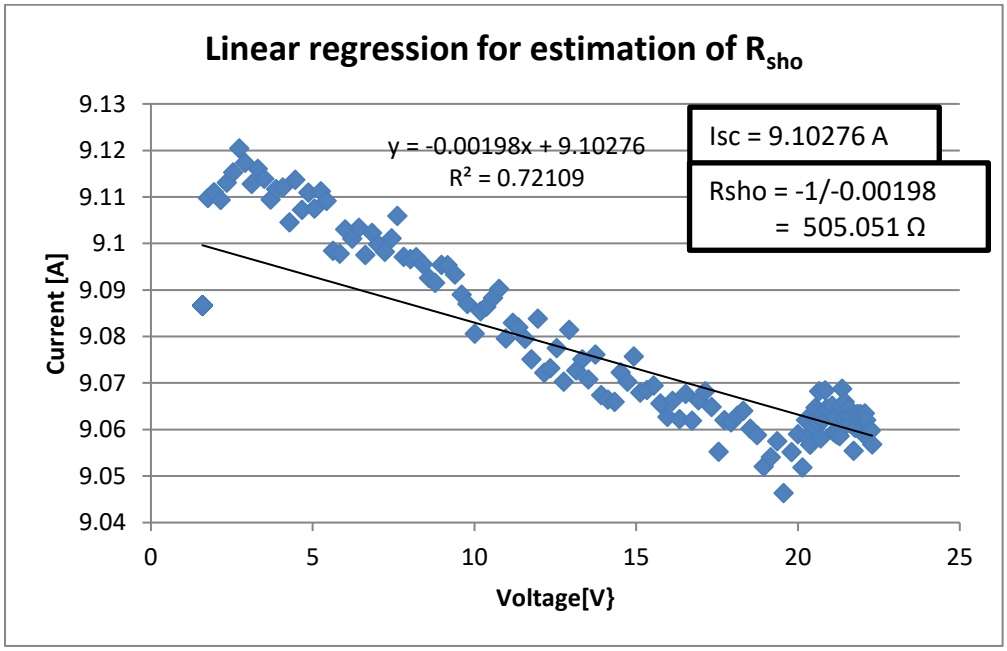

Figure 4.3: Linear regression applied on the measured current-voltage data points in the vicinity of the short-circuit point of the current-voltage characteristics of M60-P275-SMP1 sample for estimation of the initial value of shunt resistance. The online version of this figure is in color.

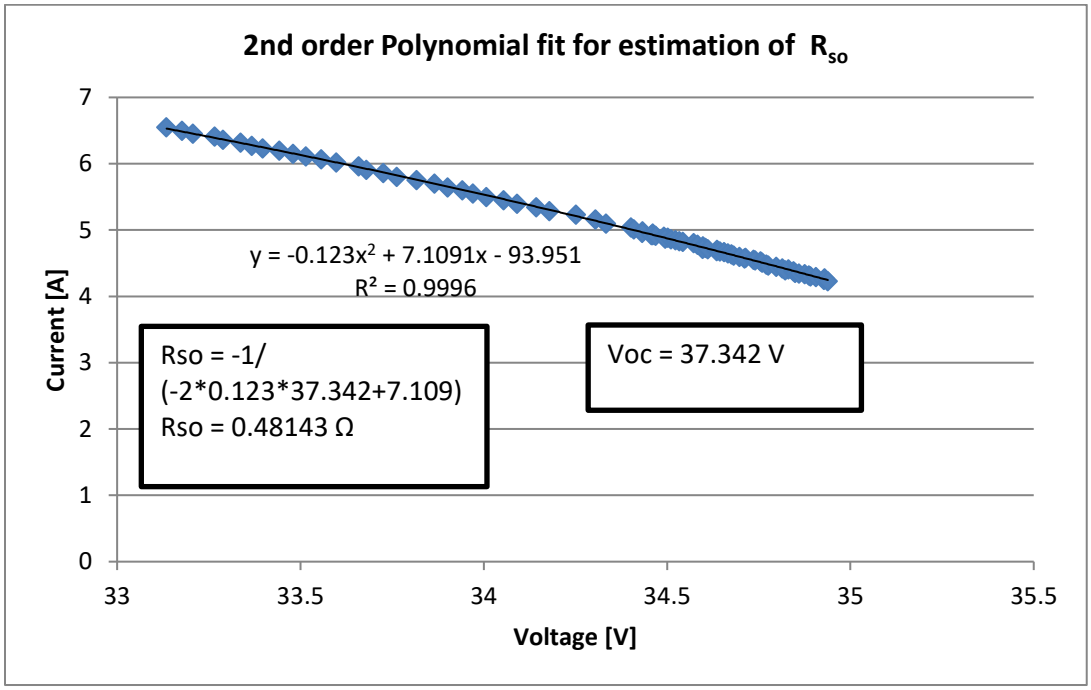

Figure 4.4: Second-order polynomial fits applied on the measured current-voltage data points in the vicinity of the open-circuit point of the current-voltage characteristics of the M60-P275-SMP1 sample for an estimation of initial value of the series resistance. The online version of this figure is in color.

of the current-voltage characteristic. Therefore, the negative reciprocal of the slope near the open-circuit voltage can be used to estimate the initial value of the series resistance, which in this case yields a series resistance estimate of 481.43 mΩ (with a standard error R^2 = 0.999).

Acquiring an estimate for the diode reverse saturation current, I_{sat}, and the diode ideality factor, n, presents a challenge. Due to the lack of a computational scheme aimed at directly arriving at an initial guess for these two parameters, an attempt to identify a suitable range of values so as to limit the search space and find a relatively centered starting point for the individual model parameters is pursued. In this regard, based on the fact that the diode ideality factor for silicon takes any value between 1 and 2 and depends on the material properties, a nominal value may be used as an initial estimate for the ideality factor. For most mono-crystalline silicon photovoltaic devices, the typical value for *n* ranges from 1 to 1.5 [35]. For this requirement of the ideality factor, a nominal value of 1.3, which is often referred to as a typical value for mono-crystalline silicon, is used. Based on this estimate for the ideality factor, a special case of the single-diode equivalent model, evaluated at the open-circuit point, is used in order to make an educated guess about the reverse saturation current, based on the following expression,

$$I_{sat} = \frac{I_{sc} - \frac{V_{oc}}{R_{sho}}}{\exp\left(\frac{qV_{oc}}{nk_BT}\right)}, \quad \ldots (4.5)$$

where I_{sat} denotes the saturation current, V_{oc} represents the open-circuit voltage, I_{sc} is the short circuit current, R_{sho} is the estimated initial values for the shunt resistance, q is the electron charge (1.6021×10^{-19} C), k_B is Boltzmann's constant (1.3806485×10^{-23} Joule per Kelvin), and T is the ambient

temperature. Once the initial estimates for the model parameters have been selected, the next step is used in order to define a suitable search space for the model parameters, i.e., definitions for the constraints associated with the parameters so as to avoid the possibility of the algorithm returning unrealistic values for the model parameters.

Assuming that these initial estimates are realistic "good" estimates, the search space or bounds on the model parameters is defined around the estimated values for the different model parameters. The bounds for the series resistance, R_s, the shunt resistance, R_{sh}, and, the photo-generated, I_{ph}, current may be defined so that they cover values within a certain percentage range around the respective initial estimates. As for the diode ideality factor, the bound was defined to cover reasonable values corresponding to mono-crystalline silicon, i.e., these values have been observed to range between 1 and 1.5. Furthermore, utilizing the relation defined through Eq. (4.5), two extremes for the diode ideality factor may be used in order to calculate the range of values expected for the corresponding reverse saturation current. Table 4.2 lists the initial estimates employed and the upper and lower bounds used for the case of the selected mono-crystalline 60 cell photovoltaic solar cells used in this analysis. These initial parameter selections, and their respective bounds, correspond to a particular 60 cell mono-crystalline silicon solar module. In a general sense, the same initial estimates and bounds may be used for modules from the same product category for the extraction of parameters. However, for a better result, it is advisable to use initial estimates calculated based on the above procedure using the respective current-voltage characteristics for each module.

4.6 Extraction of the model parameter from the current-voltage characteristics

Using initial estimates for the five-aforementioned single-diode model parameters and their respective bounds, in conjunction with the measured current-voltage data, non-linear least squares optimization may be employed for the purposes of parameter extraction. In this optimization process, one aims to minimize an objective function, which in our case is the error function, defined by the difference between the modeled and measured current values for the range of voltage values provided, as is set by Eq.(4.2). For such a problem, a trust region optimization algorithm can be employed, wherein the idea is to approximate the objective function, f, at x with a simpler function, m, that is valid in the neighborhood N around the point x. The simpler function is usually a quadratic approximation of f, defined by a Taylor approximation of f around x, and in the neighborhood defined as the trust region. A trial step, s, is computed by minimizing the model approximation over N. Once the trial step is computed, the current point is updated, and a decision, regarding the refinement of the trust-region, is made. The resultant least-squares fit, with respect to the current-voltage characteristic corresponding to the representative sample M60-P275-SMP1 module, along with intermediate fits, is shown in Figure 4.5. The obtained (optimal) model parameters, corresponding to the least-squares fit, are tabulated in Table 4.3, along with the initial estimates that were fed to the algorithm. The "goodness" of the fit is also traced quantitatively through the root-mean squares error of the optimal fit, tabulated in Table 4.4, along with the modeled peak power point, measured peak power point, and the percentage error between the two.

Table 4.2: List of initial estimates for the model parameters and the corresponding lower and upper bounds for the case of M60-P275-SMP1 sample.

Module	**60 cell Mono-crystalline Module (M60-P275-SMP1)**		
Parameters	**Estimated Values**	**Lower bound**	**Upper bound**
Shunt Resistance, R_{sh}	500 Ω	400 Ω	600 Ω
Series Resistance, R_s	0.49 Ω	0.3 Ω	0.65 Ω
Diode Ideality Factor, n	1.15	1	1.5
Diode Reverse Saturation Current, I_{sat}	4×10^{-9} A	1.7×10^{-12} A	9×10^{-6} A
Photo-generated Current, I_{ph}	10 A	8 A	11 A

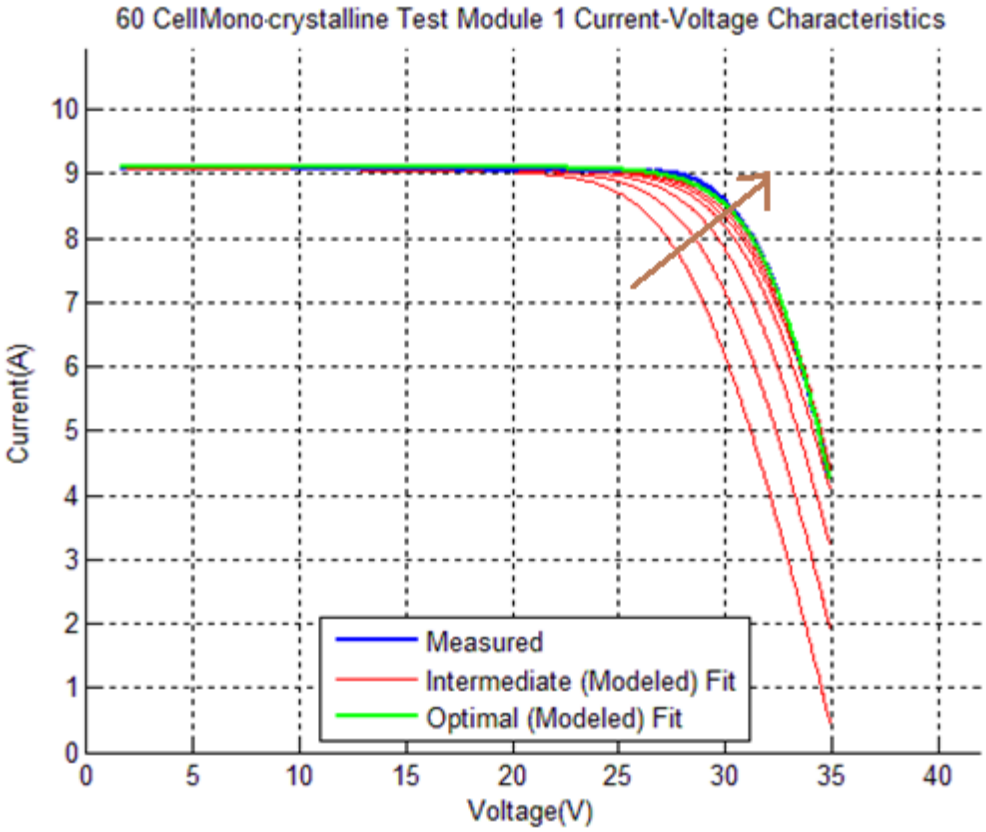

Figure 4.5: The intermediate current-voltage characteristics corresponding to successive iterations for the least-squares fitting process. The online version of this figure is depicted in color.

Table 4.3: List of initial estimates for the model parameters and the optimal modeling parameters extracted based on the least-squares fit corresponding to M60-P275-SMP1 sample.

Module	**60 cell Mono-crystalline Module (M60-P275-SMP1)**	
Parameters	**Estimated Values**	**Extract Parameters**
Shunt Resistance, R_{sh}	500 Ω	598.70 Ω
Series Resistance, R_s	0.49 Ω	0.31 Ω
Diode Ideality Factor, n	1.15	1.084
Diode Reverse Saturation Current, I_{sat}	4×10^{-9} A	1.095×10^{-9} A
Photo-generated Current, I_{ph}	10 A	9.603 A

Table 4.4: Metrics to indicate "goodness" of least-squares fit.

Module	**60 cell Mono-crystalline silicon photovoltaic solar cell Test Module # 1**
Measured Peak Power Point	276.43 Watts
Modeled Peak Power Point	273.99 Watts
Error in Peak Power Point	0.885 %
Root Mean Square Error	0.047

Figures 4.6, 4.7, 4.8, and 4.9 depict the speed for convergence of the algorithm. Two metrics, namely the norm of the residual and the root mean squares error during successive iterations, are plotted as a function of the number of iterations. The convergence rate of the trust-region least-squares is observed to be fast.

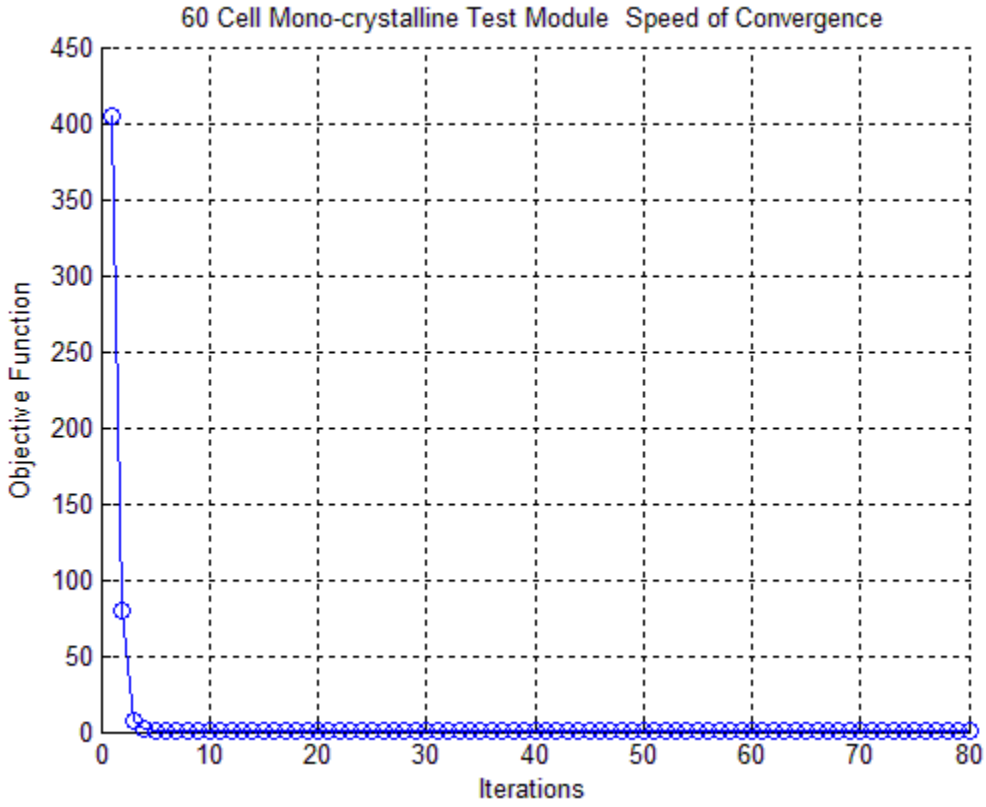

Figure 4.6: Speed of convergence based on the evaluation of objective function given by the norm of the residual during successive iterations, on a linear scale. The online version of this figure is in color.

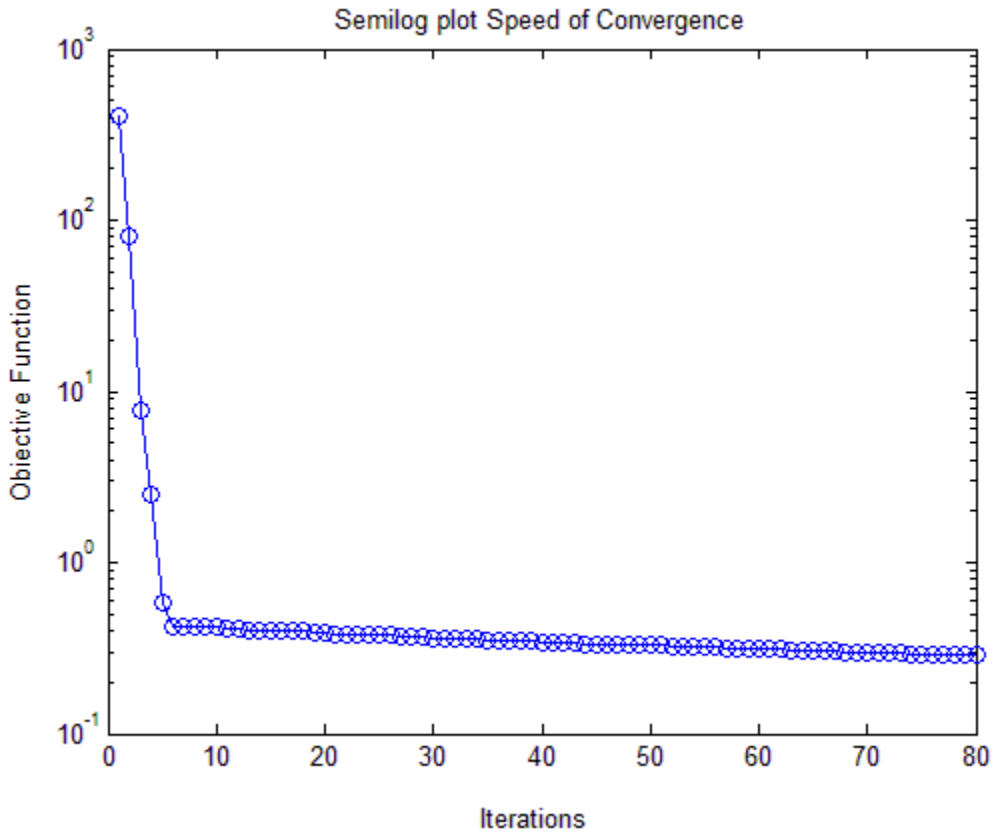

Figure 4.7: Speed of convergence based on the evaluation of objective function given by the norm of the residual during successive iterations, on a semi-logarithmic scale. The online version of this figure is in color.

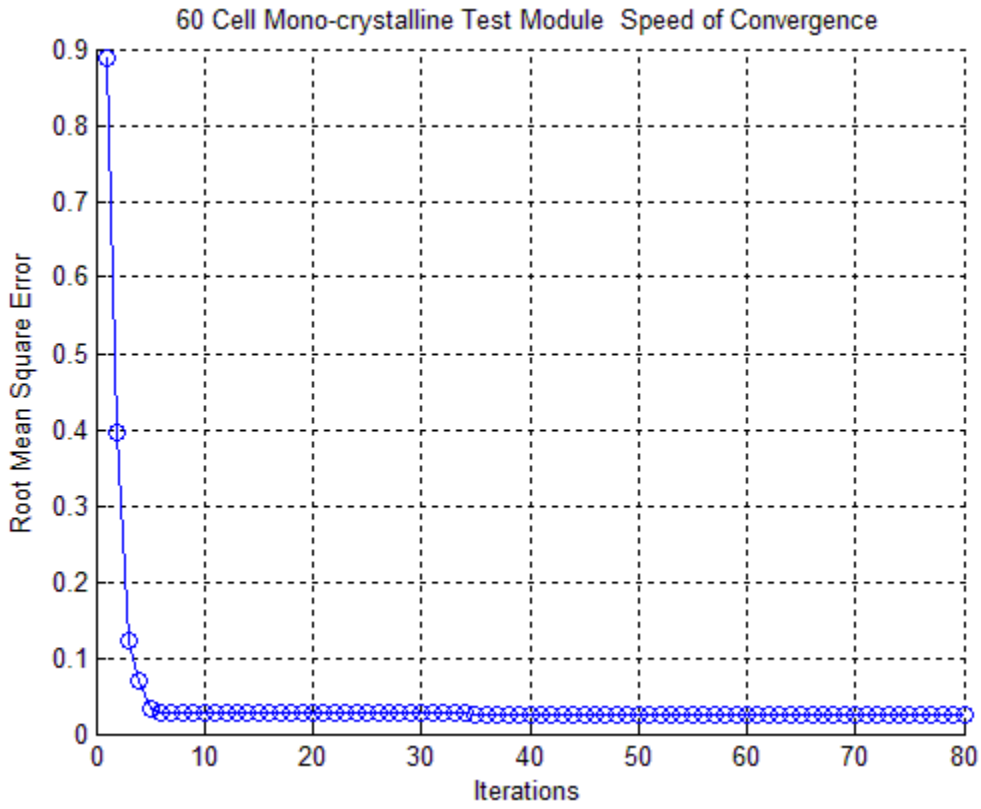

Figure 4.8: Speed of convergence based on the evaluation of root mean square error function during successive iterations, on a linear scale. The online version of this figure is in color.

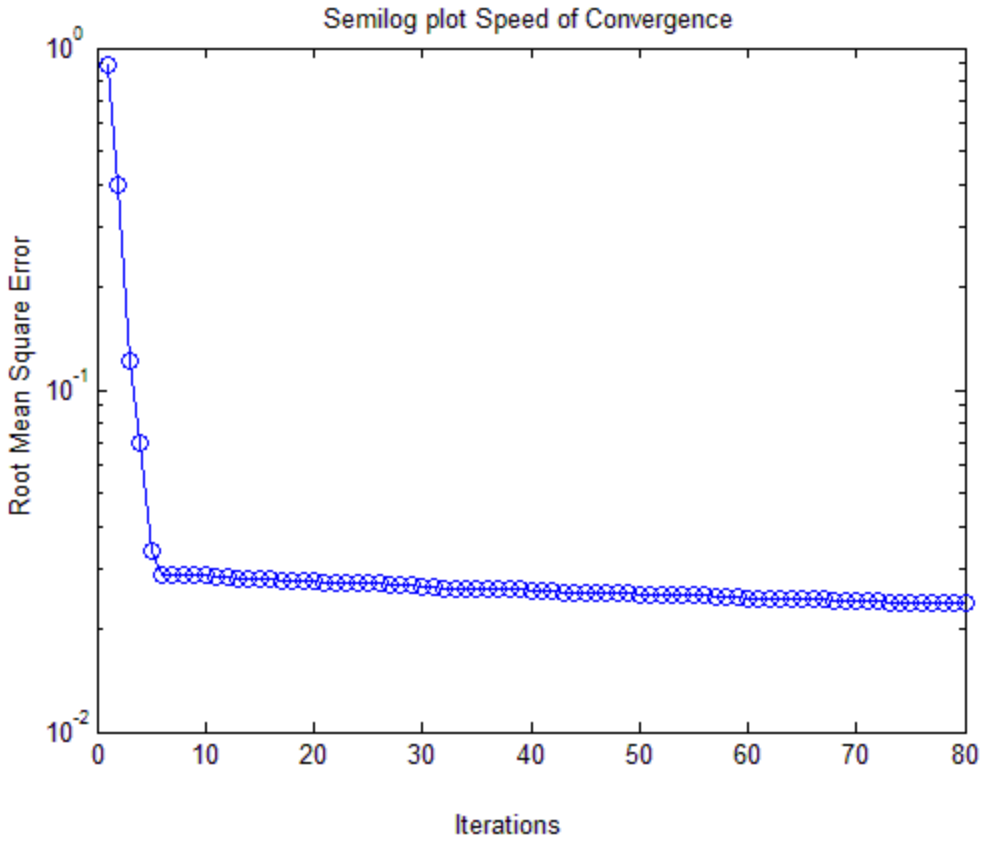

Figure 4.9: Speed of convergence traced based on the evaluation of root mean square error function during successive iterations, on a semi-logarithmic scale. The online version of this figure is in color.

4.7 Calibration for the parameter extraction algorithm

In order to measure the performance of the proposed algorithm employed for parameter extraction, it is instructive to compare the various algorithms that have been employed in the field with that employed by us. For the purposes of this analysis, benchmark current-voltage characteristic data, measured by Easwarkhanthan *et al.,* in 1986 are employed [70] . These data sets correspond to a 57 mm diameter commercial (RTC France) crystalline silicon photovoltaic solar cell measured at 33°C (for an irradiance set to 1000 $W \cdot m^{-2}$) and a 36 cell poly-crystalline silicon solar module (Photowatt-PWP 201) measured at 45°C (for an irradiance set to 1000 $W \cdot m^{-2}$). These case studies data are commonly used by others in order to test the effectiveness of the model extraction procedures and comparison of the extracted parameters.

For the first case, the measured current-voltage characteristic, corresponding to a 57-mm poly-crystalline silicon RTC France photovoltaic solar cell, was used to extract the modeling parameters based on the least-squares fitting algorithm, as discussed. Figure 4.10 shows the optimal least-squares fitting along with the intermediate fitting results as the optimization progresses through successive iterations. As is evident from the plot depicted in Figure 4.11, the least-squares fit appears to be very accurate, since the two plots are practically indistinguishable, i.e., as they overlap with each other nearly perfectly. This demonstrates the strength of the adopted optimization algorithm with respect to the estimation of model parameters. The root mean square error corresponding to the least-squares fitting proposed is compared

with those reported in literature, in Figure 4.12. The comparison shows that the proposed least-squares fitting approach based on trust region algorithm yields the least error producing the most optimal fit.

Initial estimates, corresponding to the model parameters and bounds that limit the search space in order to implement the algorithm, are tabulated in the Table 4.5. Based on these, the least-squares fitting of the measured current-voltage data corresponding to the RTC France photovoltaic solar cell, the optimal parameters set are extracted, and are tabulated in Table 4.6. Table 4.6 also includes the extracted model parameters corresponding to the same data set, as reported by other different authors based on different optimization approach. It is observed that the least-squares optimization algorithm, based on trust-region method, yields superior accuracy compared with the other optimization approaches listed in Table 4.6.

The speed of convergence for the optimization approach, with respect to the least-squares fitting of the measured current-voltage characteristic corresponding to RTC France photovoltaic solar cells, are traced based on the minimization of the objective function and the root mean square error as a function of the number of iterations. This is depicted in Figures 4.13 and 4.14, respectively.

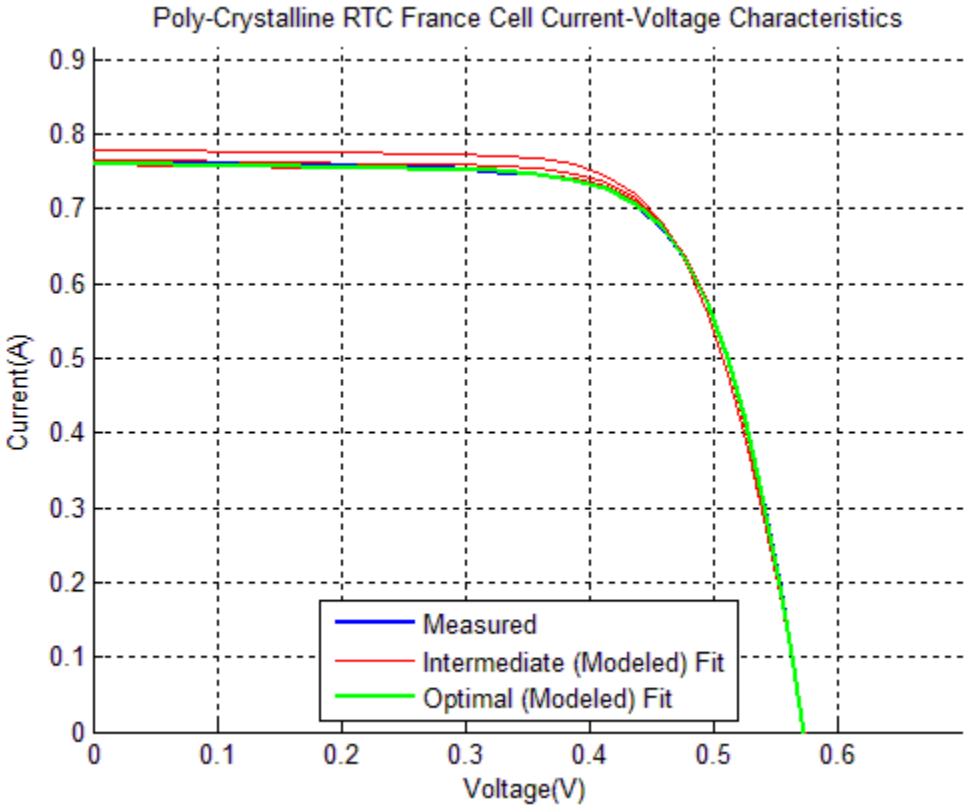

Figure 4.10: The intermediate current-voltage characteristics corresponding to the RTC France photovoltaic solar cell during successive iterations corresponding to the least-squares fitting process. The online version of this figure is depicted in color.

Table 4.5: List of the initial estimates of parameters and lower and upper bounds for the RTC France photovoltaic solar cell.

Module	**Cell Poly-Crystalline RTC France Cell**		
Parameters	**Lower bound**	**Upper bound**	**Estimated Values**
Shunt Resistance, R_{sh}	40Ω	70 Ω	60 Ω
Series Resistance, R_s	0.02Ω	0.095 Ω	0.06 Ω
Diode Ideality Factor, n	1.03	1.75	1.35
Diode Reverse Saturation Current, I_{sat}	1×10^{-10} A	9.06×10^{-6} A	5×10^{-8} A
Photo-generated Current, I_{ph}	0.74 A	0.80 A	0.78 A

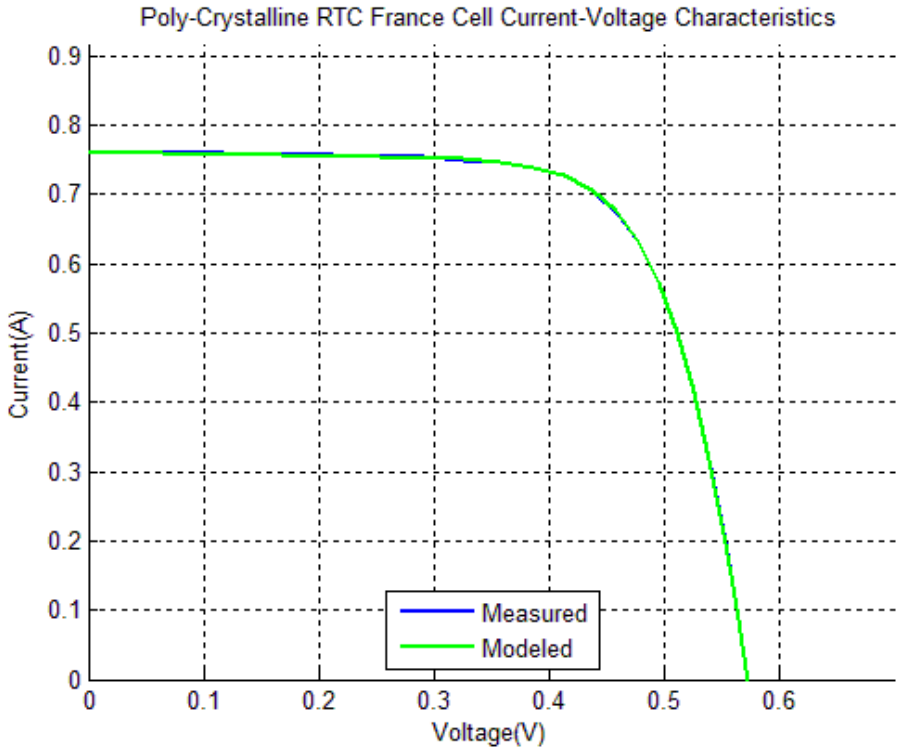

Figure 4.11: The measured and the modeled current-voltage characteristics corresponding to RTC France photovoltaic solar cell reproduced using the optimal model parameters. The online version of this figure is depicted in color.

Table 4.6: Estimated parameters of 57 mm poly-crystalline silicon RTC France photovoltaic solar cell measurement data based on different optimization approaches.

Parameters	**Least-Squares**	**Hamid *et al.*** [39]	**Askarzadeh *et al.*** [44]	**Huang *et al.*** [40]
Shunt Resistance, R_{sh}	44.992836 Ω	53.6894 Ω	52.2903 Ω	59.012 Ω
Series Resistance, R_s	0.038408 Ω	0.03638 Ω	0.03659 Ω	0.0354 Ω
Diode Ideality Factor, n	1.477108	1.48107	1.47583	1.5033
Diode Reverse Saturation Current, I_{sat}	2.09395×10^{-7} A	0.32267×10^{-6} A	0.30623×10^{-6} A	0.4000×10^{-6} A
Photo-generated Current, I_{ph}	0.761026 A	0.76078 A	0.76080 A	0.7607 A
Root Mean Square Error, RMSE	8.7×10^{-4}	9.86024×10^{-4}	9.9124×10^{-4}	0.00139
Parameters	**Easwarakhanthan *et al.*** [70]	**Bouzidi *et al.*** [41]	**AlRashidi *et al.*** [43]	**El Naggar *et al.*** [38]
Shunt Resistance, R_{sh}	53.7634 Ω	60.2410 Ω	64.1026 Ω	43.1034 Ω
Series Resistance, R_s	0.0364 Ω	0.0364 Ω	0.0313 Ω	0.0345 Ω
Diode Ideality Factor, n	1.4837	1.4816	1.6	1.5172
Diode Reverse Saturation Current, I_{sat}	3.223×10^{-7} A	3.267×10^{-7} A	9.980×10^{-7} A	4.798×10^{-7} A
Photo-generated Current, I_{ph}	0.7608 A	0.7607 A	0.7617 A	0.7620 A
Root Mean Square Error, RMSE	0.6251	0.3161	0.2863	0.0017

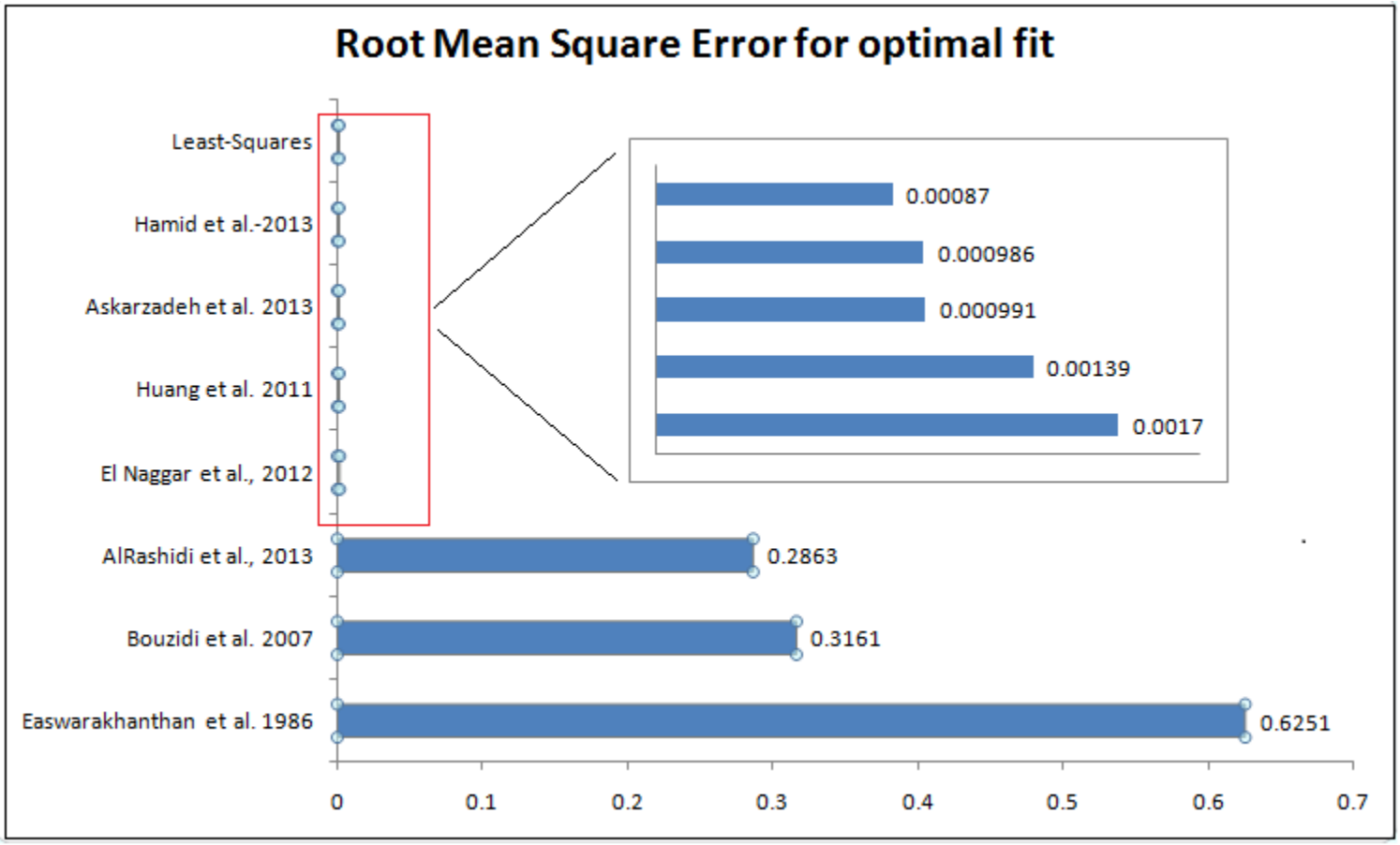

Figure 4.12: Comparison of the root mean squares error corresponding to the optimal least square fitting of current-voltage characteristic of RTC France cell based on different optimization algorithms. The online version of this figure is depicted in color.

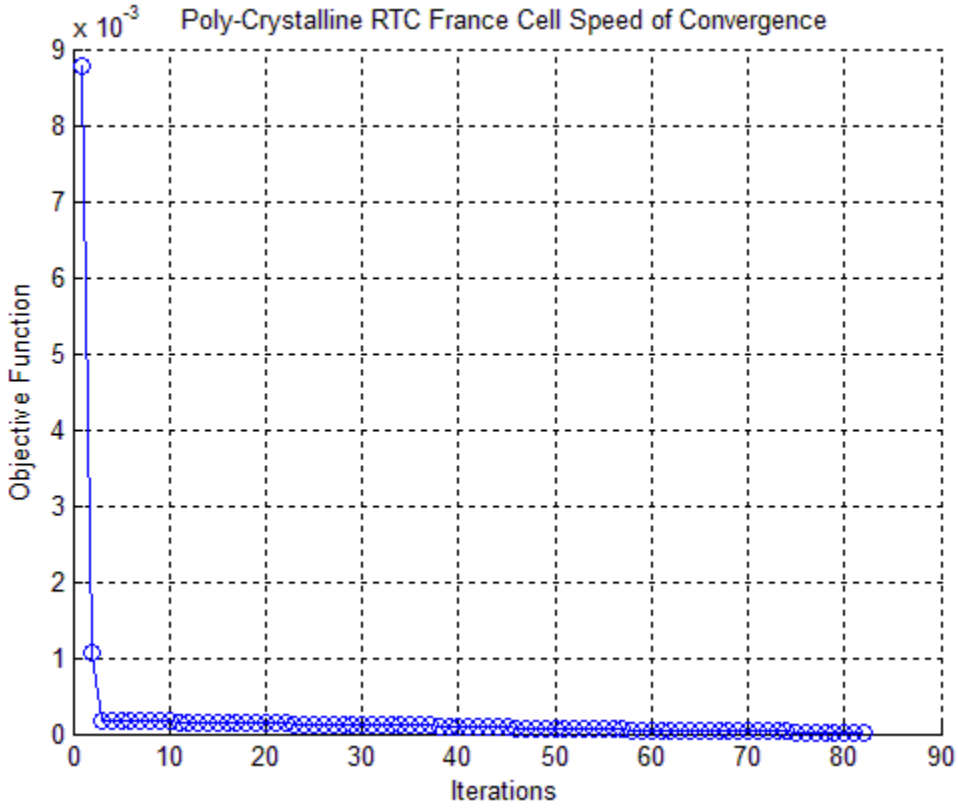

Figure 4.13: Speed of convergence based on the evaluation of the objective function given by the norm of the residual during successive iterations with respect to the least-squares fitting of the measured current-voltage data corresponding to RTC France photovoltaic solar cell, on a linear scale. The online version of this figure is in color.

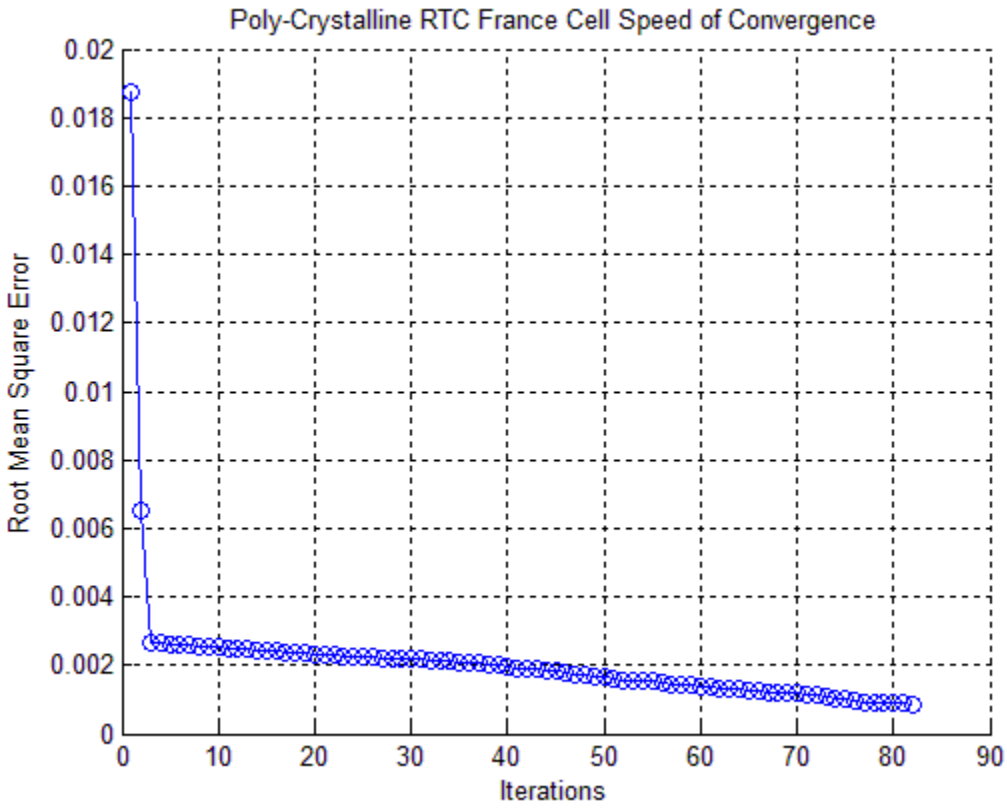

Figure 4.14: Speed of convergence based on the evaluation of the root mean square function during successive iterations with respect to the least-squares fitting of the measured current-voltage data corresponding to RTC France photovoltaic solar cell, on a linear scale. The online version of this figure is in color.

Following an analogous approach, the model parameter set, corresponding to the 36-cell poly-crystalline silicon solar module (Photowatt-PWP 201), was extracted and compared to verify the application of the algorithm with respect to current-voltage data corresponding to the modules considered in this analysis. Figure 4.15 shows the optimal least-squares fit, along with the intermediate fitting results for the optimization approach as it progresses through successive iterations. As is evident from the plot depicted in Figure 4.16, the least-squares fits appear to be very accurate, since the two plots are practically indistinguishable as they overlap with each other near perfectly. This finding concurs with the result obtained for the case of the RTC France solar cell current-voltage characteristic, as discussed previously.

The initial estimates, corresponding to the model parameters and the bounds to limit the search-space used to implement the algorithm, are tabulated in Table 4.7. Based on these parameters, the least-squares fit for the measured current-voltage data corresponding to the 36-cell poly-crystalline silicon solar module (Photowatt-PWP 201), the optimal parameters set are extracted, and are tabulated in Table 4.8. Similarly, the model parameters, extracted for this particular case, as reported by others based on different optimization approaches, are tabulated in Table 4.8. This shows that the least-squares optimization algorithm based on the trust-region method performs equally well for both cell and module data.

The speed of convergence for the optimization approach with respect to the least-squares fit for the measured current voltage data of 36 cell poly-crystalline silicon solar module (Photowatt-PWP 201)

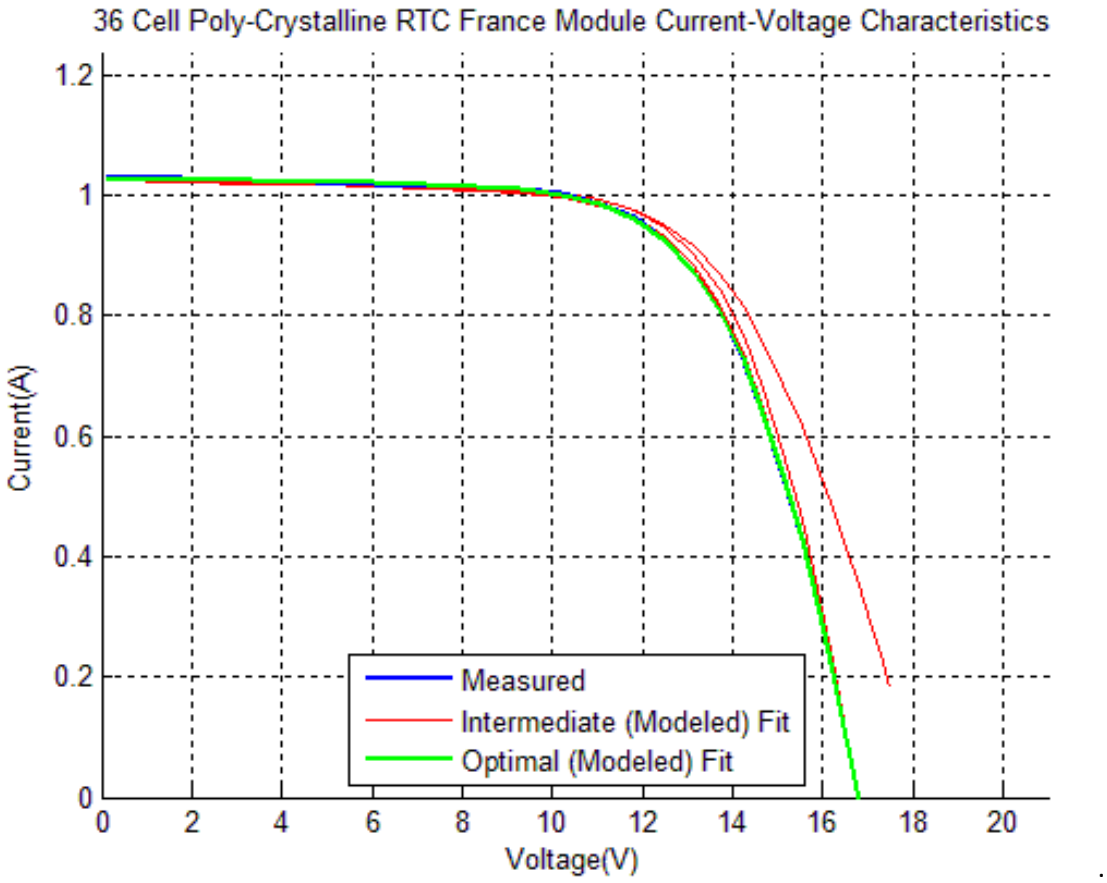

Figure 4.15: The intermediate current-voltage characteristics corresponding to 36 cell poly-crystalline silicon solar module (Photowatt-PWP 201) during successive iterations corresponding to the least-squares fitting process. The online version of this figure is depicted in color.

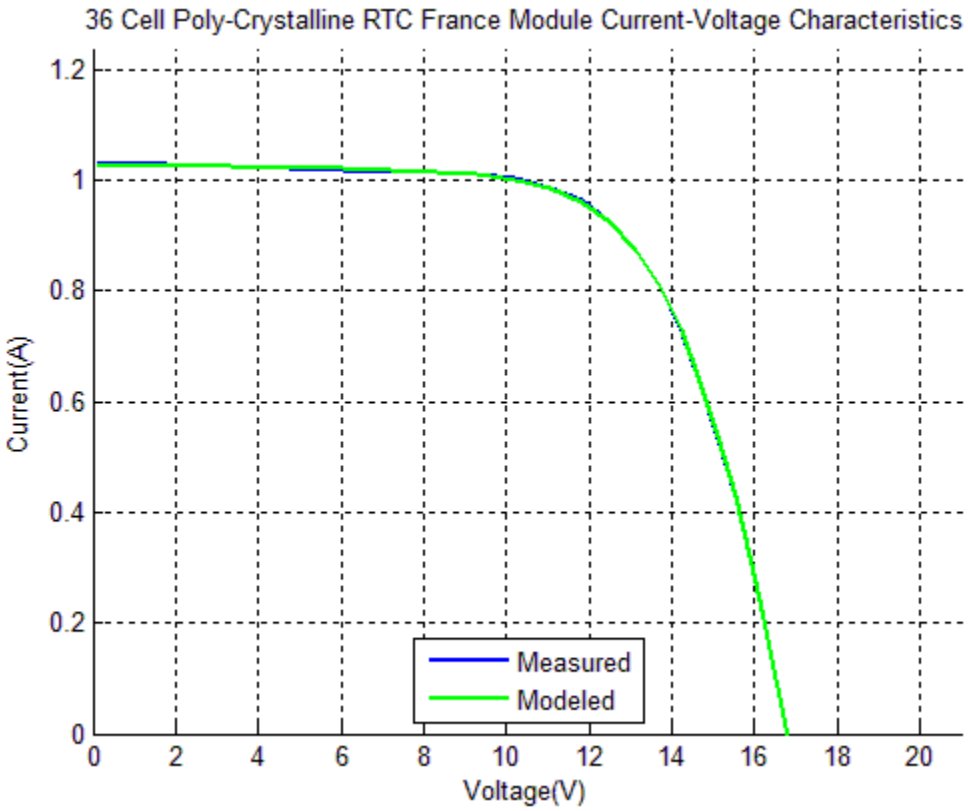

Figure 4.16: The measured and the modeled current-voltage characteristics corresponding to 36 cell poly-crystalline silicon solar module (Photowatt-PWP 201) reproduced using the optimal model parameters. The online version of this figure is depicted in color.

Table 4.7: List of initial estimates of parameters and bounds for the 36-cell poly-crystalline silicon solar module (Photowatt-PWP 201).

Module	**36 Cell Poly-Crystalline RTC France Module**		
Parameters	**Lower bound**	**Upper bound**	**Estimated Values**
Shunt Resistance, R_{sh}	100Ω	1000 Ω	700 Ω
Series Resistance, R_s	1.1Ω	2.8 Ω	2.5 Ω
Diode Ideality Factor, n	1.03	1.5	1.25
Diode Reverse Saturation Current, I_{sat}	1×10^{-10} A	9×10^{-6} A	1.5×10^{-6} A
Photo-generated Current, I_{ph}	1.02 A	1.04 A	1.03 A

Table 4.8: Estimated parameters 36 cell poly-crystalline silicon solar module (Photowatt-PWP 201) module measurement data based on different optimization approaches.

Parameters	**Least-Squares**	**Easwarakhanthan *et al.*** [70]	**Bouzidi *et al.*** [41]	**AlRashidi *et al.*** [43]	**El Naggar *et al.*** [38]
Shunt Resistance, R_{sh}	891.174657 Ω	714.2857 Ω	555.5556 Ω	555.5556 Ω	833.3333 Ω
Series Resistance, R_s	1.210525 Ω	1.2053 Ω	1.2030 Ω	1.2057 Ω	1.1989 Ω
Diode Ideality Factor, n	1.431209	1.3414	1.3385	1.3458	1.3561
Diode Reverse Saturation Current, I_{sat}	3.18036×10^{-6} A	3.1756×10^{-6} A	3.0760×10^{-6} A	3.2875×10^{-6} A	3.6642×10^{-6} A
Photo-generated Current, I_{ph}	1.031043 A	1.0313 A	1.0339	1.0318	1.0331
Root Mean Square Error, RMSE	0.002101	0.0118	0.6130	0.7805	0.0027

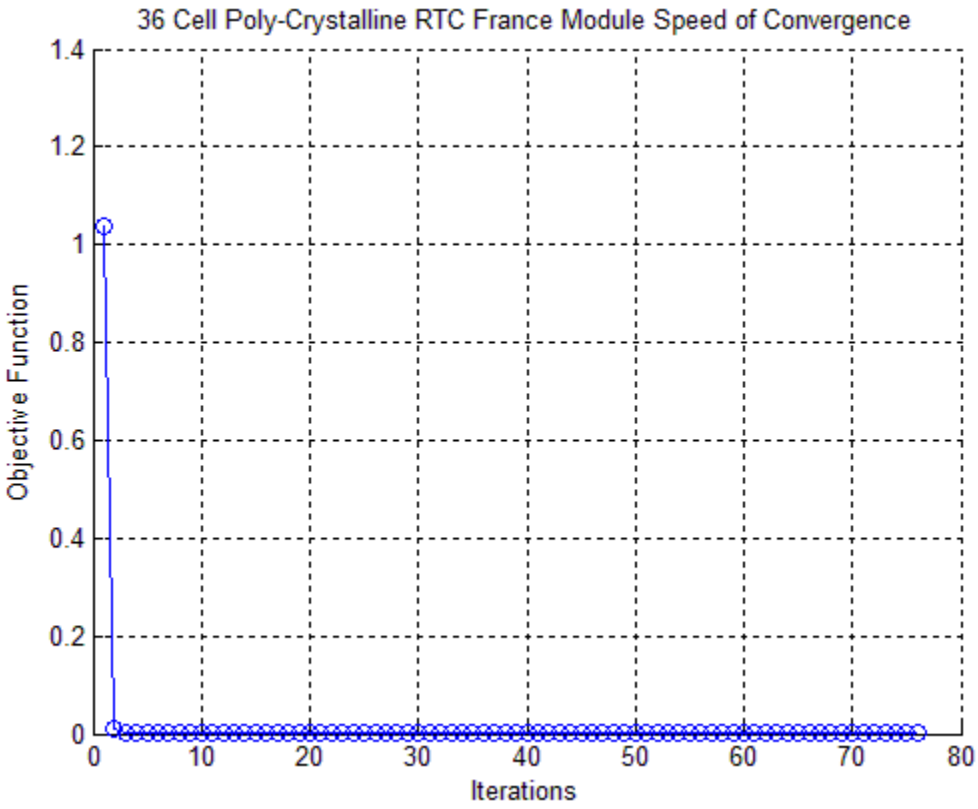

Figure 4.17: Speed of convergence based on the evaluation of the objective function given by the norm of the residual during successive iterations with respect to the least-squares fitting of the measured current-voltage data corresponding to a 36-cell poly-crystalline silicon solar module (Photowatt-PWP 201), depicted on linear scale. The online version of this figure is depicted in color.

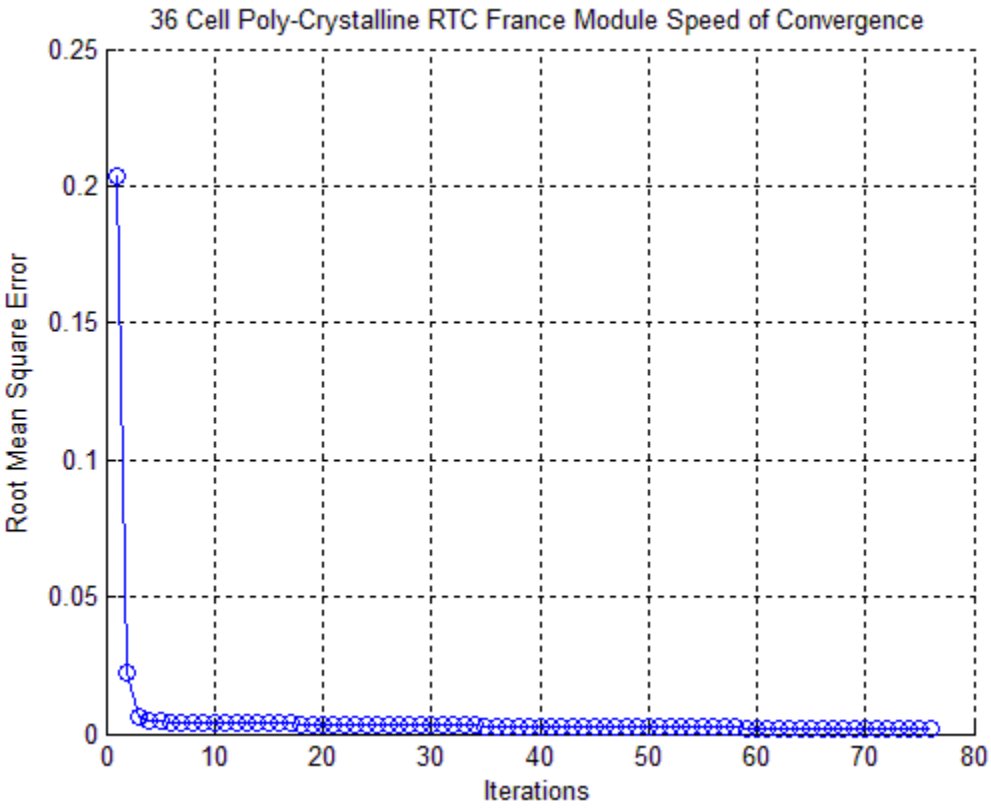

Figure 4.18: Speed of convergence based on the evaluation of the root mean square error function during successive iterations with respect to the least-squares fitting of the measured current-voltage data corresponding to a 36-cell poly-crystalline silicon solar module (Photowatt-PWP 201), depicted on a linear scale. The online version of this figure is depicted in color.

are traced based on minimization of the objective function and an additional metric of root-mean squares error as a function of the number of iterations. They are depicted in Figures 4.17 and 4.18, respectively.

4.8 Model Parameter Extraction Analysis

The least-squares optimization algorithm based on the trust-region method for parameter extraction is then employed to extract model parameters corresponding to the remaining twenty-nine sample photovoltaic modules (from Table 4.1) from their respective measured current-voltage characteristics, and similar results are acquired for each case. Depicting the results for model parameter estimation for all thirty samples of photovoltaic modules (from Table 4.1) through plots corresponding to the progression from intermediate result of fitting leading up to the optimal fit, and plots corresponding to the objective function, would require numerous plots. Since every ten samples of these thirty photovoltaic module samples are associated with the three classes of the product groups, which are similar in terms of the types of cells used and processes involved, it is reasonable to believe that parameters for these photovoltaic modules will behave more or less similarly for each class. Figures 4.19 through 4.23 depict the five parameters extracted corresponding to the thirty modules. Any significant outliers, especially below the relatively uniform cluster of the parameter values, corresponding to similar modules, can indicate the relative performance for the different modules.

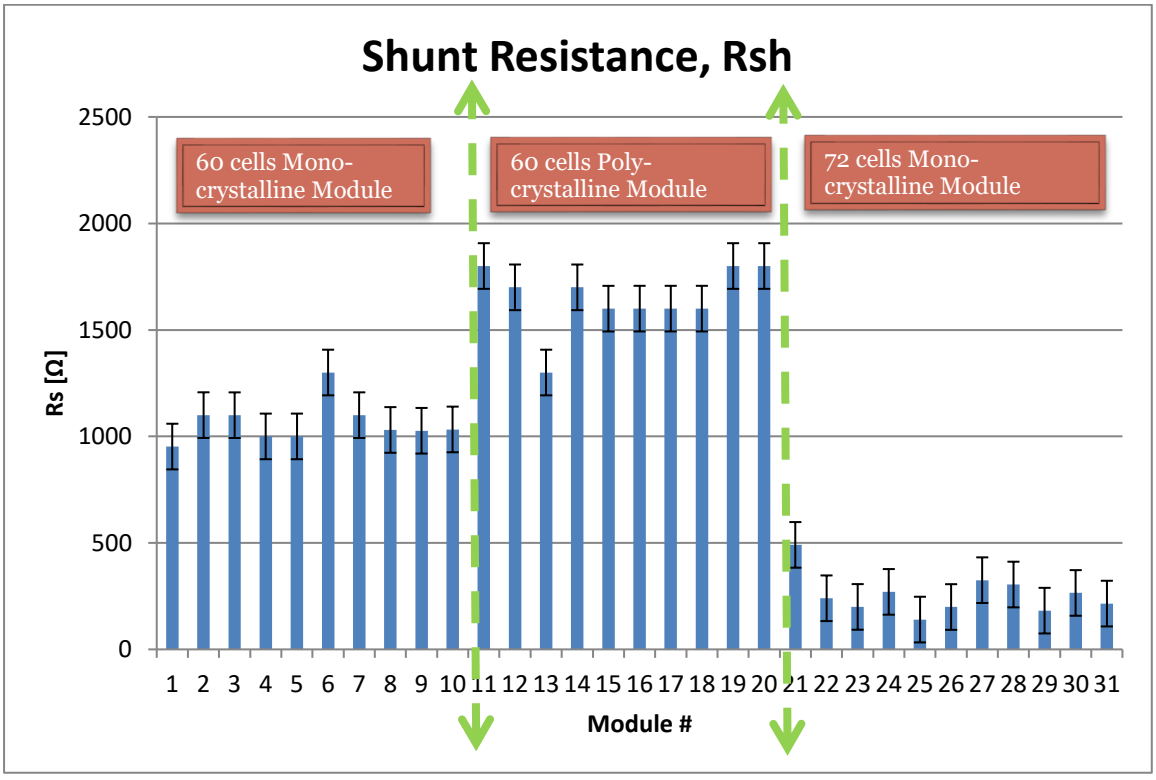

Figure 4.19: Extracted shunt resistance corresponding to the each of the all photovoltaic modules based on least-squares fitting of the measured current-voltage data. The online version of this figure is depicted in color.

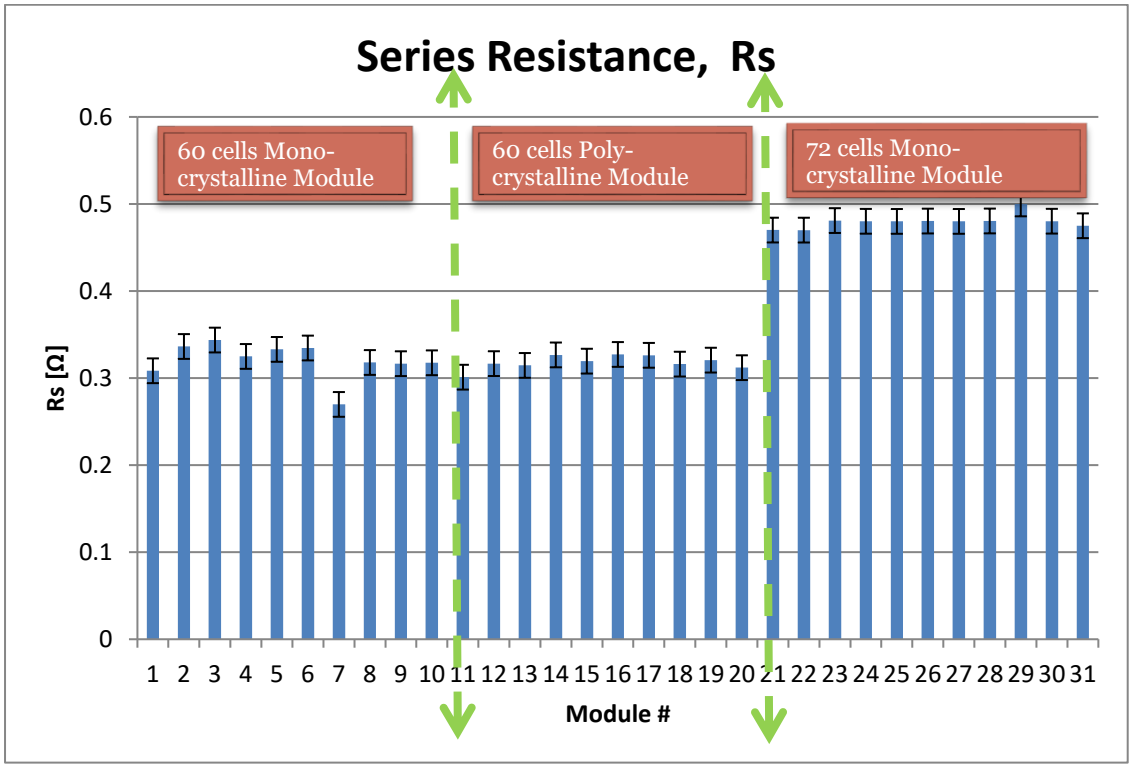

Figure 4.20: Extracted series resistance corresponding to the each of the test modules based on least-squares fitting of the measured current-voltage data. The online version of this figure is in color.

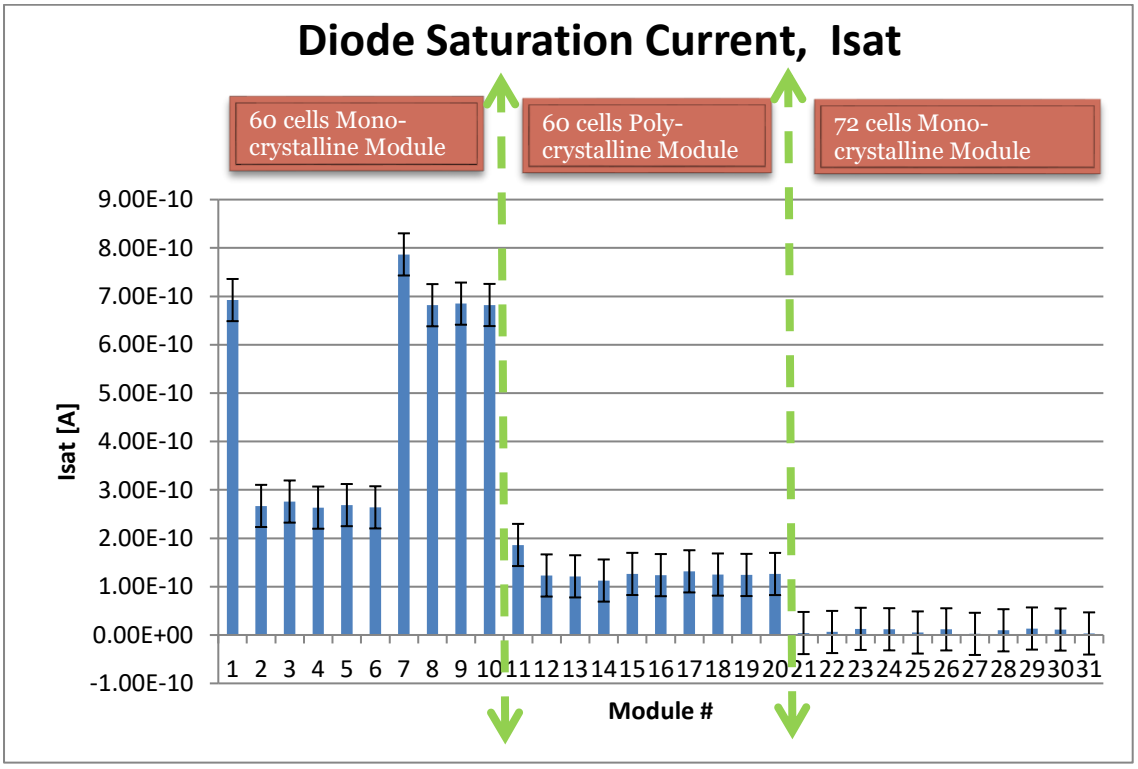

Figure 4.21: Extracted diode reverse saturation current corresponding to the each of the test modules based on least-squares fitting of the measured current-voltage data. The online version of this figure is in color.

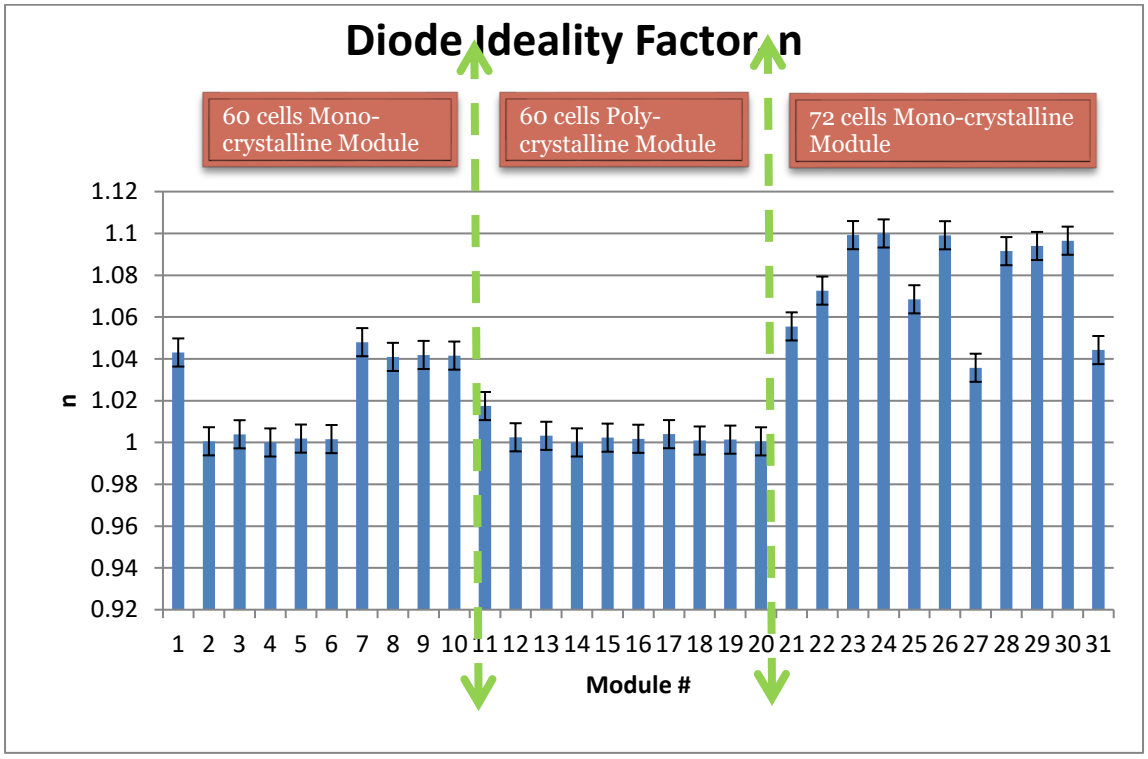

Figure 4.22: Extracted diode ideality factor corresponding to the each of the test modules based on least-squares fitting of the measured current-voltage data. The online version of this figure is in color.

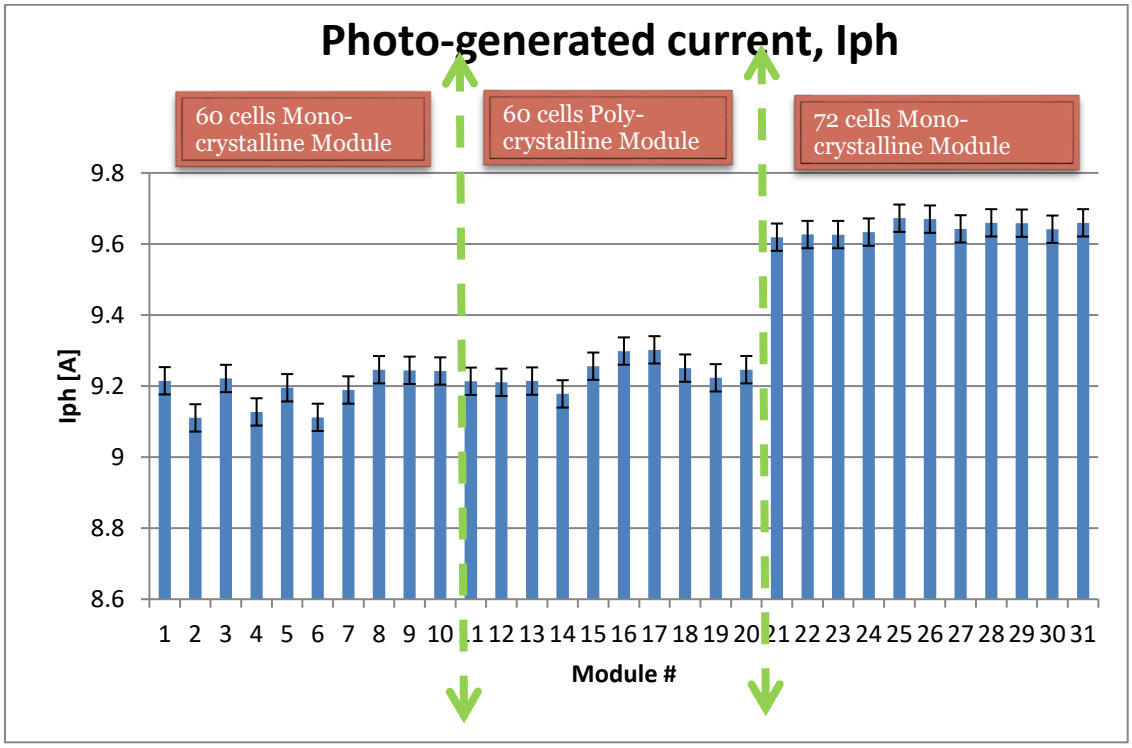

Figure 4.23: Extracted photo-generated current corresponding to the each of the test modules based on least-squares fitting of the measured current-voltage data. The online version of this figure is in color.

Chapter 5 Conclusions

In this thesis, an approach has been developed wherein the model parameters corresponding to a photovoltaic solar device, may be extracted from the measured electrical characteristics of the device. An empirical model, based on a single-diode equivalent electrical circuit, was adopted for the analysis of photovoltaic devices in their elementary form as individual solar cells and as commercial units fabricated using collection of solar cells to form of solar modules. This analysis was rooted in the current-voltage characteristics associated with such device, modeled based on a p-n junction behavior of the solar cells in conjunction with associated non-idealities of the device. The impact of individual model parameters on the overall electrical characteristics of the device were also demonstrated through a sensitivity analysis. Further to this, the collective impact of all model parameters on current-voltage characteristics may be further explored to get a better understanding of how the device performance is related to model parameters.

As part of the computational approach proposed, the problem of model parameter extraction from the measured current-voltage characteristics of photovoltaic device was formulated as a multivariate optimization problem based on a least-squares fitting approach using a trust region optimization strategy. Through a comparison with other approaches that have been used for parameter extraction corresponding to a set of benchmark data, it was demonstrated that the proposed approach based on the trust-region based optimization algorithm, produces results which are improved over those employed by others. The proposed extraction approach resulted in the most accurate fit of the

experimental current-voltage data to the model resulting in accurate extraction of the model parameters. This was demonstrated through fitting of benchmark current-voltage data associated with a silicon solar cell (57 mm RTC France solar cell) which resulted in the root means squares error of 8.7×10^{-4} A, a figure which is the lowest among the other extraction schemes. Similar results were obtained for the case of benchmark current-voltage data corresponding to a photovoltaic solar module. Finally, the parameter extraction approach was then applied to experimental current-voltage characteristics corresponding to thirty-one different samples of crystalline silicon based photovoltaic solar module produced by our anonymous industrial sponsor, and the resultant model parameters were determined based on this parameter extraction process. As expected, the extraction approach resulted in model parameter extraction with an average root mean square error of 0.0459 A among the thirty-one sample modules studied. Variations in these parameter values were observed according to the different categories of the product samples tested.

This parameter extraction is viewed as offering a first step to a new quality-control approach. If the range of model parameters corresponding to “good-quality” photovoltaic solar cells can be defined, then it may be possible to reject and classify solar modules based on parameter extraction in of itself. Unfortunately, given that no control on the deposition and materials were exercised and were performed by the industrial partner of this project, this was not possible for this project itself. This thesis represents a preliminary step towards a deeper research question. Control over the constituent material and composition would facilitate the task of defining the subset of the values (extent of the envisioned n-

dimensional hyperspace) for each model parameters that could be used for pass/fail criterion in quality assessment. In addition to material characterization, the use of extracted model parameters may be expanded to explore the power engineering aspects of the field especially with regards to power conditioning applications such as its use in maximum power tracking controllers, inverters, etc. Clearly, this work will have to be performed in the future.

References

[1] M. Asif and T. Ã. Muneer, “Energy supply , its demand and security issues for developed and emerging economies,” *Renew. Sustain. Energy Rev.*, vol. 11, no. 7, pp. 1388–1413, 2007.

[2] N. Nakicenovic and M. Jefferson, “Global Energy Perspectives to 2050 and Beyond,” *Energy Explor. Exploit.*, vol. 14, no. 2, pp. 149–151, 1996.

[3] I. Dincer, “Renewable energy and sustainable development : a crucial review,” *Renew. Sustain. Energy Rev.*, vol. 4, no. 2, pp. 157–175, 2000.

[4] O. Ellabban, H. Abu-Rub, and F. Blaabjerg, “Renewable energy resources: Current status, future prospects and their enabling technology,” *Renew. Sustain. Energy Rev.*, vol. 39, pp. 748–764, 2014.

[5] Energy Information Agency, “Classification of Renewable Energy,” 2015. [Online]. Available: http://www.eia.gov/energyexplained/?page=renewable_home#tab1. [Accessed: 17-Jan-2016].

[6] N. Kannan and D. Vakeesan, “Solar energy for future world: - A review,” *Renew. Sustain. Energy Rev.*, vol. 62, pp. 1092–1105, 2016.

[7] J. L. Gray, “The Physics of the Solar Cell,” in *Handbook of Photovoltaics Science and Engineering*, 2nd ed., John Wiley and Sons Ltd., 2011, pp. 82–129.

[8] P. Hersch and K. Zweibel, “Basic Photovoltaic Principles and Methods,” Solar Energy Research Institute, Golden, CO, 1982.

[9] D. M. Chapin, C. S. Fuller, and G. L. Pearson, “A New Silicon p-n Junction Photocell for Converting Solar Radiation into Electrical Power.,” *J. Appl. Phys.*, vol. 25, no. 5, pp. 676–677, 1954.

[10] L. Fraas and L. Partain, *Solar Cells and Their Applications*, 2nd ed. New Jersey: John Wiley and Sons Inc., 2010.

[11] J. Perlin, *From Space to Earth: The Story of Solar Electricity*. Michigan: Aatec Publications, 1999.

[12] A. J. Gonzalez, A. Sanchez-Jaurez, A. Fernandez, X. Mathew, and P. . Sebestain, “Converting Solar Radiation to Electric Power in Mexico,” in *Towards a Cleaner Planet: Energy for the Future*, Mexico: Springer, 2007, pp. 281–303.

[13] P. Cousins, D. Smith, H. Luan, J. Manning, T. Dennis, A. Waldhauer, K. Wilson, G. Harley, and W. Mulligan, “Generation 3: Improved performance at lower cost.,” in *Conference Record of the 35th IEEE Photovoltaic Specialists Conference*, 2010, pp. 275–278.

[14] D. D. Smith, P. J. Cousins, A. Masad, A. Waldhauer, S. Westerberg, M. Johnson, X. Tu, T. Dennis, G. Harley, G. Solomon, S. Rim, M. Shepherd, S. Harrington, M. Defensor, A. Leygo, P. Tomada, J. Wu, T. Pass, L. Ann, L. Smith, N. Bergstrom, C. Nicdao, P. Tipones, and D. Vicente, “Generation III high efficiency lower cost technology: Transition to full scale manufacturing,” in *Conference Record of the 38th IEEE Photovoltaic Specialists Conference*, 2012, pp. 1594–1597.

[15] P. Chiu, S. Wojtczuk, C. Harris, and D. Pulver, “42.3% Efficient InGaP/GaAs/InGaAs Concentrators using Bifacial Epigrowth.,” in *Conference Record of the 37th IEEE Photovoltaic Specialists*

Conference, 2011, pp. 000771–000774.

[16] J. L. Sawin, K. Seyboth, F. Sverrisson, F. Appavou, A. Brown, B. Epp, A. Leidreiter, C. Lins, H. E. Murdock, E. Musolino, K. Petrichenko, A. Tsakiris, J. Skeen, and B. Sovacool, "Renewables 2016 global status report," REN21 Secretariat, Paris, 2016.

[17] U. Pillai, "Drivers of cost reduction in solar photovoltaics," *Energy Econ.*, vol. 50, pp. 286–293, 2015.

[18] K. H. Solangi, M. R. Islam, R. Saidur, N. A. Rahim, and H. Fayaz, "A review on global solar energy policy," *Renew. Sustain. Energy Rev.*, vol. 15, no. 4, pp. 2149–2163, 2011.

[19] M. E. Kearney A T, Hauff J, Verdonck M, Derveaux H, Dumarest L, Malherbe J A, Charles J, Gammal A E, Llamas P, Masson G, "Unlocking the Sunbelt Potential of Photovoltaics," European Photovoltaic Industry Association and Others, 2010.

[20] Solargis, "Global Horizontal Irradiation (GHI)," 2016. [Online]. Available: http://solargis.com/products/maps-and-gis-data/free/download/world. [Accessed: 01-Jan-2016].

[21] C. D. Manning and J. A. Gow, "Development of a photovoltaic array model for use in power-electronics simulation studies," *IEE Proc. Electr. Power Appl.*, vol. 146, no. 2, pp. 193–200, 1999.

[22] R. Dufo-López, J. M. Lujano-Rojas, and J. L. Bernal-Agustín, "Comparison of different lead-acid battery lifetime prediction models for use in simulation of stand-alone photovoltaic systems," *Appl. Energy*, vol. 115, pp. 242–253, 2014.

[23] S. Kasap, *Principles of electronic materials and devices*, Third Edit. New York: McGraw-Hill, 2002.

[24] G. P. Willeke, "The Fraunhofer ISE Roadmap For Crystalline Silicon Solar Cell Technology," in *Conference Record of the 29th IEEE Photovoltaic Specialists Conference*, 2002, pp. 53–57.

[25] C. Hu, *Modern Semiconductor Devices for Integrated Circuits*. New Jersey: Pearson/Princeton Hall, 2010.

[26] K. L. Kennerud, "Analysis of Performance Degradation in CdS Solar Cells," *IEEE Trans. Aerosp. Electron. Syst.*, vol. AES-5, no. 6, pp. 912–917, 1969.

[27] D. Chang and J. Phang, "Analytical Methods for the Extraction of Solar-Cell Single- and Double-Diode Model Parameters from I-V Characteristics," *IEEE Trans. Electron Devices*, vol. ED-34, no. 2, pp. 286–293, 1987.

[28] M. A. De Blas, J. L. Torres, and E. Prieto, "Selecting a suitable model for characterizing photovoltaic devices," *Renew. Energy*, vol. 25, no. 3, pp. 371–380, 2002.

[29] K. Ishaque, Z. Salam, H. Taheri, and A. Shamsudin, "Parameter Extraction of Photovoltaic Cell Using Differential Evolution Method," in *Conference Record of the IEEE Applied Power Electronics Colloquium*, 2011, pp. 10–15.

[30] J. C. H. Phang, D. S. H. Chan, and J. R. Phillips, "Accurate analytical method for the extraction of solar cell model parameters," *Electron. Lett.*, vol. 20, no. 10, p. 406, 1984.

[31] J. P. Charles, M. Abdelkrim, Y. H. Muoy, and P. Mialhe, "A Practical Method of Analysis of the

Current-Voltage Characteristics of Solar Cell," *Sol. Cells Their Sci. Technol. Appl. Econ.*, vol. 4, no. 2, pp. 169–178, 1981.

[32] M. G. Villalva, J. R. Gazoli, and E. R. Filho, "Comprehensive Approach to Modeling and Simulation of Photovoltaic Arrays," *IEEE Trans. Power Electron.*, vol. 24, no. 5, pp. 1198–1208, 2009.

[33] S. Weixiang, C. F. Hoong, W. Peng, L. P. Chiang, and K. S. Yang, "Development of a mathematical model for solar module in photovoltaic systems," in *Proceedings of the 6th IEEE Conference on Industrial Electronics and Applications*, 2011, no. 4, pp. 2056–2061.

[34] R. Gottschalg, M. Rommel, D. G. Infield, and M. J. Kearney, "The influence of the measurement environment on the accuracy of the extraction of the physical parameters of solar cells," *Meas. Sci. Technol.*, vol. 10, no. 9, pp. 796–804, 1999.

[35] A. H. Alqahtani, "A simplified and accurate photovoltaic module parameters extraction approach using matlab," in *Proceedings of the IEEE International Symposium on Industrial Electronics*, 2012, pp. 1748–1753.

[36] A. A. El Tayyan, "An approach to extract the parameters of solar cells from their illuminated I - V curves using the Lambert W function," *Turkish J. Phys.*, vol. 39, no. 1, pp. 1–15, 2015.

[37] M. Azab, "Identification of one-diode model parameters of PV devices from nameplate information using particle swarm and least square methods," in *1st Workshop on Smart Grid and Renewable Energy*, 2015.

[38] K. M. El-Naggar, M. R. AlRashidi, M. F. AlHajri, and A. K. Al-Othman, "Simulated Annealing Algorithm for Photovoltaic Parameters Identification," *Sol. Energy*, vol. 86, no. 1, pp. 266–274, 2012.

[39] N. Farhana, A. Hamid, N. A. Rahim, and J. Selvaraj, "Solar Cell Parameters Extraction using Particle Swarm Optimization Algorithm.," in *IEEE Conference on Clean Energy and Technology*, 2013, pp. 461–465.

[40] H. Wei, J. Cong, X. Lingyun, and S. Deyun, "Extracting Solar Cell Model Parameters Based on Chaos Particle Swarm Alogorithm," in *International Conference on Electric Information and Control Engineering*, 2011, pp. 398–402.

[41] K. Bouzidi, M. Chegaar, and N. Nehaoua, "New method to extract the parameters of solar cells from their illuminated I-V curve," in *Proceedings of the 4th International Conference on Computer Integrated Manufacturing*, 2007.

[42] M. F. AlHajri, K. M. El-Naggar, M. R. AlRashidi, and A. K. Al-Othman, "Optimal extraction of solar cell parameters using pattern search," *Renew. Energy*, vol. 44, pp. 238–245, 2012.

[43] M. R. AlRashidi, M. F. AlHajri, K. M. El-Naggar, and A. K. Al-Othman, "A new estimation approach for determining the I-V characteristics of solar cells," *Sol. Energy*, vol. 85, no. 7, pp. 1543–1550, 2011.

[44] A. Askarzadeh and A. Rezazadeh, "Artificial bee swarm optimization algorithm for parameters identification of solar cell models," *Appl. Energy*, vol. 102, pp. 943–949, 2013.

[45] “PV Resources.” [Online]. Available: http://www.pvresources.com/en/standards/standards.php. [Accessed: 01-Jan-2017].

[46] “IEC - TC 82 Solar Photovoltaic Energy System.” [Online]. Available: http://www.iec.ch/dyn/www/f?p=103:7:0::::FSP_ORG_ID:1276. [Accessed: 01-Jan-2017].

[47] “IEC 60904-1 Ed.2:2006-09 Photovoltaic devices – Part 1: Measurement of photovoltaic current-voltage characteristics,” 2006.

[48] “IEC 61215 Ed.2: 2005-04 Crystalline silicon terrestrial photovoltaic (PV) modules – Design qualification and type approval Ed.1: 1993-04,” 2005.

[49] K. Emery, “Calibration and Rating of Photovoltaics,” in *presented at the IEEE Photovoltaic Specialists Conference*, 2012, pp. 1–6.

[50] A. Tolvanen, “Seminar on Solar Simulation Standards and Measurement Principles,” 2006. [Online]. Available: http://www.endeas.fi/wp-content/uploads/2016/01/Solar-Simulation-Standards-and-QuickSun-Measurement-System.pdf. [Accessed: 27-Aug-2016].

[51] W. Shockley, “The Theory of p-n Junctions in Semiconductors and p-n Junction Transistors,” *Bell Syst. Tech. J.*, vol. 28, pp. 435–489, 1949.

[52] M. B. Prince, “Silicon Solar Energy Converters,” *J. Appl. Phys.*, vol. 26, no. 5, p. 534, 1955.

[53] C. Honsberg and S. Bowden, “PV Education Network.” [Online]. Available: http://pveducation.org/pvcdrom/solar-cell-operation/series-resistance. [Accessed: 01-Jan-2016].

[54] S. Yadir, S. Assal, A. El Rhassouli, M. Sidki, M. Benhmida, and I. V. Þ. I. Od, “A new technique for extracting physical parameters of a solar cell model from the double exponential model (DECM),” *Opt. Mater. (Amst).*, vol. 36, no. 1, pp. 18–21, 2014.

[55] S. Shongwe and M. Hanif, “Gauss-Seidel Iteration Based Parameter Estimation for a Single Diode Model of a PV Module,” in *Proceedings of the IEEE Electrical Power and Energy Conference: Smarter Resilient Power Systems*, 2015, pp. 278–284.

[56] S. Shongwe and M. Hanif, “Comparative Analysis of Different Single-Diode PV Modeling Methods,” *IEEE J. Photovoltaics*, vol. 5, no. 3, pp. 938–946, 2015.

[57] L. H. I. Lim, Z. Ye, J. Ye, D. Yang, and H. Du, “A linear identification of diode models from single I-V characteristics of PV panels,” *IEEE Trans. Ind. Electron.*, vol. 62, no. 7, pp. 4181–4193, 2015.

[58] H. Tian, F. Mancilla-David, K. Ellis, E. Muljadi, and P. Jenkins, “A cell-to-module-to-array detailed model for photovoltaic panels,” *Sol. Energy*, vol. 86, no. 9, pp. 2695–2706, 2012.

[59] A. G. Aberle, S. . R. Wenham, and M. a. Green, “A new method for accurate measurements of the lumped series resistance of solar cells,” in *Conference Record of the IEEE Photovoltaic Specialists Conference*, 1993, pp. 133–139.

[60] M. C. Di Piazza, M. Luna, G. Petrone, and G. Spagnuolo, “About the Identification of the Single - Diode Model Parameters of High - Fill - Factor Photovoltaic Modules,” in *5th International Conference on Clean Electrical Power: Renewable Energy Resources Impact*, 2015, pp. 85–91.

[61] X. Weidong, W. G. Dunford, and A. Capel, “Novel Modeling Method for Photovoltaic Cells,” in *PESC Record - IEEE Annual Power Electronics Specialists Conference*, 2004, pp. 1950–1956.

[62] A. N. Celik and N. Acikgoz, “Modelling and experimental verification of the operating current of mono-crystalline photovoltaic modules using four- and five-parameter models,” *Appl. Energy*, vol. 84, no. 1, pp. 1–15, 2007.

[63] M. Belarbi and A. Boudghene-stambouli, “A new algorithm of parameter estimation of a photovoltaic solar panel,” *Turkish J. Electr. Eng. Comput. Sci.*, vol. 24, no. 1, pp. 276–284, 2016.

[64] N. Moldovan, R. Picos, and E. Garcia-moreno, “Parameter Extraction of a Solar Cell Compact Model usign Genetic Algorithms,” in *Proceedings of the 2009 Spanish Conference on Electron Devices*, 2009, pp. 379–382.

[65] Y. Yuan, “A Review of Trust Region Algorithms for Optimization,” *Int. Congr. Ind. Appl. Math.*, vol. 99, pp. 271–282, 2000.

[66] K. Levenberg, “A method for the solution of certain non-linear problem in least squares,” *Q. Appl. Math.*, vol. 2, no. 278, pp. 164–168, 1944.

[67] D. W. Marquardt, “An algorithm for least-squares estimation of nonlinear parameters.,” *J. Soc. Ind. Appl. Math.*, vol. 11, no. 2, pp. 431–441, 1963.

[68] M. J. . Powell, “A New Algorithm for Unconstrained Optimization,” in *Nonlinear Programming*, J. B. Rosen, O. L. Mangasarian, and K. Ritter, Eds. Academic Press Inc., 1970, pp. 31–66.

[69] J. J. More and D. C. Sorensen, “Computing a trust region step.,” *Soc. Ind. Appl. Math.*, vol. 4, no. 3, pp. 553–572, 1983.

[70] T. Easwarakhantan, J. Bottin, I. Bouhouch, and C. Boutrit, “Nonlinear Minimization Algorithm for Determining the Solar Cell Parameters with Microcomputers.,” *Int. J. Sol. Energy*, vol. 4, no. 1, pp. 1–12, 1986.

[71] A. Demirbas, “Potential applications of renewable energy sources, biomass combustion problems in boiler power systems and combustion related environmental issues,” *Prog. Energy Combust. Sci.*, vol. 31, no. 2, pp. 171–192, 2005.